UNIVERSITY OF CALIFORNIA,
IRVINE

Optical Methods for Ranging and Analog-to-Digital Conversion

DISSERTATION

submitted in partial satisfaction of the requirements
for the degree of

DOCTOR OF PHILOSOPHY

in Electrical and Computer Engineering

by

Rasul Torun

Dissertation Committee:
Professor Ozdal Boyraz, Chair
Professor Payam Heydari
Professor Mohammad Al Faruque

2019

DEDICATION

I would like to dedicate this dissertation to my family for their invaluable support and unconditional love throughout my life.

TABLE OF CONTENTS

LIST OF FIGURES

LIST OF TABLES

Page

ACKNOWLEDGMENTS

I would like to express my sincere gratitude to my advisor, Prof. Ozdal Boyraz, for his guidance, support and time. Also, I would like to thank my committee members, Prof. Payam Heydari and Prof. Mohammad Al Faruque for their time and suggestions.

Additionally, I would like to thank my senior labmate Dr. Salih Kalyoncu who helped me to improve my experimental skills and familiarize the field of optics. His advice and supervision was priceless to pursue research in this field. Also, I would like to thank my colleague, Mustafa Mert Bayer, due to his valuable contributions in our collaborated research.

I would like to take this opportunity to also thank all my colleagues who have persistently cooperated with me and guided me in my research. In particular, I would like to extend my warmest appreciation to Dr. Salih Kalyoncu, Dr. Yuewang Huang, Dr. Qiancheng Zhao, Imam Uz Zaman, Parinaz Sadri, Mustafa Mert Bayer, Mohammad Wahiduzzaman Khan, Md Shafiqul Islam, Alan Kai Tam, Shah Rahman and Tuva Atasever for their encouragement and support.

I gratefully acknowledge the research fellowship received from the Scientific and Technological Research Council of Turkey (TUBITAK) during my graduate studies.

To sum up, special thanks to my family for supporting and encouraging me all the time.

* * * * * * * * *

Large portions of this work are based on research authored by Rasul Torun, performed under the advisement of Prof. Ozdal Boyraz. Please check "Publications" in Curriculum Vitae. In particular, Chapter 3 is heavily borrowed from the following publications.

[J1] **R. Torun**, M. M. Bayer, I. U. Zaman, J. E. Velazco, and O. Boyraz, Realization of Multitone Continuous Wave Lidar, IEEE Photonics J., vol. 11, no. 4, pp. 110, 2019.

[C1] **R. Torun**, M. M. Bayer, I. U. Zaman, and O. Boyraz, Multi-tone modulated continuous-wave lidar, in Photonic Instrumentation Engineering VI, 2019, vol. 10925, p. 109250V.

[C2] M. M. Bayer, **R. Torun**, I. U. Zaman, and O. Boyraz, A Basic Approach for Speed Profiling of Alternating Targets with Photonic Doppler Velocimetry, in CLEO: Applications and Technology, 2019, pp. AW4K4.

CURRICULUM VITAE

Rasul Torun

EDUCATION

Doctor of Philosophy in Electrical Engineering **2019**
University of California, Irvine *Irvine, CA*

Master of Science in Electrical Engineering **2018**
University of California, Irvine *Irvine, CA*

Master of Science in Electronics and Computer Engineering **2015**
Istanbul Sehir University *Istanbul, Turkey*

Bachelor of Science in Electronics Engineering **2011**
Sabanci University *Istanbul, Turkey*

RESEARCH EXPERIENCE

Graduate Research Assistant **2012–2019**
University of California, Irvine *Irvine, California*

Scalable Fast Dispersive Laser Scanner
Investigation of Modulation Instability in RF over Fiber Links
Inter-satellite Optical Communicator Design
Multi-tone Modulated Continuous Wave Lidar
Photonic Assisted Analog-to-digital Converter Design

TEACHING EXPERIENCE

Teaching Assistant **2013–2019**
University of California, Irvine *Irvine, California*

EECS 70A - Network Analysis I
EECS 70B & 70LB - Network Analysis II & Laboratory
EECS 170A & 170LA - Electronics I & Laboratory
EECS 170B & 170LB - Electronics II & Laboratory
EECS 182 - MMIC Analysis and Design
EECS 188 - Optical Electronics
EECS 285A - Optical Communications

Teaching Assistant **2011–2012**
Istanbul Sehir University *Istanbul, Turkey*

PHYS 103 & 103L - Mechanics and Dynamics & Lab
PHYS 104 & 104L - Electromagnetics and Modern Physics & Lab

JOURNALS IN PREPARATION

[1] **R. Torun**, M. M. Bayer, and O. Boyraz, Performance Evaluation of Photonic Assisted Analog to Digital Converter Employing Pulse Modulation, (in preparation).

[2] **R. Torun**, M. M. Bayer, and O. Boyraz, Full System Performance Demonstration of Multi-tone Continuous Wave Lidar, (in preparation).

REFEREED JOURNAL PUBLICATIONS

[J1] **R. Torun**, M. M. Bayer, I. U. Zaman, J. E. Velazco, and O. Boyraz, Realization of Multitone Continuous Wave Lidar, IEEE Photonics J., vol. 11, no. 4, pp. 110, 2019.

[J2] S. K. Kalyoncu, **R. Torun**, Y. Huang, Q. Zhao, and O. Boyraz, Fast Dispersive Laser Scanner by Using Digital Micro Mirror Arrays, J. Micro Nano-Manuf., vol. 2, no. 2, p. 021004, 2014.

[J3] S. Rahman, **R. Torun**, Q. Zhao, and O. Boyraz, Electronic control of optical tweezers using space-time-wavelength mapping, J. Opt. Soc. Am. B, vol. 33, no. 3, p. 313, Mar. 2016.

[J4] Q. Zhao, P. Sadri-Moshkenani, M. W. Khan, **R. Torun**, and O. Boyraz, On-chip bimetallic plasmo-thermomechanical detectors for mid-infrared radiation, IEEE Photonics Technol. Lett., vol. 29, no. 17, pp. 14591462, 2017.

[J5] Y. Huang, Q. Zhao, S. K. Kalyoncu, **R. Torun**, and O. Boyraz, Silicon-on-sapphire mid-IR wavefront engineering by using subwavelength grating metasurfaces, JOSA B, vol. 33, no. 2, pp. 189194, 2016.

[J6] Y. Huang, Q. Zhao, S. K. Kalyoncu, **R. Torun**, Y. Lu, F. Capolino and O. Boyraz, Phase-gradient gap-plasmon metasurface based blazed grating for real time dispersive imaging, Appl. Phys. Lett., vol. 104, no. 16, p. 161106, Apr. 2014.

[J7] Y. Huang, S. K. Kalyoncu, Q. Zhao, **R. Torun**, and O. Boyraz, Silicon-on-sapphire waveguides design for mid-IR evanescent field absorption gas sensors, Opt. Commun., vol. 313, pp. 186194, 2014.

REFEREED CONFERENCE PUBLICATIONS

[C1] **R. Torun**, M. M. Bayer, I. U. Zaman, and O. Boyraz, Multi-tone modulated continuous-wave lidar, in Photonic Instrumentation Engineering VI, 2019, vol. 10925, p. 109250V.

[C2] M. M. Bayer, **R. Torun**, I. U. Zaman, and O. Boyraz, A Basic Approach for Speed Profiling of Alternating Targets with Photonic Doppler Velocimetry, in CLEO: Applications and Technology, 2019, pp. AW4K4.

[C3] D. Borlaug, **R. Torun**, O. Boyraz, and B. Jalali, V-pi reduction by using modulation index booster (MiBo) in RF links, in 2015 IEEE Optical Interconnects Conference (OI), 2015, pp. 148149.

[C4] S. Rahman, **R. Torun**, Q. Zhao, T. Atasever, and O. Boyraz, Electronically-controlled optical tweezing using space-time-wavelength mapping, in SPIE Optical Engineering+ Applications, 2015, p. 95810E95810E.

[C5] O. Boyraz, M. M. Bayer, **R. Torun**, and I.-U. Zaman, TuD2. 2-Multi Tone Continuous Wave Lidar, in 2019 IEEE Photonics Society Summer Topical Meeting Series (SUM), 2019, pp. 12.

[C6] I. U. Zaman, A. Janzen, **R. Torun**, M. Y. Peng, J. Velazco, and O. Boyraz, Omnidirectional optical transceiver design techniques for multi-frequency full duplex CubeSat data communication, in CubeSats and NanoSats for Remote Sensing II, 2018, vol. 10769, p. 1076915.

[C7] I. U. Zaman, A. W. Janzen, **R. Torun**, M. Peng, J. E. Velazco, and O. Boyraz, Design Tradeoffs and Challenges of Omnidirectional Optical Antenna for High Speed, Long Range Inter CubeSat Data Communication, in Small Satellite Conference, Delivering Mission Success, SSC18-WKII-06, 2018.

[C8] S. K. Kalyoncu, Y. Huang, **R. Torun**, Q. Zhao, and O. Boyraz, Fast Dispersive Laser Scanner by Using Digital Micro Mirror Arrays, CLEO 2013, p. JTu4A.30.

[C9] S. Rahman, P. Sadri-Moshkenani, **R. Torun**, and O. Boyraz, Space-Time-Wavelength Mapping Based Electronically Controlled Two Dimensional Optical Tweezing, in CLEO: Science and Innovations, 2016, p. SM2I3.

[C10] Q. Zhao, Y. Huang, **R. Torun**, S. Rahman, T. C. Atasever, and O. Boyraz, Numerical investigation of silicon nitride trench waveguide, in SPIE Optical Engineering+ Applications, 2015, p. 95860O95860O.

[C11] Q. Zhao, P. Sadri-Moshkenani, M. W. Khan, **R. Torun**, I.-U. Zaman, and O. Boyraz, Infrared detection using plasmonically enhanced thermomechanically actuated nanowire arrays, in CLEO: QELS$_F$*undamentalScience*, 2017, *pp.JTh*2*A*114.

[C12] Q. Zhao, M. W. Khan, P. Sadri-Moshkenani, **R. Torun**, I.-U. Zaman, and O. Boyraz, Plasmo-thermomechanical suspended nanowire array detectors for mid-infrared spectrum, in Infrared Sensors, Devices, and Applications VII, 2017, vol. 10404, p. 104040L.

[C13] Y. Huang, Q. Zhao, S. K. Kalyoncu, **R. Torun**, Y. Lu, F. Capolino and O. Boyraz, Plasmonic sub-wavelength phase-gradient meta-surfaces for real time dispersive imaging, in Lasers and Electro-Optics (CLEO), 2014 Conference on, 2014, pp. 12.

[C14] Y. Huang, Q. Zhao, S. K. Kalyoncu, **R. Torun**, Y. Lu, and O. Boyraz, Silicon on

sapphire mid-IR wave-front engineering by using sub-wavelength gratings, in Lasers and Electro-Optics (CLEO), 2014 Conference on, 2014, pp. 12.

[C15] Y. Huang et al., Wavelength conversion bandwidth enhancement through quasi-phase-matching in a width modulated silicon waveguide, in Optical Fiber Communication Conference, 2013, p. JTh2A33.

ABSTRACT OF THE DISSERTATION

Optical Methods for Ranging and Analog-to-Digital Conversion

By

Rasul Torun

Doctor of Philosophy in Electrical and Computer Engineering

University of California, Irvine, 2019

Professor Ozdal Boyraz, Chair

Optical methods are employed in various fields from communications to space research to improve the system performance. Each application uses different properties of light and light-matter interaction. For example, ultra-high frequency nature of light is desirable in applications like ranging and velocimetry to increase the resolution. On the other hand, in the telecommunication industry, ultra-wide bandwidth of the fibers is utilized with time and wavelength multiplexing techniques that make Gigabit internet possible today. Such multiplexing techniques are also useful in photonic assisted analog to digital converters (ADC) that multiply the sampling rates of electronic ADCs. Additionally, ultra-low (<10fs) jitter performance of lasers make an accurate sampling of fast events possible.

To be specific, this thesis covers multi-wavelength approaches to Lidar and photonic assisted ADCs. In ranging, multiple optical tones are generated through modulation with multiple RF frequencies and relative phase shift between individual tones are utilized to detect the range and velocity of a target. On the other hand, in photonic assisted ADC system, multiple continuous-wave lasers at different wavelengths are being utilized to achieve wavelength multiplexing, accurate delays, and to correct gain and offset mismatches between interleaved ADC channels.

In the first part of the dissertation, the multi-tone modulated continuous wave (MTCW) lidar

system is analytically and numerically investigated. Also, a proof-of-concept experiment by employing 1550nm light source and multiple RF tone modulations ranging from 50MHz to 6GHz has been performed to demonstrate proof of principle for range finding with <1cm range resolution. Additionally, the velocity measurement capability of the system has been demonstrated by using a target attached to a speaker membrane or a stepper motor.

The second part of the dissertation presents a photonic assisted ADC system that employs wavelength-multiplexed pulse-modulated lasers as an optical sampler to capture an RF signal. The sampled signal is demultiplexed and quantized with electronic ADCs after optoelectronic conversion. The system is analytically and numerically investigated for its performance limitations and requirements to overcome the problems.

Chapter 1

Introduction

Multi-wavelength optical methods are employed in research areas ranging from biomedical applications to Earth science research to analyze tissue, blood cells, material property, atmosphere by utilizing different absorbance, reflectance, or fluorescence capabilities of the materials. On the other hand, multi-wavelength light sources are utilized to increase bandwidth in communications and accuracy in sensing applications. Depending on the application one or selected number of properties of multiwavelength or broadband laser sources such as differential absorption, dispersion, nonlinearity, coherence, etc can be used to enable creative engineering solutions. This thesis demonstrates how multi-wavelength and multi-tone laser sources can be used for light detection and ranging, and photonic assisted analog to digital conversion applications.

Light detection and ranging (Lidar) has been used in various ways such as military applications [1] and atmospheric sciences [2] to detect remote objects, measure distances [3], create topographical images [4], detect aerosol particles [5], and measure ozone layers [6, 7]. In recent years, with the advent of self-driving cars and unmanned aerial vehicles (UAV), Lidar became a topic of interest once again for proximity sensing and collision prevention

[8]. Current continuous-wave lidar methodologies are either sweeping phase as in amplitude modulated continuous wave (AMCW) lidars [9] or frequency as in frequency modulated continuous wave (FMCW) lidars [10]. In this thesis, we demonstrate a new multi-tone modulated system to achieve single-shot measurements by eliminating the need for sweeping any parameter.

On the other hand, low timing jitter of lasers along with time and wavelength interleaving capability of the broadband optical sources make them desirable for time-interleaved photonic assisted Analog to Digital Converter (ADC) systems. Conventionally, mode-locked lasers are employed in photonic assisted ADCs [11] for their ultra-low jitter property. The jitter of a mode-locked laser can even be as low as attosecond level that is unheard of for electronic sampling circuits [12]. However, mode-locked lasers are not so desirable due to their high cost. Thanks to the highly commercialized telecommunication industry, components operating at C-band region are cheaper than their counterparts used in other areas such as biomedical applications. In this thesis, we propose a pulse-modulated CW laser-based system and investigate its performance in time-interleaved photonic assisted ADCs. The multiple wavelengths are employed to interleave several channels of the proposed optical front end for electronic ADCs.

The dissertation is organized as follows. Chapter 1 presents a brief introduction to optical methods used in this thesis and the objective of this research. Chapter 2 explains the background of light-matter interactions in fibers and fiber amplifiers including dispersion, nonlinear effects such as Kerr nonlinearity and Raman. Also, the theoretical formulations of each phenomenon and numerical methods used to simulate light-matter interactions are explained. In Chapter 3, a multi-tone modulated continuous wave lidar system is presented. MTCW lidar system is composed of a CW laser modulated with multiple RF tones and an interferometric coherent detection system to detect the range and velocity of the target by investigating phase delay and frequency shift of the measurement signal with respect to a

reference local oscillator. In Chapter 4, a photonic assisted ADC system is presented. The system is a front end for electronic ADCs to increase the effective sampling rate via time and wavelength interleaving in the optical domain. The method employs short-pulse modulation of CW lasers to employ as a sampler in optically sampled wavelength demultiplexed system. In Chapter 5, the performance limitations of the proposed ADC system are discussed. The dissertation ends with a general conclusion of all the works.

Chapter 2

Background

In this chapter, fundamentals of the background theory used in the applications covered in this thesis such as multi-tone continuous-wave lidars and photonic assisted analog-to-digital converters are presented.

Both applications consist of fiber-based subsystems including continuous wave (CW) lasers, Mach Zehnder modulator (MZM), Erbium-doped fiber amplifier (EDFA), polarization controllers (PC) and fibers. In the MTCW lidar system, fibers are just to connect the other components. However, in photonic assisted ADC, fiber is used to create time delay between different wavelengths. Therefore, first, pulse propagation in fibers is explained here. Later, discrete (EDFA) and distributed (Raman) optical amplification methods are presented.

2.1 Pulse Propagation in Fibers

2.1.1 Nonlinear Schrödinger Equation

Both linear dispersive and nonlinear effects influence the propagating optical pulses inside a fiber. The linearity in optics is defined by intensity independence [13]; therefore fiber becomes nonlinear especially for intense short pulses ranging from ∼10ns to 10fs. Both nonlinear and the dispersive effects change the pulse shape and spectra. As it is well known, light is also an electromagnetic wave; therefore its propagation inside the fiber is governed by Maxwell's equations [14].

$$\nabla \times E = -\frac{\partial B}{\partial t} \tag{2.1a}$$

$$\nabla \times H = J + \frac{\partial D}{\partial t} \tag{2.1b}$$

$$\nabla \cdot D = \rho_f \tag{2.1c}$$

$$\nabla \cdot B = 0 \tag{2.1d}$$

where D (C/m^2) and B (Wb/m^2) are the electric and the magnetic flux densities that are related to corresponding electric and magnetic field vectors E (V/m) and H (A/m) through equations:

$$D = \varepsilon_0 E + P \tag{2.2a}$$

$$B = \mu_0 H + M \tag{2.2b}$$

where ε_0 (F/m) is the electric permittivity and μ_0 (H/m) is the vacuum permeability which are related to speed of light via the equation c=$\frac{1}{\sqrt{\varepsilon_0 \mu_0}}$ (m/s). P (C/m^2) and M (Wb/m^2) are the induced electric and magnetic polarization vectors, respectively. When we consider the optical fiber, the equations are further simplified because of the non-magnetic medium

($M = 0$), and the absence of free charges (ρ_f=0) and free current ($J = 0$). The wave equation that describes the propagation of light inside the fiber can be obtained by substituting Eq. (2.2) into Maxwell's equations and taking the curl of Eq. (2.1a), that leads to:

$$\nabla^2 E(r,t) - \frac{1}{c^2}\frac{\partial^2 E(r,t)}{\partial t^2} = \mu_0 \frac{\partial^2 [P_L(r,t) + P_{NL}(r,t)]}{\partial t^2} \tag{2.3}$$

where P_L and P_{NL} are the linear and the nonlinear components of the induced electric polarization defined as:

$$P_L(r,t) = \varepsilon_0 \int_{-\infty}^{\infty} \chi^{(1)}(t - t^{'}) E(r,t^{'}) dt^{'} \tag{2.4}$$

$$P_{NL}(r,t) = \varepsilon_0 \left[\int_{-\infty}^{\infty} \int_{-\infty}^{\infty} \chi^{(2)}(t - t^{'}) E^2(r,t^{'}) dt^{'} dt^{'} \right] + \varepsilon_0 \left[\int_{-\infty}^{\infty} \int_{-\infty}^{\infty} \int_{-\infty}^{\infty} \chi^{(3)}(t - t^{'}) E^3(r,t^{'}) dt^{'} dt^{'} dt^{'} + \ldots \right] \tag{2.5}$$

where $\chi^{(n)}$ is the n^{th} order susceptibility of the dielectric medium. In Eq.(2.5), 2^{nd} order term vanishes due to inversion symmetry of silica fibers and the third order susceptibility $\chi^{(3)}$ becomes dominant that creates main nonlinear effects such as SPM and Raman scattering [14]. Thus, P_L and P_{NL} are approximated as:

$$P_L = \varepsilon_0 \chi^{(1)} E(r,t) \tag{2.6a}$$

$$P_{NL} \approx \varepsilon_0 \varepsilon_{NL} E(r,t) \tag{2.6b}$$

where

$$\varepsilon_{NL} = \frac{3}{4}\chi^{(3)} |E(r,t)|^2 \tag{2.6c}$$

The following assumptions are made in order to solve the wave equation in Eq.(2.3) [14]:

i The induced nonlinear polarization (P_{NL}) is so weak (causes less than 10^{-6} refractive index change), hence treated as a small perturbation.

ii The polarization is preserved along the fiber.

iii Slowly varying envelope approximation is used, because the field is quasi-monochromatic ($\Delta\omega/\omega_0 \ll 1$), where $\Delta\omega$ (Hz) is the bandwidth of the field and ω_0 (Hz) is the central frequency.

The propagation equation Eq.(2.3) fits better in the Fourier domain after simplifications and transforms to:

$$\nabla^2 E(r,\omega) + \varepsilon(\omega) k_0^2 E(r,\omega) = 0 \tag{2.7}$$

where the complex permittivity $\varepsilon(\omega) = \varepsilon_0(1 + \tilde{\chi}^{(1)}(\omega) + \tilde{\chi}^{(3)}(\omega) + \tilde{\chi}^{(5)}(\omega) + \ldots)$, $\tilde{\chi}^{(n)}$ is the Fourier transform of $\chi^{(n)}$ and the wavenumber $k_0 = \omega_0/c$ (rad/m). The refractive index (n) and the absorption coefficient (α) can be derived from the dielectric constant via

$$\varepsilon = \left(n + i\frac{\alpha}{2k_0}\right)^2 = (n_L + \Delta n)^2 \tag{2.8}$$

Therefore, they consist of both linear and nonlinear terms described by

$$n = n_L + n_{NL} = n_L + n_2|E|^2 \tag{2.9a}$$

$$\alpha = \alpha_L + \alpha_{NL} = \alpha_L + \alpha_2|E|^2 \tag{2.9b}$$

where the nonlinear index coefficient $n_2 = \frac{3}{8n}\Re\left[\chi^{(3)}\right]$ and two-photon absorption coefficient $\alpha_2 = \frac{3\omega_0}{4nc}\Im\left[\chi^{(3)}\right]$. The dielectric constant is mainly calculated by the refractive index and the absorption loss is added as a small perturbation as mentioned in the equation Eq. (2.8) where $\Delta n = n_2|E|^2 + i\frac{\alpha}{2k_0}$.

The separation of variables method can be used to solve Helmholtz Equation in Fourier domain and the solution will be in the form of:

$$E(r,\omega) = F(x,y)A(z,\omega)exp(i\beta_0 z) \tag{2.10}$$

where $F(x,y)$ is the field distribution of the fiber mode, $A(z,\omega)$ is the slowly varying envelope and the β_0 is the wave number. The mode distribution and the envelope equations can be derived from Eq.(2.7), when $E(r,\omega)$ terms replaced by the Eq.(2.10).

$$\frac{\partial^2 F(x,y)}{\partial x^2} + \frac{\partial^2 F(x,y)}{\partial y^2} + (\beta_0^2 - \bar{\beta}^2)F = 0 \tag{2.11}$$

$$2i\beta_0 \frac{\partial A}{\partial z} + (\bar{\beta}^2 - \beta_0^2)A = 0 \tag{2.12}$$

The first equation is solved by treating Δn as a first order perturbation, hence $\varepsilon = (n_L + \Delta n)^2 \approx n_L^2$. Therefore, $F(x,y)$ is independent of the nonlinear perturbation (Δn). The wave number is also defined as the sum of the linear and nonlinear terms respectively as in $\bar{\beta}(\omega) = \beta(\omega) + \Delta\beta(\omega)$.

$$\Delta\beta(\omega) = \frac{\omega^2 n(\omega)}{c\bar{\beta}(\omega)} \frac{\int_{-\infty}^{\infty}\int_{-\infty}^{\infty} \Delta n(\omega)|F(x,y)|^2 dxdy}{\int_{-\infty}^{\infty}\int_{-\infty}^{\infty} |F(x,y)|^2 dxdy} = i\frac{\alpha}{2} + \gamma|A|^2 \tag{2.13}$$

where $\gamma = \frac{n_2\omega_0}{cA_{eff}}$ is the nonlinear parameter and $A_{eff} = \frac{\left[\int_{-\infty}^{\infty}\int_{-\infty}^{\infty} |F(x,y)|^2 dxdy\right]^2}{\int_{-\infty}^{\infty}\int_{-\infty}^{\infty} |F(x,y)|^4 dxdy}$ is the effective mode area. The linear and nonlinear wave number terms are expanded by using Taylor

expansion around the carrier frequency ω_0, as shown below.

$$\beta(\omega) = \beta_0 + \sum_{j=1}^{\infty} \frac{1}{j!}\beta_j(\omega - \omega_0)^j \tag{2.14a}$$

$$\Delta\beta(\omega) \approx \Delta\beta_0 \tag{2.14b}$$

$$\bar{\beta}(\omega) \approx \beta_0 + \sum_{j=1}^{\infty} \frac{1}{j!}\beta_j(\omega - \omega_0)^j + \Delta\beta_0 \tag{2.14c}$$

where β_j is the jth order linear dispersive term and $\Delta\beta_0$ is the zeroth order nonlinear term.

By using the approximation $(\bar{\beta}^2 - \beta_0^2) \approx 2\beta_0\left[\bar{\beta}(\omega) - \beta_0\right]$ and substituting $\bar{\beta}(\omega)$ with Eq.(2.14c), Eq.(2.12) simplifies to [15]

$$\frac{\partial A}{\partial z} - i\sum_{j=1}^{\infty} \frac{1}{j!}\beta_j(\omega - \omega_0)^j A = i\Delta\beta_0 A \tag{2.15}$$

Further by substituting $\Delta\beta_0$ with $i\frac{\alpha}{2} + \gamma|A|^2$ and taking the inverse Fourier transform of both sides of Eq. (2.15), the well known Nonlinear Schrödinger Equation (NLSE) for A(z,t) is derived as:

$$\frac{\partial A}{\partial z} + \sum_{j=1}^{\infty} \frac{-i^{j+1}}{j!}\beta_j \frac{\partial^j A}{\partial t^j} = -\frac{\alpha}{2}A + i\gamma(\omega_0)|A|^2 A \tag{2.16}$$

The NLSE simplifies to

$$\frac{\partial A}{\partial z} + \beta_1\frac{\partial A}{\partial t} + i\frac{1}{2}\beta_2\frac{\partial^2 A}{\partial t^2} - \frac{1}{6}\beta_3\frac{\partial^3 A}{\partial t^3} + \frac{\alpha}{2}A = i\gamma|A|^2 A \tag{2.17}$$

after neglecting the higher order dispersion ($\beta_j = 0, j > 3$).

The simplified NLS equation (Eq. (2.17)) includes the effects of group velocity, group velocity dispersion, GVD slope, fiber loss, and fiber non-linearity respectively. The β_1 (s/m) is the reciprocal of group velocity and the β_2 (ps^2/km) is the GVD parameter of the propagation

medium. GVD slope (β_3) is negligibly small, unless second-order dispersion is $\sim$0 [14].

2.1.2 Group Velocity Dispersion

Group velocity is defined as the effective velocity of a wave packet that includes several frequency components. In an optical dispersive medium, the lights with different colors (frequencies) travel at different velocity. Since speed is associated with the refractive index, dispersion means having different refractive indices for different colors. In bulk materials dispersion is a material property. In fibers, the net dispersion has two parts: material and waveguide dispersion that are originated from the nature of the material used to propagate light and the optical waveguide design such as its geometry and materials used in core and cladding parts. In an optical fiber, phase velocity can be defined as $\nu_g = c/n(\omega)$ in terms of frequency. Generally, there are two types of dispersion such as normal and anomalous. In normal dispersion, the lower frequencies (red shifted) travel faster than higher frequencies (blue shifted) and it is vice versa for anomalous dispersion. The optical wave starts to broaden because of the speed difference between different frequency components. The effect of GVD on the pulse propagation in a linear medium can be studied by eliminating all the nonlinear terms in Schrdinger equation, which results to a simplified NLSE:

$$i\frac{\partial A}{\partial z} = -\frac{\beta_2}{2}\frac{\partial^2 A}{\partial t^2} \tag{2.18}$$

This simplified differential equation can easily be solved by Fourier transform method. The normalized, arbitrary shaped pulse in time domain $A(z,t)$ and its spectrum $\hat{A}(z,\omega)$ in frequency domain are related by Fourier transform as:

$$A(z,t) = \frac{1}{2\pi}\int_{-\infty}^{\infty} \hat{A}(z,\omega)\exp(-i\omega t)d\omega \tag{2.19}$$

By taking the Fourier transform of both sides in Eq. (2.18) with using time derivative property $\left(\frac{\partial^n}{\partial t^n} \rightarrow (i\omega)^n\right)$, it transforms into an ordinary differential equation:

$$i\frac{\partial \hat{A}}{\partial z} = -\frac{1}{2}\beta_2\omega^2\hat{A} \tag{2.20}$$

which has a solution in the form of:

$$\hat{A}(z,\omega) = \hat{A}(0,\omega)\exp\left(\frac{i}{2}\beta_2\omega^2 z\right) \tag{2.21}$$

It is obvious from the solution that GVD alters only the phase, not the amplitude of the initial pulse spectrum. The added phase is proportional to the frequency and propagation length. The phase change in spectrum modifies the pulse shape in time domain as shown in Fig. 2.1. The corresponding time domain solution is evaluated by taking the inverse Fourier Transform of Eq. (2.21).

$$A(z,t) = \frac{1}{2\pi}\int_{-\infty}^{\infty}\hat{A}(0,\omega)\exp\left(\frac{i}{2}\beta_2\omega^2 z\right)\exp(i\omega t)d\omega \tag{2.22}$$

The femtosecond laser pulses used in optics do not have a well-defined shape due to nonlinear processes inside the laser cavity, distortions, and noise interference etc. However, they can be approximated as Gaussian pulses, which are well defined mathematically, in order to investigate the effect of optical system on the pulse. The following part is the review on the effect of GVD on the Gaussian pulses. A normalized Gaussian pulse defines the initial pulse:

$$A(0,t) = \exp\left[\frac{1+iC}{2}\left(\frac{t}{T_0}\right)^2\right] \tag{2.23}$$

where C is the initial chirp parameter and T_0 is the half width at $1/e$ intensity point and related to full width at half maximum as $T_{FWHM} = 1.665T_0$. The final pulse after propagation

becomes:

$$A(z,t) = \frac{T_0}{\sqrt{T_0^2 - i\beta_2 z(1+iC)}} \exp\left[-\frac{(1+iC)t^2}{2(T_0^2 - i\beta_2 z(1+iC))}\right] \tag{2.24}$$

The result shows that both initially chirped ($C \neq 0$) and unchirped ($C = 0$) Gaussian pulses conserve their Gaussian shapes after propagation. However, the pulse width T_1 (defined similar to T_0) and the chirp parameter C_1 of the pulse change due to GVD as [16]:

$$\frac{T_1}{T_0} = \left[1 + \left(\frac{C\beta_2 z}{T_0^2}\right)^2 + \left(\frac{\beta_2 z}{T_0^2}\right)^2\right]^{1/2} \tag{2.25}$$

$$C_1(z) = C + (1+C^2)\frac{\beta_2 z}{T_0^2} \tag{2.26}$$

According to the results, it is easily seen that, if there is no initial chirp on the pulse, the pulse starts to broaden due to GVD independent of the medium type such as normal ($\beta_2 > 0$) or anomalous ($\beta_2 < 0$). If there is an initial chirp, pulse broadens faster than unchirped case when $\beta_2 C > 0$. On the other hand, if $\beta_2 C < 0$, the pulse first compress to compensate the effect of initial chirp and then starts to broaden again [16].

Simulation Results

The following simulation results show the GVD effect on the Gaussian pulse in time and frequency domain. The results are obtained by using SSFM with zero nonlinearity.

Figure 2.1 and 2.2 show the evolution of transform-limited and chirped Gaussian pulses along the fiber under the effect of GVD respectively. In the figures, the propagating pulses are displayed only at specific distances that are multiples of dispersion length, $L_D = \frac{T_0^2}{|\beta_2|}$, to

indicate the broadening and compression effects. Additionally, such pulses are normalized according to the peak intensity of the initial pulse. It is clearly seen in Fig. 2.1 that the GVD does not affect the spectrum intensity. However, time-domain pulses are broadened due to phase change in the frequency domain. On the other hand, Fig. 2.2 demonstrates the propagation of initially chirped pulses where compression and faster-broadening properties are observed. In addition to these, it is seen that Gaussian pulses remain Gaussian after propagation in linear dispersive mediums.

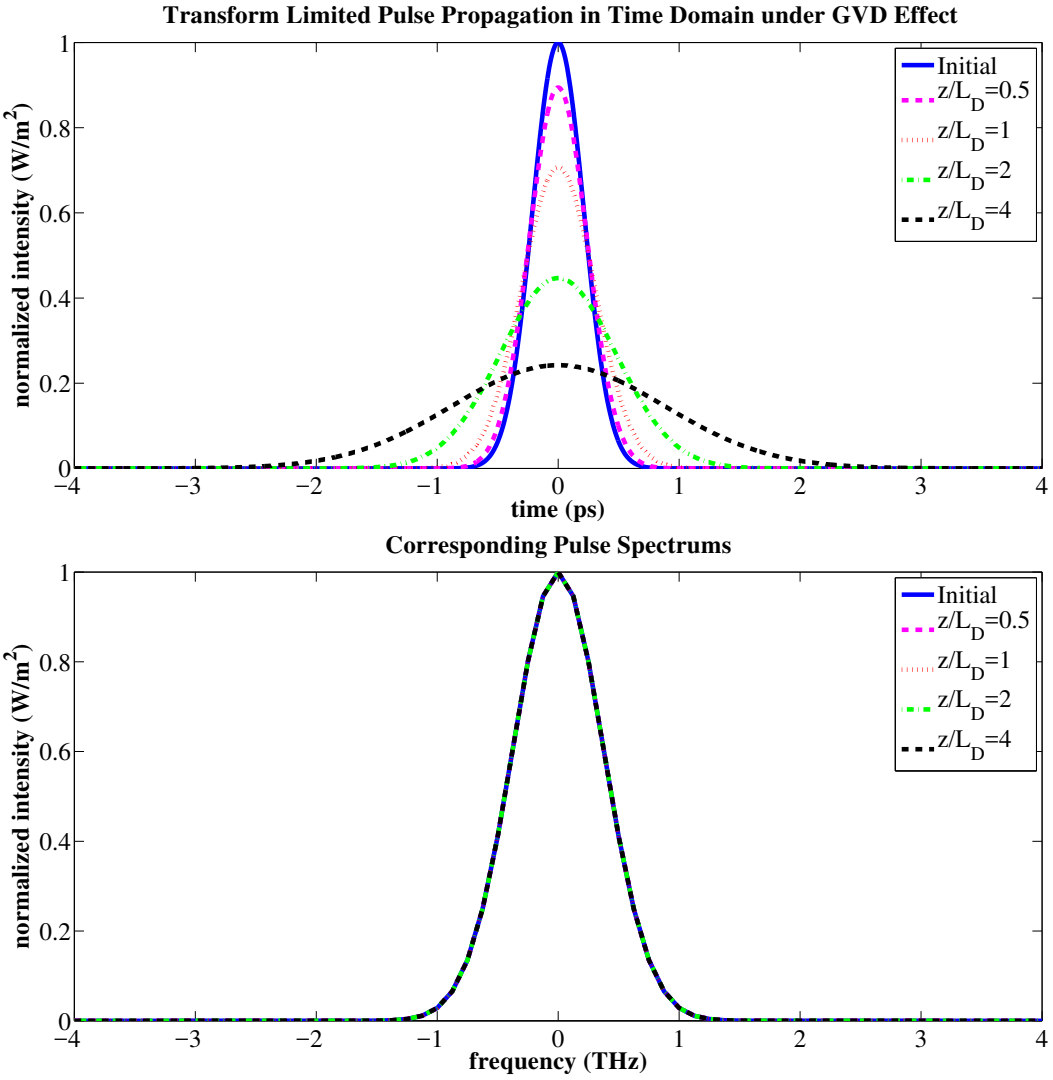

Figure 2.1: Transform limited Gaussian pulse ($T_{FWHM} = 500fs$) propagation inside a fiber. Temporal (upper) and Spectral (down) evolution due to GVD (D=17 ps/km-nm).

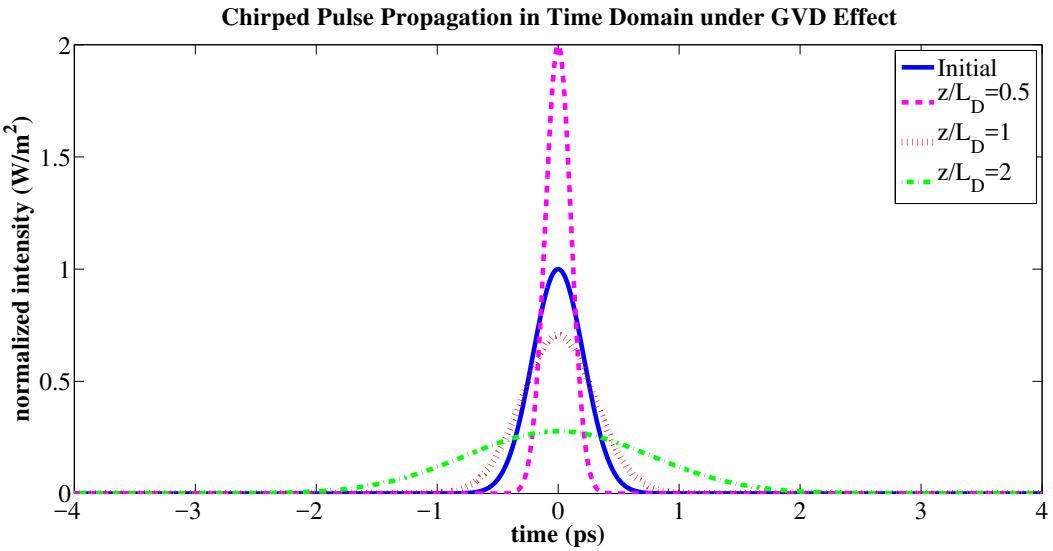

Figure 2.2: Chirped Gaussian pulse ($C = 2$) propagation inside a fiber under the effect of GVD (β_2=-21.67 ps^2/km). $L_D = \frac{T_0^2}{|\beta_2|}$ is the dispersion length.

2.1.3 Nonlinear Optical Effects

The optical medium becomes nonlinear when the electromagnetic field (light) intensity increases due to the small core area of the fiber and high peak power of the ultrashort pulses. Self and Cross Phase Modulation (SPM/XPM) are two fundamental nonlinear effects.

Self Phase Modulation

Refractive index of the dielectric medium also depends on the intensity of the light, in addition to the frequency as in GVD. The refractive index profile becomes nonlinear, when the light intensity inside the medium increases. As a result, the pulse experiences both linear GVD and nonlinear effects while propagating in fiber. The comparison between the

dispersion and nonlinear length determines the dominant effect.

$$L_D = \frac{T_0^2}{|\beta_2|} \tag{2.27a}$$

$$L_{NL} = \frac{1}{\gamma P_0} \tag{2.27b}$$

where L_D, L_{NL} are dispersion and nonlinear lengths respectively, γ is the nonlinearity parameter and P_0 is the peak power of the pulse [14]. Three possible cases are shown below.

i) If $L > L_D$ and $L > L_{NL}$, both GVD and SPM is effective.

ii) If $L_D \gg L > L_{NL}$, then GVD is negligible.

iii) If $L_{NL} \gg L > L_D$, then SPM is negligible.

Therefore, the individual effect of SPM can be studied by eliminating GVD in NLS Equation (case 2). The equation simplifies to

$$\frac{\partial A}{\partial z} = ie^{-\alpha z}\gamma P_0 |A|^2 A \tag{2.28}$$

As it is seen in Eq. (2.28), SPM creates an intensity dependent nonlinear phase on the pulse without changing the pulse shape in time domain. However, the added phases would distort the spectrum drastically. The solution to the above ordinary differential equation is

$$A(z = L, t) = A(0, t) \exp[i\phi_{NL}(z = L, t)] \tag{2.29}$$

where $\phi_{NL}(L, t) = |A(0, t)|^2 \gamma P_0 L_{eff}$ is the nonlinear phase and $L_{eff} = \frac{1-\exp(-\alpha L)}{\alpha}$ is the effective length. The maximum phase shift occurs at the peak intensity point (center for the Gaussian pulses) and given by $\phi_{max} = \gamma P_0 L_{eff}$.

Any time dependent phase on the signal creates new frequency components in the spectrum as it is stated in Fourier Theorem. In other words, phase change across the pulse creates an instantaneous frequency deviation from the center value ω_0 that causes a spectral broadening. The amount of SPM induced spectral shift, also called frequency chirp ($\delta\omega$) is obtained by taking the derivative of nonlinear phase.

$$\delta\omega(t) = -\frac{\partial\phi_{NL}}{\partial t} = -\gamma P_0 L_{eff}\frac{\partial}{\partial t}|A(0,t)|^2 \tag{2.30}$$

For Gaussian pulses as in Eq. (2.23), the SPM induced frequency shift is:

$$\delta\omega(t) = -\frac{2}{T_0^2}\frac{L_{eff}}{L_{NL}}t\exp\left(-\frac{t^2}{T_0^2}\right) \tag{2.31}$$

with a maximum shift of $\delta\omega_{max} = 0.86\Delta\omega_0\phi_{max}$ where $\Delta\omega_0 = T_0^{-1}$.

Simulation Results

The effect of Self Phase Modulation both in time and frequency domains is shown in the following simulation results. The input pulse is again taken as the normalized Gaussian pulse. We can see that the spectrum is drastically distorted, while the pulse shape is conserved through the propagation, as mentioned before. The results are obtained by using SSFM with changing parameters to satisfy case 2 ($L_D \gg L > L_{NL}$).

The SPM makes a spectral change while preserving the time domain signals as opposed to GVD. As it is shown in Fig. 2.3, the SPM is nonlinear and it transforms the spectrum arbitrarily.

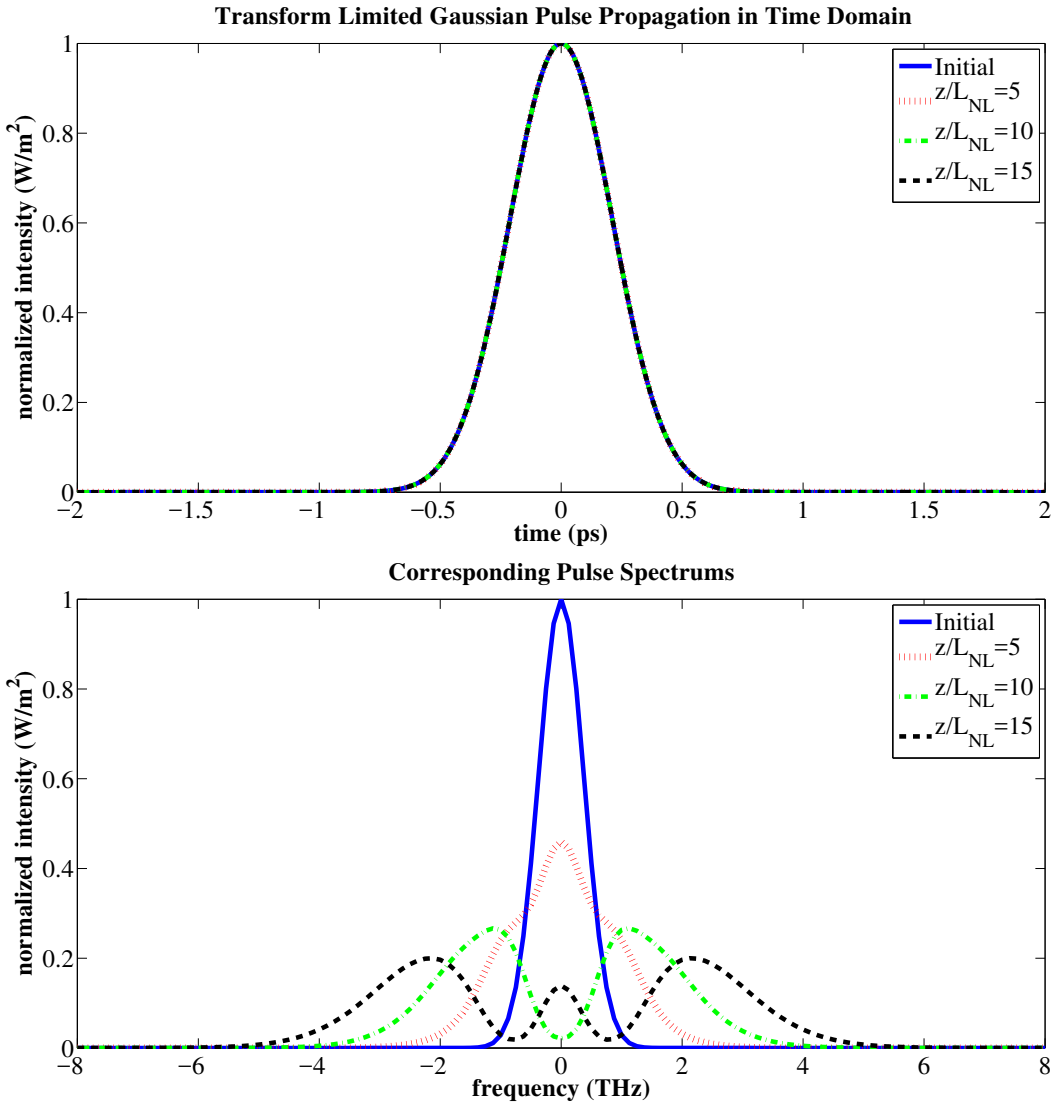

Figure 2.3: Transform limited Gaussian pulse propagation inside the fiber. Temporal (upper) and spectral (down) evolution due to nonlinear effect ($\gamma = 2W^{-1}km^{-1}$).

Cross Phase Modulation

Cross Phase Modulation is another nonlinear phenomenon similar to SPM, occurs when there is more than one optical beam in the medium at the same time. When the beams interact with each other, each optical beam experiences a refractive index change affected by its own intensity and the intensity of other beams that causes spectral broadening of the pulses [14]. The nonlinear phase caused by XPM is twice as high as SPM for the same intensity. As a result, the total nonlinear phase seen by each pulse due to SPM and XPM when N optical pulses with different frequencies propagate in a medium becomes [16]:

$$\varphi_j(t) = \gamma_j \left[L|A_j(0,t)|^2 + 2\sum_{j\neq k} \int_0^L |A_k(0, t - zd)|^2 dz \right] \tag{2.32}$$

where $j = 1 - N$. As seen in the above equation, XPM is also dependent on the relative positions of the pulses $(t - zd)$. The pulses only overlap in a certain time window, because they travel at different velocities in a dispersive medium. The walk-off between the pulses affects the amount of the spectral broadening due to XPM [17].

2.1.4 Numerical solutions to Nonlinear Schrödinger Equation

The full-wave Maxwell equation does not generally have an analytical solution in a nonlinear optical medium. Additionally, numerical solutions are very hard to apply due to the dimensionality problem. However, an approximate solution can be found by using some predefined conditions and assumptions. There are simply two kinds of numerical methods such as pseudospectral and finite difference methods that differ in terms of putting the carrier frequency into the account or not. The finite difference methods include the carrier frequency, they

can calculate forward and backward propagating waves more accurately than pseudo-spectral methods [18]. Split Step Fourier Method is one of the pseudo-spectral numerical methods that is extensively used to solve the NLS equation for the propagation of pulses because of its easy implementation and fast computation [14]. In this study, I utilized the SSFM method to investigate the pulse propagation inside the fiber.

Split Step Fourier Method

The fundamental idea of the SSFM is that the linear and nonlinear parts of NLS equation are treated separately using the analytical solutions of individual parts. Even though NLSE does not have any analytical solution, the individual linear and nonlinear parts have. They can be solved separately with a small numerical error by dividing the propagation distance into small steps (h). As a summary, the linear term due to GVD and nonlinear term due to SPM are defined respectively as [18]:

$$D = -\frac{\alpha}{2} - \sum_{m=2}^{3} \frac{i^{m-1}}{m!} \beta_m \frac{\partial^m}{\partial T^m} \tag{2.33a}$$

$$N = i\gamma \left[|A(z,t)|^2 + \frac{i}{\omega_0 A(z,t)} \frac{\partial}{\partial t} [|A(z,t)|^2 A(z,t)] \right] \tag{2.33b}$$

where $A(z,t)$ is the complex field envelope at distance (z) and time (t). Thus the NLS equation can be written in the form as [18, 19]:

$$\frac{\partial A(z,t)}{\partial z} = (D+N)A(z,t) \tag{2.34}$$

with a general solution of

$$A(z+h,t) = \exp[h(D+N)]A(z,t) \tag{2.35}$$

The solution is approximated by adding the dispersive and nonlinear effects independently over small distance (h) which is divided into two.

$$\exp[h(D+N)] = \exp(hD)\exp(hN) \tag{2.36}$$

The dispersion (D) effect is analyzed in frequency domain, since multiplication is computationally less complex than taking derivative in time domain. Thus, taking the Fourier Transform of both sides by using differentiation theorem, so NLS equation reduces to [18, 19]:

$$\frac{\partial A(z,\omega)}{\partial z} = -\frac{\alpha}{2}A(z,\omega) - \sum_{m=2}^{3}\frac{i^{m-1}}{m!}\beta_m(i\omega)^m A(z,\omega) \tag{2.37}$$

with the solution of

$$A(z+h,\omega) = A(z,\omega)\exp\left\{h\left[-\frac{\alpha}{2} - \sum_{m=2}^{3}\frac{i^{m-1}}{m!}\beta_m(i\omega)^m\right]\right\} \tag{2.38a}$$

$$A(z+h,t) = \mathcal{F}^{-1}\left\{A(z+h,\omega)\right\} \tag{2.38b}$$

In order to reduce the error accumulation more, we employed a modified technique called symmetrized SSFM in our simulations. The general procedure applied in symmetrized SSFM at every h distance is shown step by step below [18, 19]:

i) Dispersion and loss are calculated over h/2 by setting N=0.

$$A\left(z+\frac{h}{2},T\right) = \mathcal{F}^{-1}\left\{\exp\left[\frac{h}{2}D(i\omega)\right]\mathcal{F}\left\{A(z,T)\right\}\right\}$$

ii) At the midpoint of step size, nonlinearity is calculated by setting D=0.

$$A\left(z+\frac{h}{2},T\right)=A\left(z+\frac{h}{2},T\right)\exp(hN)$$

iii) Dispersion and loss is calculated over the second half by setting N=0.

$$A\left(z+h,T\right)=\mathcal{F}^{-1}\left\{\exp\left[\frac{h}{2}D(i\omega)\right]\mathcal{F}\left\{A(z+\frac{h}{2},T)\right\}\right\}$$

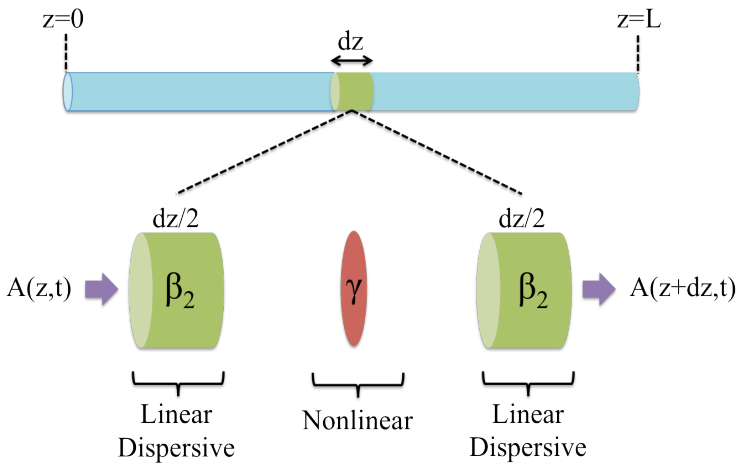

Figure 2.4: Schematic of Split Step Fourier Method [19].

2.2 Optical Amplification

In fiber optic systems, the light intensity is degrading while propagating inside the optical fiber due to material absorption. Fig. 2.5 shows the loss spectrum of Corning SMF-28 single-mode optical fiber. In long-haul fiber communication systems, 1550nm wavelength is employed due to the minimum loss of 0.19 dB/km [20]. Before the invention of optical amplifiers in the 1990s, optoelectronic repeaters or regenerators were utilized to overcome the loss and extend the reach of optical communications links. Such regenerators first convert the optical signal to electric current and then regenerate it via transmitter after amplification

and processing to clean the signal in the electric domain. Even though optical amplifiers are not able to regenerate the signal, they overcome the losses which are generally the main limiting factors. Also, they provide simultaneous amplification of wide-band optical signals through stimulated emission.

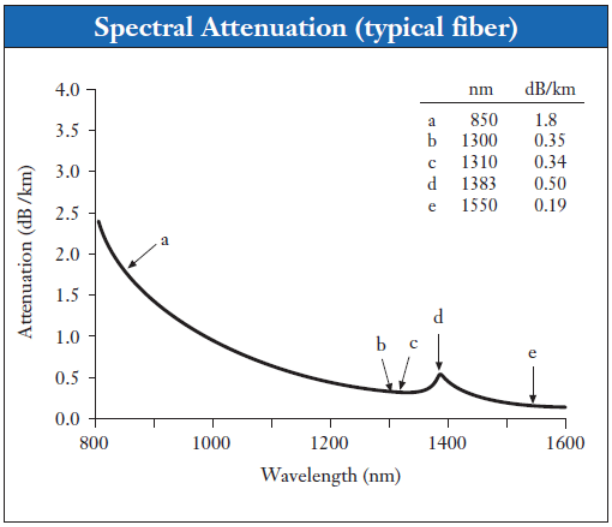

Figure 2.5: Spectral Attenuation of Corning SMF-28 single mode fiber [20].

Optical amplifiers can be categorized by the placement of gain medium as discrete and distributed amplification schemes. In discrete amplification scheme, the lumped amplifiers are placed at discrete positions, i.e. once in 40-60 km for modern fiber-optic communication systems. On the other hand, in distributed amplification, the entire fiber-optic cable link used to propagate signal, is utilized as a gain medium with co-propagating and counter-propagating pumping schemes. Stimulated emission and stimulated Raman Scattering are the physical processes facilitated in these amplification schemes.

2.2.1 Discrete Amplification

The optical amplifiers used in discrete amplification are generally bulky optical devices, which require specially doped fibers to achieve desired gain profile. Erbium-Doped Fiber Amplifier (EDFA) is the most commonly used discrete amplifier where the core of a silica

fiber is doped with Erbium ions. In order to attain gain in communication wavelength (1550 nm), it needs to be efficiently pumped with a laser at a wavelength of 980 nm or 1450 nm [21]. EDFA has a narrowband gain curve and the pump wavelengths are determined by the resonant energy levels of Er atom, as shown in Fig. 2.6. Additionally, EDFA has a slow gain process because of the energy storage at the upper level of Er atom.

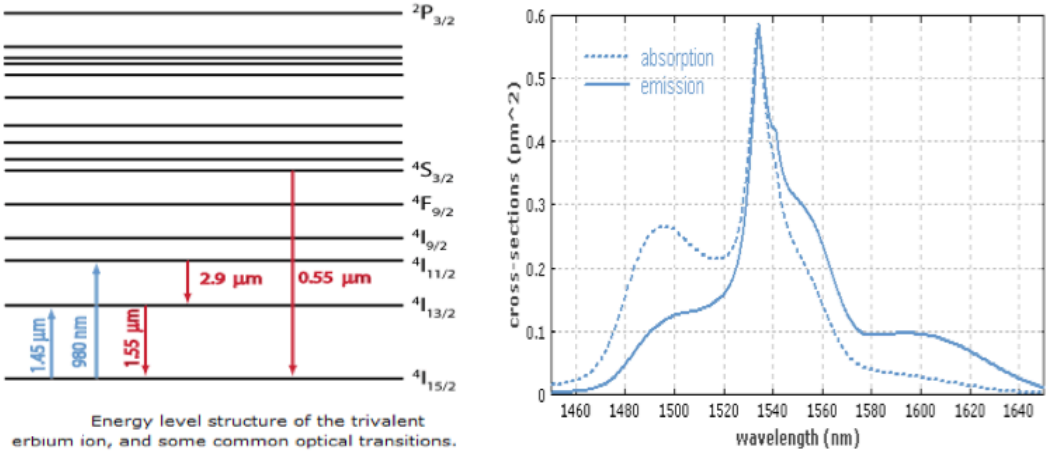

Figure 2.6: Energy level structure of Erbium ion and some optical transitions (a). Absorption and emission cross-sections for Erbium ions in Er: Yb-doped phosphate glass (b) [21].

2.2.2 Stimulated Raman Scattering

In molecular mediums, there is another nonlinear process called Stimulated Raman Scattering that is widely employed in optics to operate optical fibers as an amplifier or tunable laser by transferring energy from one beam (pump) to others (Stokes) [22]. In other words, the weak Stokes wave that has a lower frequency ($E = h\nu$), thus higher wavelength ($\lambda = \upsilon_p/f$), is amplified by the intense (higher frequency) pump beam via SRS process. The vibrational energy states in the medium, as shown in Fig 2.7, determines the amount of energy transfer between the incident and scattered fields.

The pump wave begins to amplify the Stokes wave due to Raman induced energy transfer; when both the pump and probe (Stokes) waves simultaneously propagate inside a fiber. This

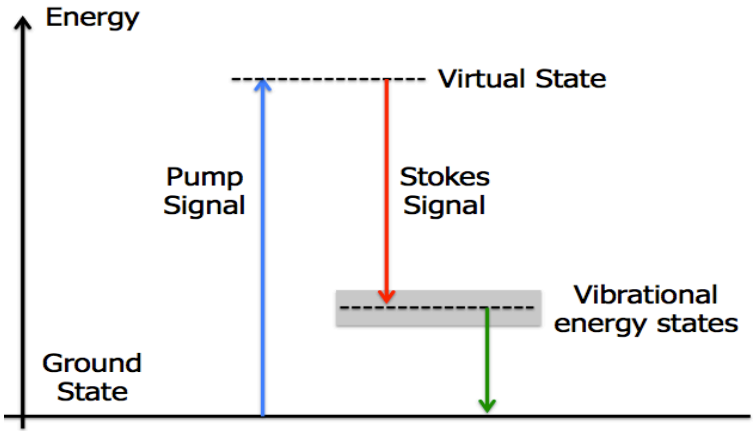

Figure 2.7: Energy Diagram of Raman Scattering [23].

amplification process is governed by the following equation in a lossless medium:

$$\frac{\partial I_S}{\partial z} = g_R I_P I_S \tag{2.39}$$

where I_S and I_P are Stokes and pump waves respectively and g_R is the Raman gain coefficient [24], which is a function of frequency shift ($\Omega = \omega_P - \omega_S$) between the pump and Stokes waves, and depends on the composition of the fiber core, relative polarization of both fields (co-polarized or orthogonally polarized) and inversely proportional to the pump wavelength [25]. The silica fibers have a very wide Raman gain spectrum up to 40THz due to its amorphous nature. As it is seen in the co-polarized case of Fig. 2.8(b), the first peak is nearly at 13.2THz and the second peak is at 14.7THz due to non-crystalline nature of silica glass [14]. The multiple peaks exist since several vibrational modes contribute to the gain spectra. However, the spectra can be modeled by a single-peaked function like polynomial, Gaussian or Lorentzian with the loss of some fine structures [26].

As it is mentioned earlier, the stimulated Raman scattering occurs when both pump and probe beams propagate at the same time. The amplification lasts until the frequency shift lies inside the bandwidth of gain spectra. On the other hand, new frequency components can be generated and amplified by spontaneous Raman scattering, even the initial probe beam

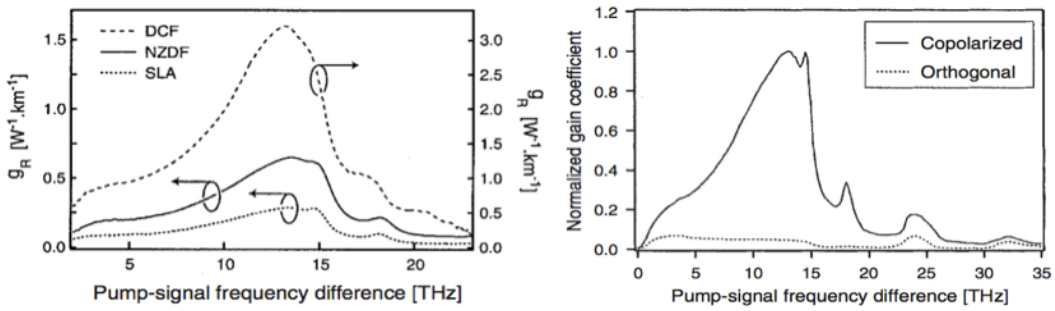

Figure 2.8: Raman gain spectrum of silica fiber and the effect of intensity (a), which depends on the type of fibers and the polarization states (b) on Raman gain coefficient [26].

does not exist. Although photons within the 40THz bandwidth are generated and amplified, the frequency component which experiences the maximum Raman gain dominates the system due to higher amplification. As a result, in silica fibers, nearly 13.2 THz downshifted Stokes wave is generated. The technique enables to generate 26.4-29.4THz ($\sim$1000cm^{-1}) frequency separated second-order Stokes pulses with $\sim$3THz ($\sim$40nm) tunability. This property leads to the design of multi-wavelength stable soliton Raman lasers.

For the simplest case, the signal is pumped by single continuous wave (CW) laser, the evolution of pump and the probe beams is governed by the following equations including both the fiber losses and the interaction between them through SRS process [14].

$$\frac{\partial I_S}{\partial z} = g_R I_P I_S - \alpha_S I_S \tag{2.40a}$$

$$\frac{\partial I_P}{\partial z} = -\frac{\omega_P}{\omega_S} g_R I_P I_S - \alpha_P I_P \tag{2.40b}$$

where α_P and α_S are the fiber loss coefficients for pump and Stokes frequencies (ω_P and ω_S), respectively. Additionally, the coefficient $\frac{\omega_P}{\omega_S} > 1$ indicates that the energy supplied by the pump beam is more than the energy gained by the Stokes. Rest of the energy is lost in the system as heat via collisions.

The above differential equations do not have any analytical solution. However, for the small

signal case ($I_S \ll I_P$), the pump depletion due to the amplification process can be neglected (first term in Eq. (2.40b)) and hence the solution becomes:

$$I_P(z = L) = I_0 \exp(-\alpha_P L) \tag{2.41a}$$

$$I_S(z = L) = I_S(0) \exp(g_R I_0 L_{eff} - \alpha_S L) \tag{2.41b}$$

where I_0 is the incident pump intensity, L is the propagation length and $L_{eff} = \frac{1-\exp(-\alpha L)}{\alpha}$ is the effective length. The gain term should be greater than the loss term to build up Stokes wave inside the fiber. This solution can only be applied for the initial stages of Raman amplification because the small-signal approximation will not be valid for so long due to pump depletion while amplifying Stokes.

2.2.3 Distributed Amplification

A flat gain Raman amplifier, based on stimulated Raman scattering, needs to be designed to provide a uniform amplification for the broadband signal. As mentioned earlier, the fiber becomes the gain medium for the Raman amplification when properly pumped that causes pump depletion due to long fiber lengths [16]. In order to have more uniform amplification along the fiber, bidirectional (hybrid) pumping schemes consist of co-pumping (signal direction) and counter-pumping (opposite direction) may be facilitated, as shown in Fig. 2.9.

The distributed Raman amplification becomes a great alternative to discrete amplification in terms of feasibility, achievable gain bandwidth, uniformity and the signal-to-noise ratio (SNR). The main advantages are as follow:

1. Raman amplification enables a fast gain mechanism since it employs a simultaneous

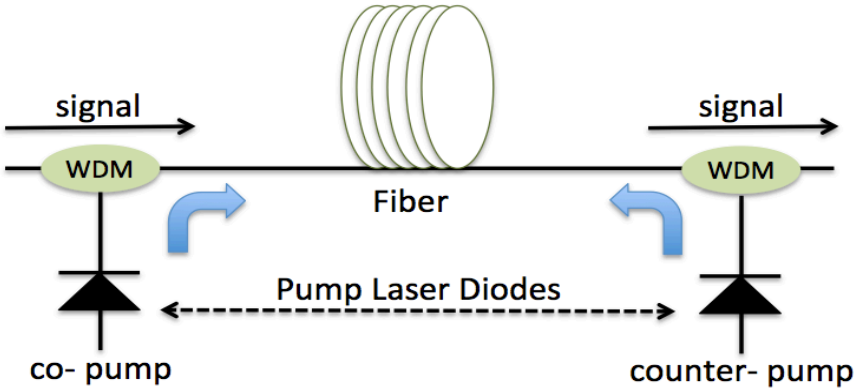

Figure 2.9: The schematics of the Raman amplifier including co/counter pump laser diodes [19].

process, SRS [16].

2. Raman amplification keeps the signal level inside the safe region through gain distribution over a long distance. In other words, it prevents the signals to reach high power levels where nonlinear effects are powerful and to drop below the noise floor where noise interference is drastic [27]. Kalyoncu et al. state that the distributed amplification provides up to 16dB higher SNR corresponding to 2.5 bit higher resolution in TS-ADC setup [28].

3. Broadband and uniform spectral gain profile can be acquired with using multi pumping schemes and selecting appropriate pump wavelengths and the powers.

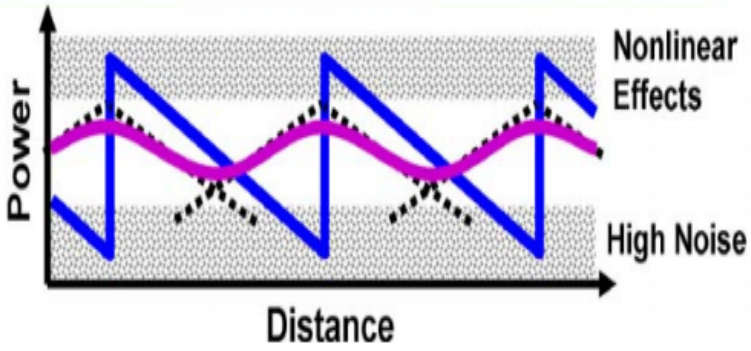

Figure 2.10: The signal level dynamics inside the fiber with discrete (blue) and distributed amplification (red) [27].

The multi-pumped Raman amplifier is modeled by including all signal-to-signal (pump-pump, pump-signal and signal-signal) interactions and the wavelength dependent attenuation (α_k). The following set of equations determines the evolution of all signal and pump powers along the Raman amplified system [19].

$$\pm\frac{dP_k}{dz} = -\alpha_k P_k + \sum_{j=1}^{k-1} g_{\lambda_j}(\lambda_k - \lambda_j)P_j P_k - \sum_{j=k+1}^{N} \frac{\lambda_j}{\lambda_k} g_{\lambda_k}(\lambda_j - \lambda_k)P_j P_k \tag{2.42}$$

where $k = 1, 2, \ldots, N$, +/- corresponds to co/counter propagating signals, P_k is the pump/signal power, α_k is the wavelength dependent attenuation coefficient and g_{λ_j} is the Raman gain coefficient for the signal at wavelength λ_j which is proportional to reference gain coefficient at λ_0 as $g_{\lambda_j}(\Delta\lambda) = \frac{\lambda_j}{\lambda_0} g_{\lambda_0}(\Delta\lambda)$. The first term on the right side of the equation represents the wavelength dependent fiber attenuation. The second term is the gain introduced on the signal at wavelength λ_k by the other signals with higher frequencies, $\lambda_j, j = 1, \ldots, k-1$. The last term, on the other hand, represents the pump depletion on the signal at wavelength λ_k due to power transfer to the other signals with lower frequencies, $\lambda_j, j = k+1, \ldots, N$ [19].

The set of equations above cannot be solved analytically, therefore numerical approaches such as generic and shooting algorithms, are generally used to calculate the proper pump wavelengths and powers to obtain the desired uniform wideband gain profile.

Chapter 3

Multi-tone Continuous Wave Lidar

3.1 Introduction

Light detection and ranging (Lidar) has been used in various ways such as military applications [1] and atmospheric sciences [2] to detect remote objects, measure distances [3], create topographical images [4], detect aerosol particles [29, 5], and measure ozone layers [6, 7]. In recent years, with the advent of self-driving cars and unmanned aerial vehicles (UAV), Lidar became a topic of interest once again for proximity sensing and collision prevention [30, 31, 8, 32, 33, 34]. However, most of these recent research activities focus on the receiver architectures [35], and signal processing techniques [36, 37] to achieve more robust, accurate and sensitive measurements in longer ranges. Optical backbone mostly relies on Lidar technologies based on pulsed time of flight (PToF) measurements, which transmits laser impulses and collects the scattered light from a target. The measured time delay between transmission and the reception reveals the range information by using simple calculations. To achieve accurate timing, PToF Lidars require short pulse generation and high temporal resolution, which creates the necessity of fast electronics. Therefore, several consecutive measurements

are performed in combination with Monte Carlo methods to minimize the error in timing. Additionally, the precision of this approach degrades with distance, also it lacks the ability to detect velocity and direction of moving targets simultaneously [10].

Recently, new Lidar technologies employing continuous wave (CW) lasers emerged as in amplitude modulated continuous wave (AMCW), and frequency modulated continuous wave (FMCW) Lidars [38, 39, 40]. The AMCW Lidars modulate the intensity of the light while keeping the frequency constant. Depending on the desired measurement precision, AMCW technique requires high-speed radio-frequency (RF) electronics to modulate the light intensity. On the receiver side, this requirement can be mitigated via demodulation or superheterodyne receivers that can convert the high-frequency tones into base-band signals. The range information is either obtained by convolving the local oscillator with the time-delayed return signal as in phase shift Lidars, or electronic heterodyne detection to generate a beat note proportional to the target distance as in linearly chirped Lidars [10, 38]. Previously, <5mm precision was reported for distances <12m by employing AMCW Lidars directly modulated with <20MHz RF signal and applying precision improvement techniques such as multiple signal classification and harmonic distortion cancellation [41, 42, 43].

Moreover, the FMCW Lidars are based on frequency sweeping of the light sources such as tunable lasers or frequency modulated CW lasers with a chirped RF signal. The backscattered signal is detected via optical heterodyning that employs a slow square-law detector, therefore the generated beating frequency can be recorded by slower electronics [10]. Since the same target is measured with several frequencies, the results are more robust and accurate [38]. Also, FMCW Lidars have the potential of detecting the speed and direction of the target simultaneously [44, 45]. Additionally, FMCW Lidar systems can achieve sub-mm resolutions for shorter ranges (<10m), while utilizing wide-band frequency tuning via swept sources [46, 47, 48]. The resolution degrades to ∼5cm at medium ranges (∼100m), with a bandwidth that is limited to 5GHz [49]. However, in the practical domain, frequency stabil-

ity of the laser source and technical challenges limit the sweeping frequency range up to a few GHz, therefore the range resolution is limited to cm level, which mitigates the reliability of frequency chirped Lidars [50, 51]. Very recently, frequency combs are utilized to achieve >THz bandwidth with μm resolutions in shorter ranges [52]. On the other hand, some frequency domain Lidars previously employed the multiple-wavelength techniques such as continuous time-of-flight measurements [53], multi-wavelength super-heterodyning [54, 55] and multi-frequency demodulation via CMOS photonic mixer devices [56], which were used for short-range and high precision imaging and ranging. However, it is important to note that these efforts are mainly targeted for short-range measurements in applications such as Microsoft Kinect.

In addition to AMCW and FMCW, phase-based ranging is also a remarkable technique for absolute metrology systems [57]. However, implementation of such a system is troublesome due to the requirement of multiple detectors or detector arrays, as well as heterodyne detection of two arms with different frequencies. Also, the detection in such applications requires either phase detectors or elaborates phase extraction techniques during post-processing. Lack of direct velocity measurement is another drawback of such techniques. Therefore, a less burdensome system is necessary with high-resolution capability for longer ranges that can also provide the velocity information simultaneously.

Here, we present a multi-tone modulated continuous wave (MTCW) Lidar technology that can provide high precision range and velocity information of static and moving targets. In the proposed approach, CW lasers are simultaneously modulated with a few carefully selected RF tones. At the receiver, the interference of the scattered light with the reference is detected by a photodiode. Since, the acquired light travels to the target and back to the beam splitter, the interference signal carries the range and velocity information of the target at the amplitude and phase of the detected RF tones. We utilize the relative amplitude variations in RF tones to extract the range and velocity information. In this chapter, the proposed

MTCW Lidar system is investigated theoretically and verified with numerical simulations. Also, a proof of principle experiment has been performed for ranging from a static target. We show the short-distance range measurements with <1cm accuracy by using 2.5GHz and 6GHz RF tones. The accuracy can be further improved by increasing the tone frequencies, data extrapolation, and signal processing algorithms. Recent progress in the development of highly coherent narrow-linewidth lasers allows practical devices that can operate over kilometers of distances. As a result, the proposed method can be suitable for aerial or satellite-based remote sensing applications with cm accuracy.

3.2 Lidar Range Measurements

3.2.1 Principle and Numerical Results

Figure 3.1 illustrates the schematic of the MTCW Lidar system. The system is driven by a CW laser source that is amplitude modulated by a Lithium Niobate ($LiNbO_3$) modulator to create well separated optical tones. The signal is then split into two as the reference and the measurement arms. The measurement signal is incident on the target after collimation and beam expansion. The reflected beam is then collected back at the same transmit aperture or a separate collection aperture. After collecting the reflected signal, it is collimated back and sent to an interferometer that enables the superposition of the transmit signal and the reference signal on a detector. The photodetector is used to detect the interference and create RF tones required for range finding and velocimetry. In particular, we are interested in the relative amplitude variations of modulation tones to extract the range information. Due to the difference in the phase accumulation at different optical tones at a given target distance, we will have nonuniform amplitudes across the RF frequencies. By carefully evaluating the strength of the tone powers, we can estimate the path length covered by the optical beam

from the source, to the target and back to the detector. In this study, we have developed an algorithm that recognizes the amplitude nonuniformity across the harmonic frequencies and precisely detect the range information from these amplitude variations. If there is a moving target, it is also possible to detect the Doppler shift to identify the velocity and direction with the same configuration. The number of RF tones and their frequencies are selected carefully for the desired range and precision. Consequently, the proposed method is employing multi-tone RF modulation, optical heterodyning and sine fitting algorithms that enable acquisition of range and possible velocity information in a single shot measurement by eliminating the need of frequency, amplitude or phase sweeping.

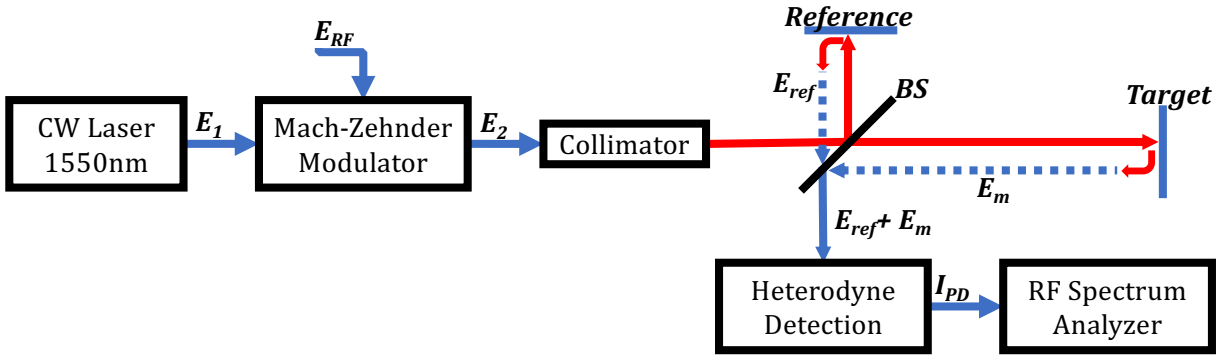

Figure 3.1: Schematic of the proposed multi-tone continuous wave Lidar system

Analytical modeling

The unmodulated complex optical field at the output of the CW laser can be modeled as

$$E_1 = A_0 exp(j\omega_0 t + j\phi_0) exp(-jk_0 z) \tag{3.1}$$

where A_0 is the amplitude of the lights electric field, ω_0 is the angular frequency of the optical carrier, ϕ_0 is the phase of the initial light beam, k_0 is the angular wave number, and z is the propagation distance [58]. Later, this optical carrier is intensity modulated by a waveform

that is the sum of sinusoidal signals,

$$E_{RF} = \sum_{i=1}^{N} A_i cos(2\pi f_i t + \phi_i) = \sum_{i=1}^{N} \frac{A_i}{2}[exp(j2\pi f_i t + j\phi_i) + exp(-j2\pi f_i t - j\phi_i)] \quad (3.2)$$

where A_i, f_i, and ϕ_i are the amplitude, frequency, and phase of ith RF tone, respectively. The field transfer function of the balanced driven Mach Zehnder modulator (MZM) under push-pull configuration is $cos(0.5\pi \frac{v_m}{V_\pi})$ where $v_m = \frac{V_\pi}{2} + E_{RF}$ at quadrature bias. Therefore, after trigonometric conversions, the transfer function of MZM can be rewritten as

$$cos(\frac{\pi}{4} + \frac{\pi}{2V_\pi} E_{RF}) = \frac{1}{\sqrt{2}}[cos(\frac{\pi}{2V_\pi} E_{RF}) - sin(\frac{\pi}{2V_\pi} E_{RF})] \quad (3.3)$$

To achieve linear modulation, we used low modulation depth ($m = \pi \frac{A_i}{V_\pi} \ll 1$), therefore modulated electric field can be expressed by

$$E_2 = \frac{E_1}{\sqrt{2}} - \frac{E_1}{\sqrt{2}} \frac{\pi}{2V_\pi} E_{RF} \quad (3.4)$$

by using small angle approximations. After inserting E_1 and E_{RF},

$$E_2 = \frac{A_0}{\sqrt{2}} exp(j\omega_0 t + j\phi_0 - jk_0 z) - \frac{mA_0}{4\sqrt{2}} \sum_{i=1}^{N} exp(j(\omega_0 + 2\pi f_i)t + j(\phi_0 + \phi_i) - jk_0 z) + exp(j(\omega_0 - 2\pi f_i)t + j(\phi_0 - \phi_i) - jk_0 z) \quad (3.5)$$

where all the RF tone amplitudes are selected equal, therefore the modulation depth, m, is the same for all RF tones. Later, modulated light is transferred to the free space through a collimator and split into two via a beam splitter. While one signal is traveling to the target (measurement signal), the other is kept inside the system to be used as a local oscillator (reference signal) in coherent detection. Both signals accumulate phase during propagation,

and the returned signals at the detector can be represented as

$$\begin{aligned} E_{ref,m} &= \frac{A_0}{2\sqrt{2}}\alpha_{ref,m} exp(j\omega_0 t + j\phi_0 + j\omega_0 \frac{2L_{ref,m}}{c}) \\ -m\frac{A_0}{4\sqrt{2}}\alpha_{ref,m} \sum_{i=1}^{N} & exp[j(\omega_0 + 2\pi f_i)t + j(\phi_0 + \phi_i) + j(\omega_0 + 2\pi f_i)\frac{2L_{ref,m}}{c}] \\ & + exp[j(\omega_0 - 2\pi f_i)t + j(\phi_0 - \phi_i) + j(\omega_0 - 2\pi f_i)\frac{2L_{ref,m}}{c}] \end{aligned} \tag{3.6}$$

where L_{ref} and L_m are the distances between the beam splitter - reference mirror and beam splitter - target, respectively. Also, α_{ref} and α_m are the linear loss coefficients of free-space propagation. On the detector, the reference and measurement signals will be mixed, and the current output of the PIN photodiode will be

$$I_{PD} = RP_{in} = R(E_{ref} + E_m)(E_{ref} + E_m)^* \tag{3.7}$$

where R is the responsivity of the detector and P_{in} is input optical power on the detector. The phase shift of each tone will convert into amplitude variations at different RF tones as:

$$\begin{aligned} I_{PD} = I_{PD,ave} - \frac{1}{4}RmA_0^2 \sum_{i=1}^{N} & (\alpha_{ref}^2 + \alpha_{ref}\alpha_m) cos(2\pi f_i t + \frac{4\pi}{c} L_{ref} f_i) \\ & + (\alpha_{ref}\alpha_m + \alpha_m^2) cos(2\pi f_i t + \frac{4\pi}{c} L_m f_i) \end{aligned} \tag{3.8}$$

where $I_{PD,ave}$ is the average photodiode current which is the sum of all self-beating components.

This result assumes that we can ignore higher-order distortion tones and phase mismatch is generated by only the optical path difference between the reference arm and the measurement arm. However, the sinusoidal transfer function of the modulator can only be assumed linear for a small region around the quadrature bias point. We can drive the modulator in the linear regime by keeping the amplitude of the RF tones small. Then, the higher-order distortion terms will be suppressed at a much faster rate than the fundamental tones. For example,

even-order harmonic distortion tones (HD2, HD4, ...) will be suppressed entirely if the modulator is biased at the quadrature point. Therefore, 3rd order harmonic distortion (HD3) and intermodulation distortion tones (IMD3) will limit the system performance. However, they are proportional to the cube of the modulation depth ($P_{HD3} \propto m^3$, $P_{IMD3} \propto m^3$) while fundamental tone is directly proportional to the modulation depth ($P_{fund} \propto m$). Therefore, the spur free dynamic range (SFDR) of the system will be improved with decreasing modulation depth [59]. However, it will also limit the transmitted RF tone power. To overcome the high losses in Lidar systems, it is crucial to increase the modulation depth, therefore other linearization techniques [60, 61, 62] need to be employed.

On the other hand, careful selection of modulation frequencies may eliminate the requirement for linearization. If the distortion tones do not overlap with the fundamental tones, nonlinear modulator behavior can be seen as an opportunity instead of a problem. It is possible to optimize modulation depth to utilize distortion tones as extra measurement tools after isolating the intensity variations due to the mixing of tones. If one can overcome the computation complexity, this will further improve the tone powers and system accuracy.

As is clear in Eq. 3.8, each RF frequency tone, f_i, accumulates different phase while the light is traveling towards the target. Therefore, interference of the backscattered light with the reference will produce a difference in amplitudes for different tones. After recording the power of each tone, the data points are fit into a sinusoidal signal to extract the frequencies, where the reference and measurement signals interfere constructively or destructively. The frequency difference between two consecutive peaks, $\Delta f = |f_{p2} - f_{p1}|$, will determine the range information such as

$$\frac{4\pi}{c}\Delta L(f_{p2} - f_{p1}) = 2\pi \Longrightarrow \Delta L = \frac{c}{2\Delta f} \tag{3.9}$$

where ΔL is the absolute range difference, $\Delta L = |L_m - L_{ref}|$.

In MTCW Lidar, we are specifically interested in the sinusoidal fit over the measured tone powers as shown in Fig. 3.2. The amplitude of such fitting depends on the experienced loss in the reference and measurement arms. Peak amplitude is achieved when two cosines are in phase and the minimum amplitude is achieved when two cosines are entirely out of phase. Therefore, the amplitude of modulation is $A_{fit} = \frac{1}{4}RmA_0^2\alpha_m(\alpha_{ref} + \alpha_m)$, the extinction ratio is $ER = \frac{\alpha_{ref}+\alpha_m}{|\alpha_{ref}-\alpha_m|} \implies 1$ when $\alpha_m \ll \alpha_{ref}$ and modulation depth of the oscillation is $m_{osc} = \alpha_m/\alpha_{ref}$. Since the backscattered power from the target is so low, the reference arm should be attenuated to preserve the extinction ratio and modulation depth of the oscillation. However, RF heterodyne detection can be pursued in the electrical domain to further enhance the signal-to-noise ratio (SNR) of the detection system.

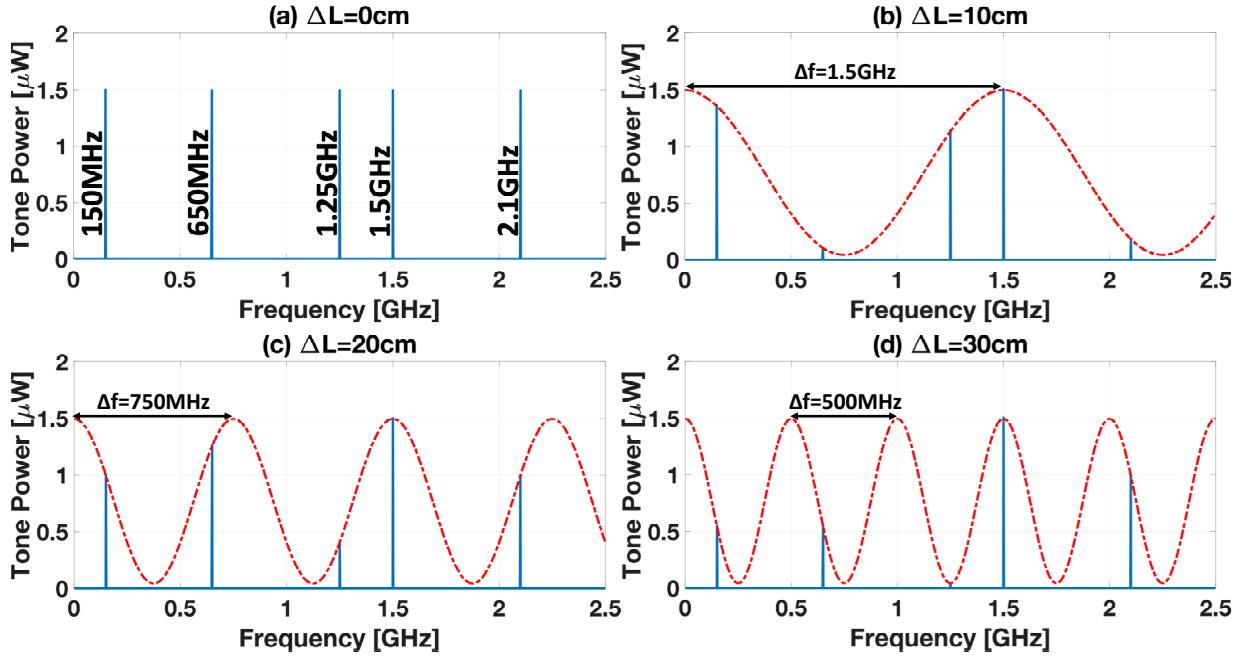

Figure 3.2: RF tone power variation for various target distances and corresponding frequencies

Numerical verification

We modeled the full system of the proposed MTCW Lidar in the computer environment that includes the modulator and detector nonlinearities, laser and detector noises, and losses in the measurement arm to verify the experimental results. In Fig. 3.2, the evolution of the tone powers is demonstrated while the range of the target is moved up to 30cm from its initial position with 1μm steps. Also, the wavelength of the laser is selected as 1μm to eliminate the mismatch between the optical carriers. Additionally, the modulation depth is set to 10% and losses are neglected ($\alpha_{ref} \approx \alpha_m \approx 1$). To eliminate overlapping of actual tones with higher-order distortions such as harmonic distortions ($2f, 3f, \ldots$) and intermodulation distortion ($2f_2 \pm f_1, 2f_1 \pm f_2, \ldots$), we selected RF tones as 150MHz, 650MHz, 1.25GHz, 1.5GHz and 2.1GHz with the same amplitude as shown in Fig. 3.2(a).

When the target is 10cm away, the light propagates a total distance of 20cm back and forth from the target by creating peaks at every 1.5GHz. While the 1.5GHz tone has the same amplitude as before, 650MHz is degraded the most due to the proximity to the valley point at 750MHz that experience the complete destructive interference at the detector as seen in Fig. 3.2(b). When the target distance is doubled and tripled as in Fig. 3.2(c) and Fig. 3.2(d), respectively, the period of the sinusoidal fit decreases accordingly. Therefore, to achieve high resolutions, larger bandwidth is required. For example, by facilitating 50GHz RF bandwidth, the system can achieve <1mm resolution. Such higher resolutions can also be achieved by extrapolating the data of the lower frequency tones and signal processing without going to X-band modulation. When the target range increases, the consecutive peaks of the sinusoidal fit get closer to each other due to inverse proportionality of range and frequency as in $\Delta L = 0.5c/\Delta f$. However, the same modulation pattern repeats itself according to the period of the greatest common divisor (GCD) of all RF tones. For the given tones GCD is 50MHz, therefore the same modulation pattern is repeating itself in every 3 meters. This MTCW system is designed for the fine range measurements at the last portion

of true range information (L_{act}) that can be represented as $L_{act} = NL_{rep} + L_f$, where L_{rep} is the distance of modulation pattern repetition and L_f is the final range information that can be extracted from this system. However, it is not possible to extract the number of repetitions (N) directly. Using quasi-CW signals can eliminate uncertainty and act as coarse range measurement. For instance, in the case of autonomous vehicles, the 300m operation range requires 2μs light propagation. The pulsed modulation with 100kHz repetition rate and 50% duty cycle can yield sufficient time (>3μs) to acquire enough data for averaging. Also, it is possible to further increase the data acquisition time by increasing the duty cycle or decreasing the repetition rate.

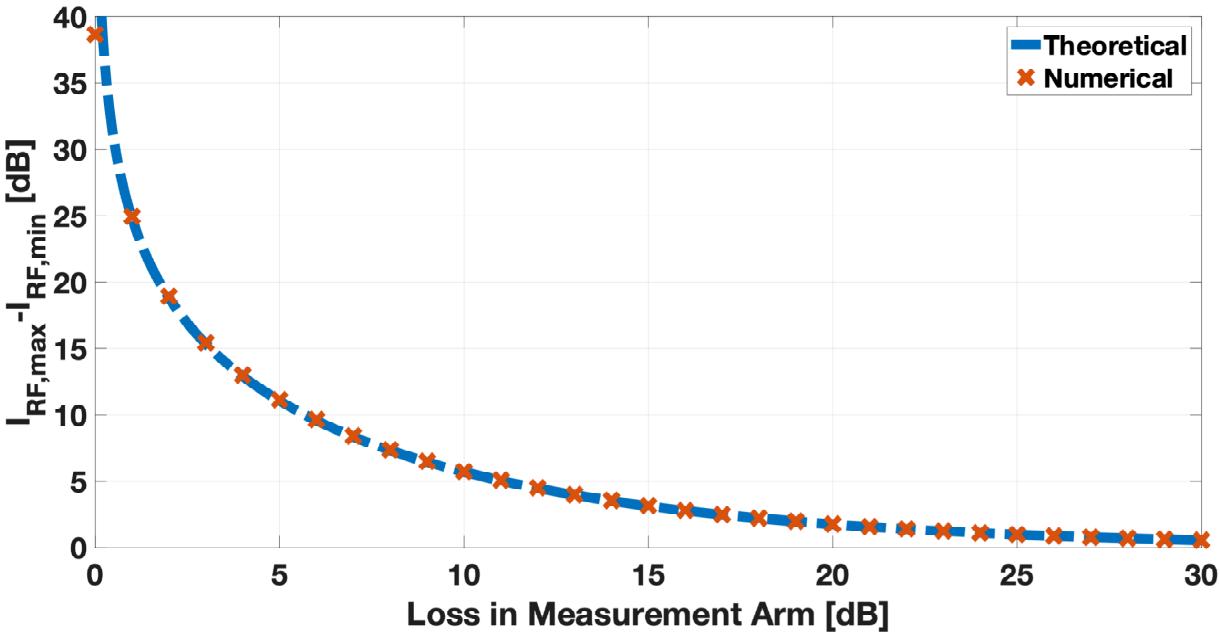

Figure 3.3: The effect of measurement arm loss on the extinction ratio of the sinusoidal fit when there is no loss in the reference arm.

There is a trade-off between the modulation depth and sensitivity of the system. Figure 3.3 demonstrates how the extinction ratio of the sinusoidal fit is decreasing while the backscattered signal is being attenuated with respect to the reference signal according to the decibel

representation of extinction ratio formula.

$$ER = \frac{I_{RF,max}}{I_{RF,min}} = \frac{\alpha_{ref} + \alpha_m}{|\alpha_{ref} - \alpha_m|} \tag{3.10a}$$

$$ER[dB] = I_{RF,max}[dB] - I_{RF,min}[dB] \tag{3.10b}$$

$$ER[dB] = 10log_{10}(\alpha_{ref} + \alpha_m) - 10log_{10}(|\alpha_{ref} - \alpha_m|) \tag{3.10c}$$

When a high reference power is used, the coherent detection allows you to detect lower scattering powers, however, the variation between the constructive and destructive interference is mitigated. Therefore, the reference power should be optimized for the desired application based on the loss in the measurement arm that is due to divergence, range, and scattering efficiency.

3.2.2 Experimental verification

To demonstrate the system performance, the proposed Lidar system is established on the optical table as shown in Fig. 3.4. We used a CW laser operating at 1550nm with 14mW average power. The laser output is sent to an 8GHz LiNbO3 MZM to modulate light with the sum of two RF tones. Two RF tones generated by Agilent RF Signal Generators are combined with a coaxial 2-way power combiner (RFPC) and fed into modulators RF port. Quadrature bias operation of the MZM is ensured by a DC power supply. The modulated light is first amplified by an Erbium-doped fiber amplifier (EDFA) with 10dB gain and transferred to the free space via a collimator with 2.1mm beam waist and 0.95mrad beam divergence. The transmitted beam is further split into two through a non-polarizing 50-50 beam splitter (BS) cube. In this experiment, for demonstration purposes, we used Aluminum mirrors with >95% reflectivity as a target and reference, hence $\alpha_{ref} \approx \alpha_m \approx 1$. The target mirror is translated on an optical rail for coarse measurements, then on an integrated micrometer

stage for fine-tuning. The current setup is used for the proof of principle of ranging only, therefore the target is stationary and not yielding any Doppler shifts for speed profiling. However, the velocimetry capability of a similar configuration is recently demonstrated for an oscillating target [63]. The back-reflected signals from the mirrors are recombined on the same beam splitter and directed to the heterodyne detection mechanism. As a detector, we used a fiber-coupled InGaAs PIN photodiode (PD) with >12.5GHz bandwidth. For these proof of concept experiments, it is sufficient to use a PIN photodiode, which has an active area diameter of 32μm that can detect as low as >5μW. Since such a high bandwidth requires small active area, which reduces the sensitivity of the detector, in a more realistic system an avalanche photodetector (APD) should be considered to enhance the detection capability by three orders of magnitude. A free space to fiber coupling system is built with a coupling efficiency >25%, by utilizing 3D micrometer stages and a 10× objective lens with a numerical aperture of 0.25. After coupling to the fiber, through a 90/10 power splitter, the average power is observed by an optical power meter (OPM), while spectral measurements are performed by an RF Spectrum Analyzer (RFSA). The acquired spectra are recorded and further post-processed in MATLAB to extract the range information via sinusoidal fitting algorithms.

3.2.3 Results and discussion

For proof of concept demonstration, two experiments are performed: (i) frequency sweeping of a stationary target anchored at a fixed distance and (ii) measuring the powers of two tones for a target that is placed at different distances.

Figure 3.5 demonstrates the frequency sweeping of a target at fixed range, where red dots represent the experimental data points and blue curve the numerical expectation. The two consecutive peaks are observed at DC and 1.4GHz indicating $\Delta f = 1.4GHz \implies \frac{c}{2\Delta f} =$

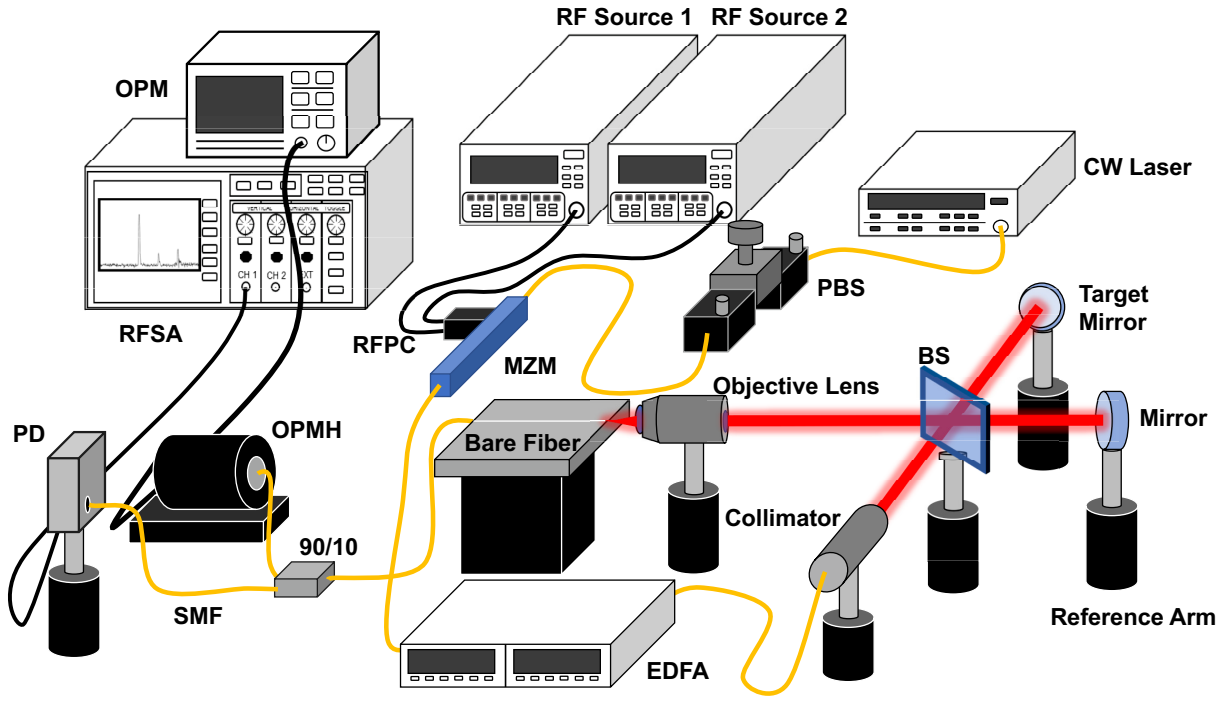

Figure 3.4: Full experimental setup of MTCW Lidar

10.71cm, along with the destructive interference occurring at the 700MHz tone. Due to a greater loss in the measurement arm, where $\alpha_m/\alpha_{ref} \approx 0.8$, constructive interference is achieved as ∼5.1dB higher than the reference. As is clear, the experimental data are well-matched with the numerical analysis. The mismatch between the experiment and the numerical expectation is shown in Fig. 3.5(b), where the root-mean-square (RMS) error is calculated as 0.0936.

This experiment is used as a calibration for the proposed MTCW Lidar system. Since, several components in the experimental setup, such as RF path and MZM, have frequency dependency, the detected signal amplitudes have variations across the RF frequencies due to these imperfections. To eliminate such variations, we normalized the acquired interference powers with respect to the reference signal power that is measured while blocking the measurement arm. In Fig. 3.5(a), 0dB line shows the reference signal power. In the complete system, after system calibration, pre-distortion can be applied to the tones to equate the power levels and eliminate the need for calibration experiment.

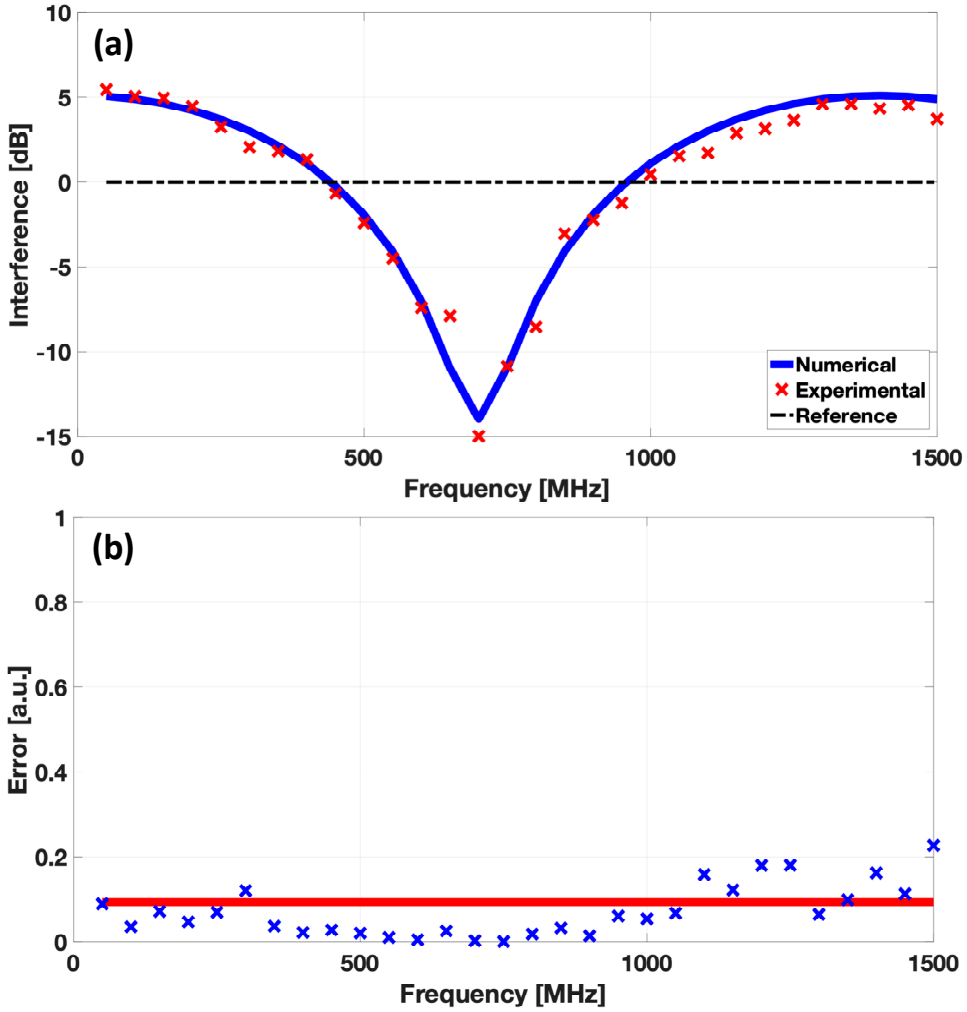

Figure 3.5: (a) Frequency sweeping for a stationary target sitting at a fixed distance (10.71cm). Intensities are normalized with respect to the reference signal. (b) The calculated error between experimental data and theoretical expectation for frequency sweeping.

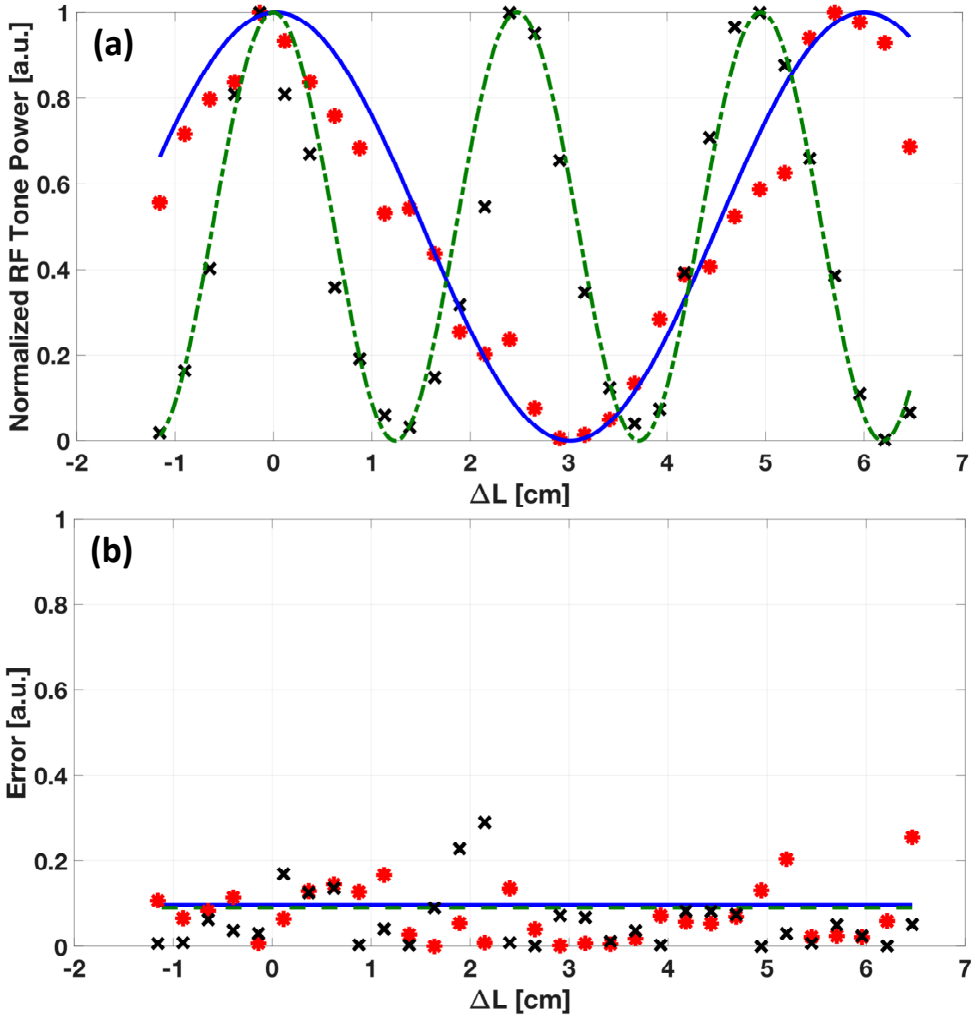

Figure 3.6: (a) Multi-tone measurement by using two tones at 2.5GHz and 6GHz (b) Calculated error between experimental data and theoretical expectation for individual tones at 2.5GHz (dots) and 6GHz (crosses) in the multi-tone measurement system. RMS error values at 2.5GHz and 6GHz are represented as solid and dashed lines respectively.

In the second experiment, we modulate the CW laser by using two RF tones at 2.5GHz and 6GHz, and the measurement arm is moved slowly to observe the interference. Fig. 3.6(a) shows that 2.5GHz and 6GHz tones are forming waveforms with 6cm and 2.5cm periods, respectively. The results are in a perfect correlation with the theoretical expectations. Fig. 3.6(b) indicates the amount of error in the system at each measurement distance for individual tones. The RMS error of the system is calculated from the error graph as 0.0972 and 0.0905 for 2.5GHz and 6GHz tones, respectively.

We note that 6GHz RF bandwidth is sufficient to resolve 2.5cm with a full cycle. It is also possible to add more tones at lower frequencies without increasing the total RF bandwidth of 6GHz and further applying signal processing to achieve higher resolution. Fig. 3.7(a) demonstrates 5mm range resolution by applying curve fitting and data extrapolation. Normally, 30GHz RF bandwidth is required to achieve 5mm resolution. However, extending the bandwidth or improving the resolution through data extrapolation is possible if the SNR of the detected signal is high enough. The behavior of the system for different ranges of extrapolation for a higher resolution can be seen in Fig. 3.7(b). As we extrapolate the fit based on a few low-frequency tones, the amplitude difference between these tones becomes very crucial. The ideal case (full cycle) and the 2× bandwidth extension (half cycle) results are overlapping as shown in Fig. 3.7(b). This is due to true bandwidths capability of capturing constructive interference at low frequencies and destructive at high. For bandwidth efficiency purposes, careful selection of RF tones plays a significant role. Then, it is possible to utilize the double bandwidth entirely without facing any penalties. Further improvements can be performed depending on the SNR and modulation depth of the detected signal. The SNR depends on the incident beam power, detector sensitivity and divergence of the beam. In the actual practice, utilizing a high average output power laser and increasing the collection efficiency via carefully engineered collection optics will enhance the signal strength along with an amplified APD. In addition, it is also possible to increase the signal level by applying RF heterodyning after the optical detector.

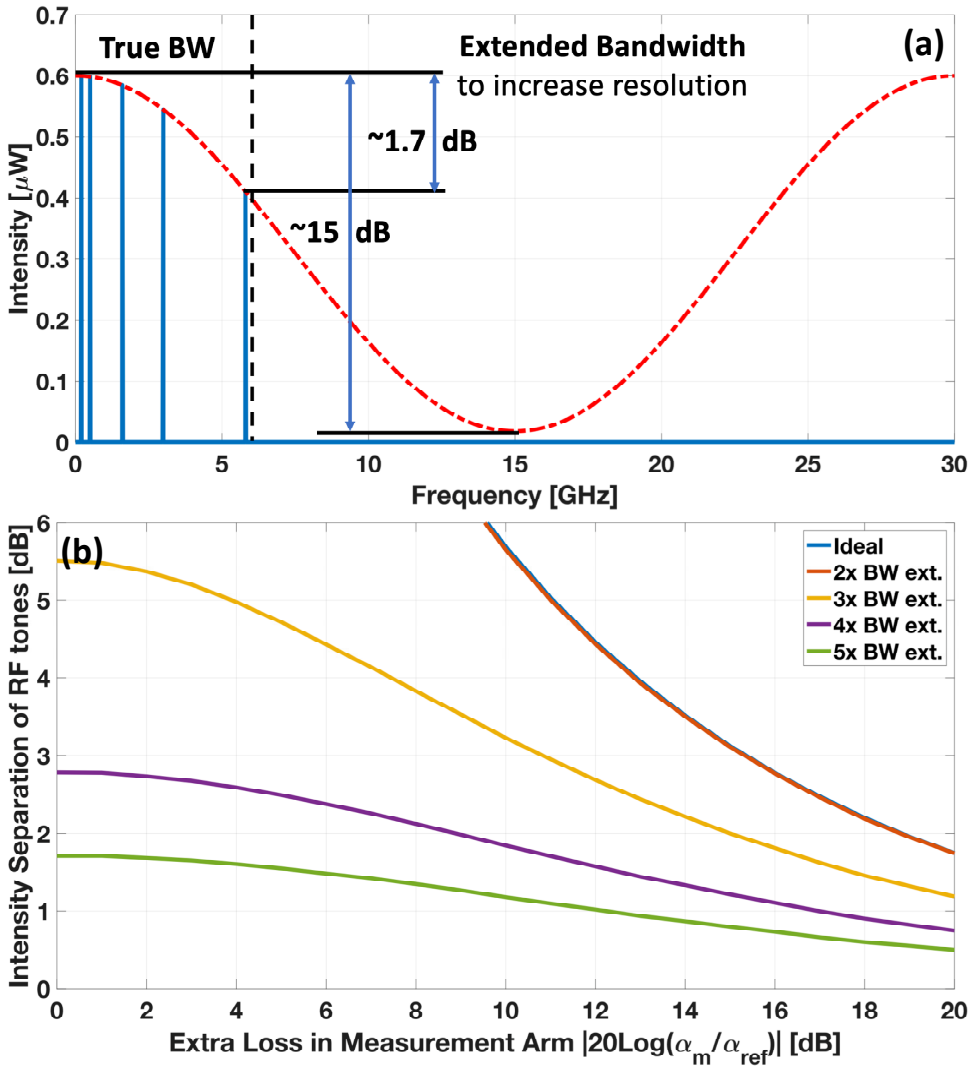

Figure 3.7: (a) Five times extended bandwidth to increase the resolution through sine fitting algorithm (b) Suppression of the variation between RF tone intensities during bandwidth extension up to five times.

3.3 Velocity Measurement

Over the past years, heterodyne or photonic Doppler velocimetry (PDV) is vastly used for detection of the particle velocities after small explosions, or in gas gun experiments, and Lidar systems [64]. The fundamental principle of PDV is triggering the heterodyne detection by combining the reflected beam from a moving target (Doppler-shifted light) with the reference arm as in a Michelson interferometer. The phase shift due to the displacement between the initial and final positions of a moving surface in typical interferometry corresponds to a frequency shift in PDV. A constant speed yields a single shift around the base-band in the frequency domain, but acceleration and deceleration of oscillating target yields various frequency components, which are troublesome to distinguish in the frequency domain [65]. Even though, PDV requires only carrier signal for speed measurements, multi-tone or multi-wavelength systems can improve the accuracy and robustness of the speed measurements. Additionally, multi-tone systems can provide direction information along with the speed to form complete velocity information. We demonstrated the velocity measurement capability of a multi-tone CW lidar system by applying fast (FFT) and short-time Fourier Transform (STFT) [66]. This approach can be used for wind-vector and ocean-surface wave speed profiling.

3.3.1 Principle

The proposed MTCW lidar system can also provide velocity information of the moving targets in a single shot measurement. When a moving target emits an electromagnetic wave at a frequency (f_0), the detected wave at the receiver observes a Doppler frequency shift (Δf) in the amount of

$$\Delta f = \frac{\Delta v}{c} f_0 \tag{3.11}$$

where $\Delta v = -(v_r - v_s)$ is the opposite of the velocity of the receiver relative to the source and c is the speed of the light in the medium. In our system, the source and the receiver are in the same place, therefore the Doppler shift affects the wave incident upon the target as well as the wave reflected back to the receiver. It results in a frequency shift twice that from the same target emitting a wave [67]

$$\Delta f = \frac{2\Delta v}{c} f_0 \tag{3.12}$$

Frequency of the emitted light (f_0) is >200THz in Doppler lidars. Since the radars are operating below a few GHz, light provides >5 orders of magnitude greater carrier frequency (f_0) and Doppler frequency shift (Δf). This property of the light enables detection of slow speeds (< 1mm/s) and high speeds (>200m/s) with high resolution. For example, 1μm light can provide a frequency shift of 2MHz for each 1m/s increase in the relative speed. Therefore, it is possible to detect velocities from 1mm/s to 250m/s with 1mm/s resolution with collecting 500μs data and digitize such data with 1GSa/s ADC. It is important to state that the fastest wind speed, not related to the tornadoes, is recorded as 113m/s (408km/h) by an automatic weather station on Barrow Island, Australia during the passage of Tropical Cyclone Olivia on April 10, 1996 [68]. On the other hand, fastest tornado-related wind speed is recorded as 150m/s (541km/h) near El Reno, Oklahoma, the United States on May 31, 2013 [69]. The system mentioned as an example can measure well above these maximum wind speeds with high resolution.

3.3.2 Experimental Verification

The initial experimental setup demonstrated in Fig. 3.4 is used for high resolution range measurements. To achieve high resolution, we used 6GHz RF tone, therefore we employed a high-speed detector with >12.5GHz bandwidth. Even though such a large bandwidth can

provide high depth resolution ($\frac{c}{2\Delta f} = 12mm$), fiber-coupled input of the detector makes the system prone to vibrations. Since the stability of the system decreases in velocity measurements due to moving targets, the detection mechanism needs to be more robust. Therefore, we replaced the fiber-coupled detector with larger area free-space detectors.

The modified system is used in two velocity measurement experiments: (i) speed profiling of a commercial speaker, (ii) velocity of a moving target on a step-motor.

Speed Profiling of a Commercial Speaker

The measurement setup for free-space PDV is given in Fig. 3.8. A 1550 nm narrow-linewidth laser diode (LD) is pigtailed to a 2 mm aspheric collimator (CL) through a polarization controller (PC), Mach-Zehnder modulator (MZM) and Erbium-doped fiber amplifier (EDFA). The MZM is modulated by a 100 MHz single tone. A beam-splitter operating in the telecom wavelengths is used to separate the reference arm targeting the reference mirror (M1) and the measurement arm incident to the target mirror (M2), which is anchored on the oscillating membrane of a high-power (600 W) speaker (Pyle PLPW6D). The speaker has a maximum longitudinal translation of 4mm and is intensity-modulated via a function generator. The displacement of the membrane is controlled by a 70 Hz sinusoidal input with the 600 mVpp, where the frequency response is at its peak as stated in the datasheet of the speaker. The Doppler-shifted light and the local reference interferes back on the beam-splitter and directed towards InGaAs PIN photodetector (PD) through a focusing lens (L1). Finally, the time-domain measurements are performed by a digital storage oscilloscope (DSO).

The acquired data in the time-domain is further transformed into the frequency domain by applying FFT and STFT. The resultant frequency shifts are related to the velocity according to Eq. 3.12. First, by applying FFT to the large-window time domain it is possible to calculate the maximum resolvable speed of the system to determine the speed boundaries.

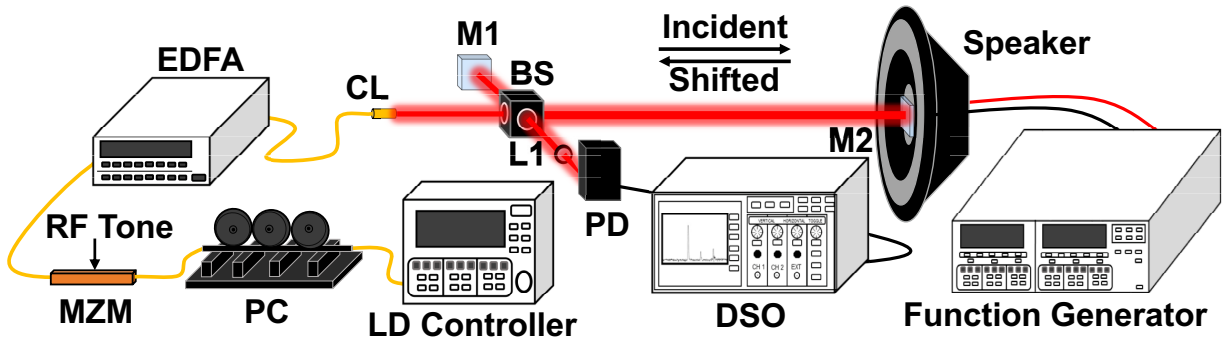

Figure 3.8: Free-space optical PDV measurement setup for speed profiling of a commercial speaker [63].

Then we calculate the intermediary velocity components by narrowing the time window and creating multiple time windows with 1.25 kHz resolution in the frequency domain and applying STFT near the baseband. By associating the zoomed time intervals with their corresponding shifts over a couple of periods, it is possible to create a speed profile of a moving target in the time domain.

The FFT of the large time window data is presented in Fig. 3.9(a) in linear scale and the inset shows the dB scale to realize the transition from signal to the noise floor. The maximum resolvable speed is related to the maximum observable frequency shift, and it is recorded as 11.2 kHz which corresponds to 0.87 cm/s. The maximum displacement of the speaker membrane is 4 mm and its resistance at 70Hz is $\sim 8\Omega$ as stated in its datasheet. When we consider the 100W power handling capability of the speaker, it is clear that the maximum displacement can be achieved at 40 Vpp. In the light of this information, for the given input of 600 mVpp at 70 Hz, the maximum speed of the speaker membrane is estimated as $\sim$0.84 cm/s. Therefore, the measured speed is in a decent agreement with the expected result according to the datasheet.

As is clear in Fig. 3.9(a), there exist many intermediary velocity components as a result of the potential accelerations and decelerations. In order to differentiate the remaining possible velocity components and map the speed profile, we narrowed down the time-scale and applied

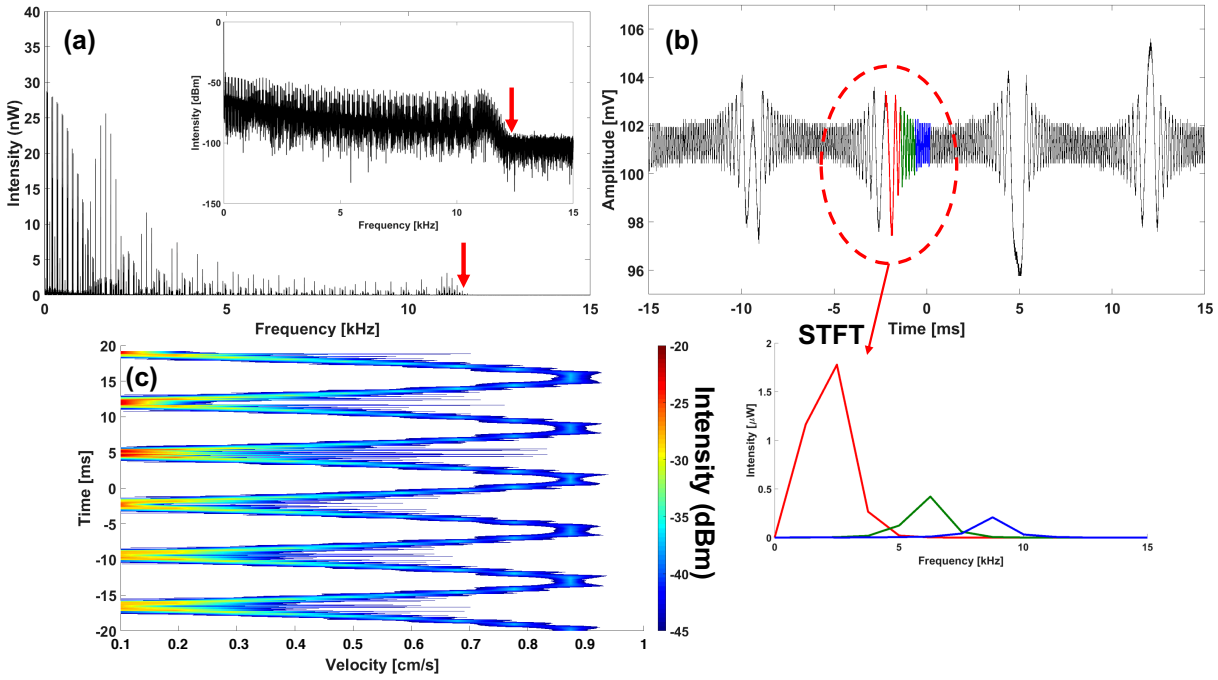

Figure 3.9: (a) FFT of the wide-window time domain in linear scale, arrow shows the maximum Δf. The inset shows the signal to noise floor transition in dB scale. (b) Narrow time domain response, application of STFT shown in red, green and blue. The inset shows the FFT of the corresponding time windows. (c) The speed profile of the speaker membrane oscillation with respect to the intensity [63].

STFT. The narrowed down time-window is shown in Fig. 3.9(b) and the further zoomed time-scales subject to STFT are represented in different colors to achieve the intermediary velocity components. The inset indicates the corresponding frequency domain results of the selected time windows according to their color code. Here, the measured frequency shifts are 2.5 kHz, 6.26 kHz and 8.77 kHz for the selected evenly spaced time-windows (0.8 ms), which maps to 0.195 cm/s, 0.485 cm/s and 0.68 cm/s, respectively.

After post-processing of the data and gathering the resultant velocity components after STFT, it is possible to match the calculated speeds with their time. Then it is possible to construct the speed profile and the speed components of the oscillation of the speaker membrane are given in Fig. 3.9(c) over ∼3 swings of the speaker membrane with respect to their measured intensities. In overall, it is possible to indicate the oscillation period, as well. The oscillation period is calculated as 70.22 Hz while the function generator supplies a sine input at 70 Hz, which shows a good correlation with the measured speed profile.

Speed Measurement of a Target Moving with Constant Speed

The results of the commercial speaker demonstrated that the system is working as expected. However, they do not provide complete proof, since we are not able to observe the membrane movement and map to the measured data. Therefore, we decided to move a target with a fixed velocity and verify the results with a camera. We mounted a target mirror on top of a ∼41.5cm long motorized rail that is controlled with a NEMA-23 stepper motor and DM542T motor driver. By using the Arduino Mega 2560 board, the stepper motor is programmed to make a linear scan with controllable fixed velocity up to ∼10cm/s for velocimetry measurements.

The modified experimental setup is shown in Fig. 3.10. This time, 1550nm laser light is modulated with a few RF tones at 20MHz, 70MHz, 130MHz, and 200MHz that are combined

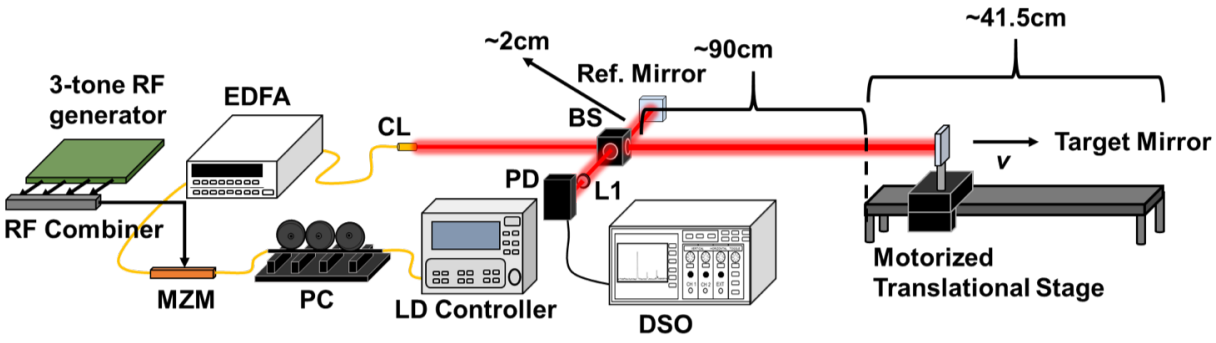

Figure 3.10: Free-space optical PDV measurement setup for speed profiling of a target moved on a motorized translational stage with a constant speed.

with an RF power combiner. In Fig. 3.11(a), the spectrum of the collected time domain data is shown after post-processing. All modulation and distortion tones are observed. In order to observe Doppler frequency shift, we need to zoom in the vicinity of the modulation tones and base-band, since the Doppler frequency shift will be ∼129 kHz for 10cm/s speed. The red arrows in Fig. 3.11(a) point out the zoomed-in regions that are explicitly demonstrated in Fig. 3.11(b)-(d). The Doppler-shift at the base-band is well above the others because it is the combination of the carrier and all modulation tones with their Doppler-shifted counterparts. All of the measurements give similar Doppler shifts around 130.5kHz that maps to 10.11 cm/s speed. This result is also verified with a simultaneous video recording and frame-by-frame motion analysis.

Due to symmetric peaks at 130.5kHz away from the tones, the results shown in Fig. 3.11 do not provide the direction of the motion. However, the modulation scheme can be modified to generate single side-band (SSB) modulated light and one of the peaks will be eliminated. In this way, Doppler shift in positive and negative directions will represent approaching and leaving targets, respectively.

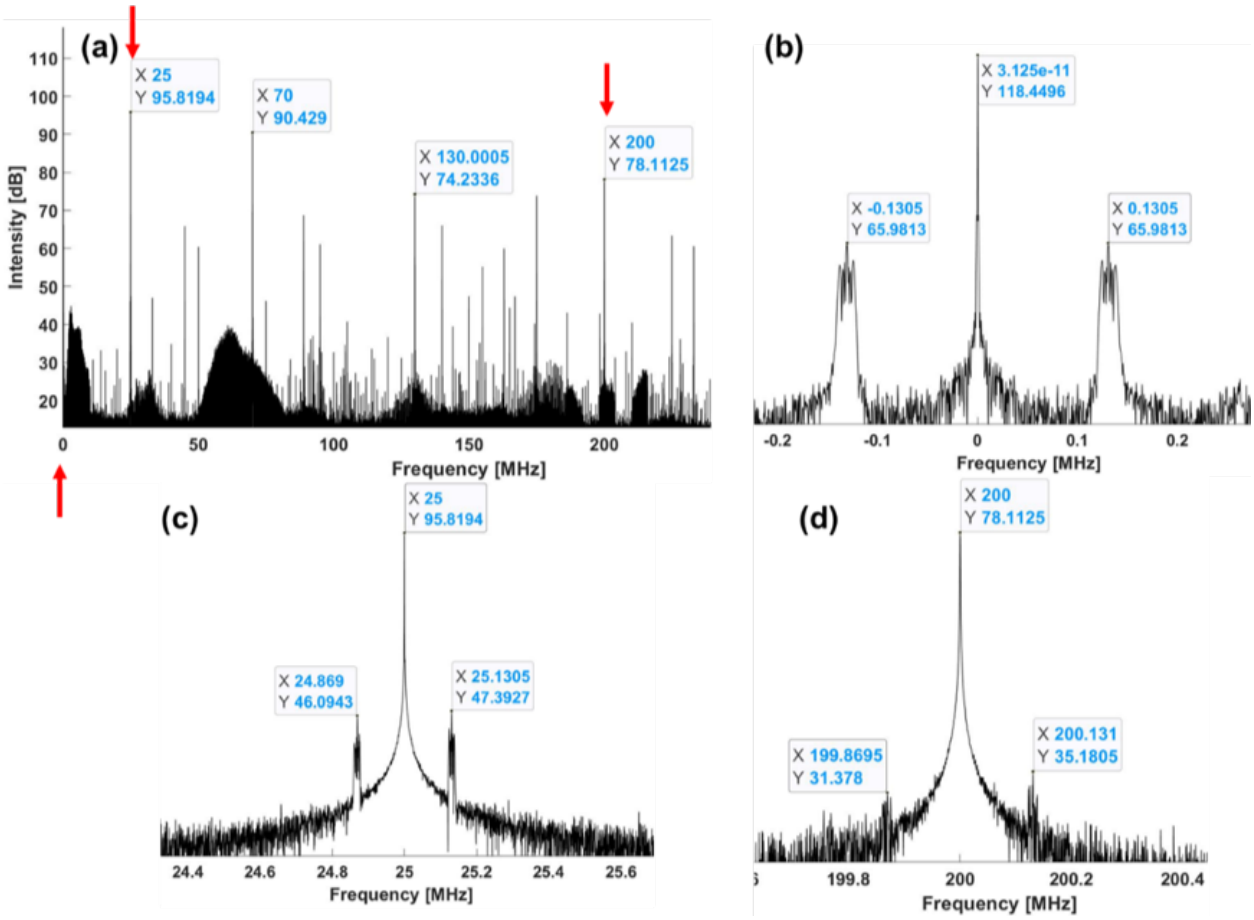

Figure 3.11: Free-space optical PDV measurement results for speed profiling of a target moved on a motorized translational stage. Constant speed of ∼10cm/s creates ∼130kHz Doppler shift.

3.4 Simultaneous Range and Velocity Measurements

We have demonstrated the range and velocity measurements separately in Ch. 3.2 and Ch. 3.3 respectively. In this chapter, we will discuss how the range measurements will change when the target is moving.

3.4.1 Effect of the Doppler Shift on Range Measurements

Doppler frequency shift due to the velocity of the target eliminates the interference between reference and measurement arms, since cross beating terms do not overlap. Therefore, range measurement of the target will depend on only the self-beating terms that generate almost the same frequencies. Still, we expect to have amplitude variation of the tones, but weaker one. The reason can be explained analytically starting from Eq. 3.5 that is rewritten below.

$$E_2 = \frac{A_0}{\sqrt{2}} exp(j\omega_0 t + j\phi_0 - jk_0 z) - \frac{mA_0}{4\sqrt{2}} \sum_{i=1}^{N} exp(j(\omega_0 + 2\pi f_i)t + j(\phi_0 + \phi_i) - jk_0 z) \\ + exp(j(\omega_0 - 2\pi f_i)t + j(\phi_0 - \phi_i) - jk_0 z) \tag{3.13}$$

Later, modulated light (E_2) is transferred to the free space through a collimator and split into two via a beam splitter. Reference signal at the detector is the same as Eq. 3.6.

$$E_{ref} = \frac{A_0}{2\sqrt{2}} \alpha_{ref} exp(j\omega_0 t + j\phi_0 + j\omega_0 \frac{2L_{ref}}{c}) \\ -m\frac{A_0}{4\sqrt{2}} \alpha_{ref} \sum_{i=1}^{N} exp[j(\omega_0 + 2\pi f_i)t + j(\phi_0 + \phi_i) + j(\omega_0 + 2\pi f_i)\frac{2L_{ref}}{c}] \\ + exp[j(\omega_0 - 2\pi f_i)t + j(\phi_0 - \phi_i) + j(\omega_0 - 2\pi f_i)\frac{2L_{ref}}{c}] \tag{3.14}$$

However, measurement signal will have Doppler shift in frequency, therefore phase accumu-

lations during the light propagation to the target and back are slightly different. In the Eq. 3.15, Doppler shift, and both phase shifts are demonstrated clearly. The measurement signal at the detector can be represented as

$$\begin{aligned} E_m = \frac{A_0}{2\sqrt{2}}\alpha_m exp(j(\omega_0+\Delta f_0)t + j\phi_0 + j\omega_0\frac{L_m}{c} + j(\omega_0+\Delta f_0)\frac{L_m}{c}) \\ -m\frac{A_0}{4\sqrt{2}}\alpha_m \sum_{i=1}^{N} exp[j(\omega_0+2\pi f_i+\Delta f_0+\Delta f_i)t + j(\phi_0+\phi_i) \\ +j(\omega_0+2\pi f_i)\frac{L_m}{c} + j(\omega_0+2\pi f_i+\Delta f_0+\Delta f_i)\frac{L_m}{c}] \\ +exp[j(\omega_0-2\pi f_i+\Delta f_0-\Delta f_i)t + j(\phi_0-\phi_i) \\ +j(\omega_0-2\pi f_i)\frac{L_m}{c} + j(\omega_0-2\pi f_i+\Delta f_0-\Delta f_i)\frac{L_m}{c}] \end{aligned} \tag{3.15}$$

where Δf_0 can vary up to $\Delta f_0 = \frac{2\Delta v}{c} f_0 = \pm 300\text{MHz}$, where $|\Delta v| < 150 m/s$ and $f_0 = 300 THz$. On the other hand, Δf_i can vary up to $\pm$5kHz for 5GHz bandwidth. Since $\Delta f_i \ll \Delta f_0$, we can approximate their sums and difference as $\Delta f_0 \pm \Delta f_i \approx \Delta f_0$. Therefore, Eq. 3.15 will be simplified to

$$\begin{aligned} E_m = \frac{A_0}{2\sqrt{2}}\alpha_m exp(j(\omega_0+\Delta f_0)t + j\phi_0 + j\omega_0\frac{2L_m}{c} + j\Delta f_0\frac{L_m}{c}) \\ -m\frac{A_0}{4\sqrt{2}}\alpha_m \sum_{i=1}^{N} exp[j(\omega_0+2\pi f_i+\Delta f_0)t + j(\phi_0+\phi_i) + j(\omega_0+2\pi f_i)\frac{2L_m}{c} + j\Delta f_0\frac{L_m}{c}] \\ +exp[j(\omega_0-2\pi f_i+\Delta f_0)t + j(\phi_0-\phi_i) + j(\omega_0-2\pi f_i)\frac{2L_m}{c} + j\Delta f_0\frac{L_m}{c}] \end{aligned} \tag{3.16}$$

After coherent detection, photodiode current will be

$$I_{PD} = RP_{in} = R(E_{ref}+E_m)(E_{ref}+E_m)^* \tag{3.17}$$

Therefore

$$
\begin{aligned}
I_{PD} = I_{PD,ave} &+ \frac{1}{4}RA_0^2\alpha_{ref}\alpha_m cos\Big(\Delta f_0 t + 2\omega_0\frac{\Delta L}{c} + \Delta f_0\frac{L_m}{c}\Big) \\
-\frac{1}{4}RmA_0^2\sum_{i=1}^{N}\Bigg\{ &\alpha_{ref}^2 cos\Big(2\pi f_i t + \phi_i + 4\pi f_i\frac{L_{ref}}{c}\Big) + \alpha_m^2 cos\Big[(2\pi f_i + \Delta f_i)t + \phi_i + (4\pi f_i + \Delta f_i)\frac{L_m}{c}\Big] \\
&+\frac{1}{2}\alpha_{ref}\alpha_m cos\Big[(2\pi f_i + \Delta f_0)t + \phi_i + 2\omega_0\frac{\Delta L}{c} + 4\pi f_i\frac{L_{ref}}{c} + \Delta f_0\frac{L_m}{c}\Big] \\
&+\frac{1}{2}\alpha_{ref}\alpha_m cos\Big[(2\pi f_i - \Delta f_0)t + \phi_i - 2\omega_0\frac{\Delta L}{c} + 4\pi f_i\frac{L_{ref}}{c} - \Delta f_0\frac{L_m}{c}\Big] \\
&+\frac{1}{2}\alpha_{ref}\alpha_m cos\Big[\big(2\pi f_i + \Delta f_0 + \Delta f_i\big)t + \phi_i + 2\omega_0\frac{\Delta L}{c} + (4\pi f_i + \Delta f_0 + \Delta f_i)\frac{L_m}{c}\Big] \\
&+\frac{1}{2}\alpha_{ref}\alpha_m cos\Big[(2\pi f_i - \Delta f_0 + \Delta f_i)t + \phi_i - 2\omega_0\frac{\Delta L}{c} + (4\pi f_i - \Delta f_0 + \Delta f_i)\frac{L_m}{c}\Big] \\
&-\frac{1}{4}m\alpha_{ref}\alpha_m cos\Big[(\Delta f_0 + \Delta f_i)t + 2(\omega_0 + 2\pi f_i)\frac{\Delta L}{c} + (\Delta f_0 + \Delta f_i)\frac{L_m}{c}\Big] \\
&-\frac{1}{4}m\alpha_{ref}\alpha_m cos\Big[(\Delta f_0 - \Delta f_i)t + 2(\omega_0 - 2\pi f_i)\frac{\Delta L}{c} + (\Delta f_0 - \Delta f_i)\frac{L_m}{c}\Big] \\
&-\frac{1}{4}m\alpha_{ref}^2 cos\Big(4\pi f_i t + 2\phi_i + 8\pi f_i\frac{L_{ref}}{c}\Big) \\
&-\frac{1}{4}m\alpha_{ref}\alpha_m cos\Big[(4\pi f_i - \Delta f_0 + \Delta f_i)t + 2\phi_i - 2\omega_0\frac{\Delta L}{c} + 4\pi f_i\frac{L_{ref} + L_m}{c} - (\Delta f_0 - \Delta f_i)\frac{L_m}{c}\Big] \\
&-\frac{1}{4}m\alpha_{ref}\alpha_m cos\Big[(4\pi f_i + \Delta f_0 + \Delta f_i)t + 2\phi_i + 2\omega_0\frac{\Delta L}{c} + 4\pi f_i\frac{L_{ref} + L_m}{c} + (\Delta f_0 + \Delta f_i)\frac{L_m}{c}\Big] \\
&-\frac{1}{4}m\alpha_m^2 cos\Big[(4\pi f_i + 2\Delta f_i)t + 2\phi_i + (8\pi f_i + 2\Delta f_i)\frac{L_m}{c}\Big]\Bigg\}
\end{aligned}
\tag{3.18}
$$

where $I_{PD,ave} = \frac{1}{8}RA_0^2(1 + N\frac{m^2}{2})(\alpha_{ref}^2 + \alpha_m^2)$ and $\Delta L = L_m - L_{ref}$. Except intermodulation distortion (IMD3) tones, Eq. 3.18 shows complete equation that includes DC part, fundamental tones, harmonic distortions and Doppler shifted components. The following assumptions can be made to simplify this long equation.

i. According to Eq. 3.18, it seems that the interference can only occur when Δf_i is negligibly small. This assumption is valid since detector bandwidth (5GHz) is much smaller than carrier frequency (∼300THz). Additionally, the frequency resolution should be selected accordingly to overlap the fundamental tones created after the interference.

ii. Phase change due to the main optical carrier $\left(2\omega_0\frac{\Delta L}{c}\right)$ is sensitive to micrometer level movements. Such phase change will be averaged out due to the surface roughness of the target and the path length difference caused by focusing. Therefore, it is safe to neglect this phase as we observed from the experiments.

iii. The higher-order distortions (HD2, IMD3, etc.) are not the main focus of this technique, so we can remove them. On the other hand, it is possible to use them similar to the fundamental tones. Even though Eq. 3.18 indicates the feasibility, it requires broader and deeper analysis including higher-order distortion tones.

iv. As clearly seen, the initial phase of the optical carrier (ϕ_0) doesn't have any effect. Additionally, the phases of the RF tones are creating a constant phase shift for the same tones that has no effect on the relative phase shift. Therefore, it is possible to eliminate the RF tone phases ($\phi_i = 0$).

When the above modifications are applied, the equation will be simplified to

$$\begin{aligned}
I_{PD} = I_{PD,ave} + \frac{1}{4}RA_0^2\alpha_{ref}\alpha_m cos\Big(\Delta f_0 t + \Delta f_0\frac{L_m}{c}\Big) \\
-\frac{1}{4}RmA_0^2\sum_{i=1}^{N}\Bigg\{\alpha_{ref}^2 cos\Big(2\pi f_i t + 4\pi f_i\frac{L_{ref}}{c}\Big) + \alpha_m^2 cos\Big(2\pi f_i t + 4\pi f_i\frac{L_m}{c}\Big) \\
+\frac{1}{2}\alpha_{ref}\alpha_m cos\Big[(2\pi f_i + \Delta f_0)t + 4\pi f_i\frac{L_{ref}}{c} + \Delta f_0\frac{L_m}{c}\Big] \\
+\frac{1}{2}\alpha_{ref}\alpha_m cos\Big[(2\pi f_i - \Delta f_0)t + 4\pi f_i\frac{L_{ref}}{c} - \Delta f_0\frac{L_m}{c}\Big] \\
+\frac{1}{2}\alpha_{ref}\alpha_m cos\Big[\big(2\pi f_i + \Delta f_0\big)t + (4\pi f_i + \Delta f_0)\frac{L_m}{c}\Big] \\
+\frac{1}{2}\alpha_{ref}\alpha_m cos\Big[(2\pi f_i - \Delta f_0)t + (4\pi f_i - \Delta f_0)\frac{L_m}{c}\Big] \\
-\frac{1}{4}m\alpha_{ref}\alpha_m cos\Big[\Delta f_0 t + 2\pi f_i\frac{2\Delta L}{c} + \Delta f_0\frac{L_m}{c}\Big] \\
-\frac{1}{4}m\alpha_{ref}\alpha_m cos\Big[\Delta f_0 t - 2\pi f_i\frac{2\Delta L}{c} + \Delta f_0\frac{L_m}{c}\Big]\Bigg\}
\end{aligned} \tag{3.19}$$

When the Doppler frequency shifts are entirely eliminated ($\Delta f_0 = 0$), Eq. 3.19 will convert

to

$$I_{PD} = I^{'}_{PD,ave} - \frac{1}{4} RmA_0^2 \sum_{i=1}^{N} \Bigg\{ \Big(\alpha_{ref}^2 + \alpha_{ref}\alpha_m\Big) cos\Big(2\pi f_i t + 4\pi f_i \frac{L_{ref}}{c}\Big) + \Big(\alpha_{ref}\alpha_m + \alpha_m^2\Big) cos\Big(2\pi f_i t + 4\pi f_i \frac{L_m}{c}\Big) \Bigg\} \tag{3.20}$$

that is exactly equal to Eq. 3.8. When we compare Eq. 3.19 with Eq. 3.20, it is obvious that less beating terms are overlapped in the presence of Doppler shift which creates smaller amplitude variation. However, the proposed sinusoidal fitting method will still work.

3.5 Conclusion

In this chapter, we demonstrated the multi-tone modulated continuous wave Lidar system. The technique has the capability of providing high precision range and velocity information of static and moving targets. In addition, we performed proof of concept experiments along with the theoretical and numerical analysis of range and velocity measurements in static and dynamic environments. Further applications of the proposed method for scattering targets can be implemented by engineering the source power and receiver sensitivity.

Chapter 4

Photonic Assisted Continuous-Time Analog to Digital Converter

4.1 Introduction

According to the well-known Moore's Law, integrated circuit (IC) technology is rapidly developed in the last 50 years with doubling the performance every 18 months in terms of size and speed [70]. However, analog to digital converters (ADCs) couldn't achieve the same pace and became the bottleneck in terms of sampling rates. Therefore, interleaving methods are introduced to increase the ADC performance.

In the electrical domain, time interleaving is employed to use multiple ADCs in parallel to process data series at a faster rate than the operating sample rate of each individual ADC as shown in Fig. 4.1. As expected, such an increase in the sampling rate comes with a power and area penalty due to parallelization. Additionally, the noise performance of the system will degrade due to gain, offset, and timing mismatches between the interleaved channels. Therefore, interleaving will not benefit for the Walden figure of merit (FOM) in

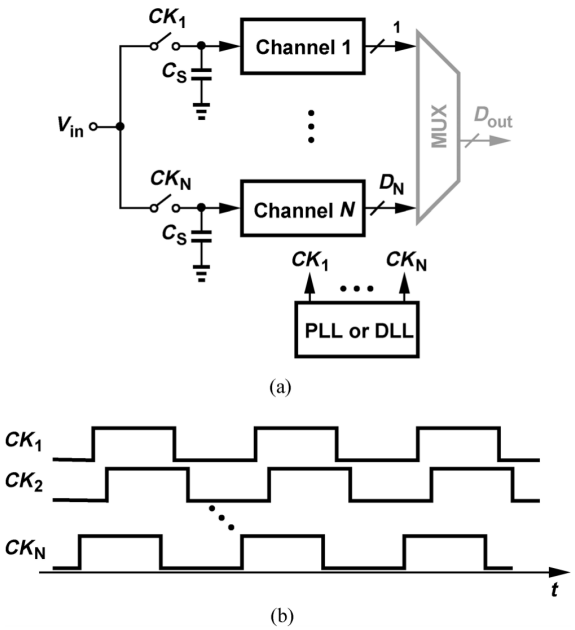

Figure 4.1: (a) Time interleaved ADC environment and (b) its clock phases [72].

comparison to the single ADC used at the back-end as seen in the below equation, since $ENOB_{IL} \leq ENOB_{ADC}$.

$$\frac{FOM_{IL}}{FOM_{ADC}} = \frac{\frac{N \times P_{diss}}{N \times f_s \times 2^{ENOB_{IL}}}}{\frac{P_{diss}}{f_s \times 2^{ENOB_{ADC}}}} = 2^{(ENOB_{ADC} - ENOB_{IL})} \geq 1 \tag{4.1}$$

where N is the number of interleaved channels, P_{diss} is the power dissipation, f_s is the sampling rate and ENOB is the effective number of bits. Since, the FOM indicates the power consumption for the same performance, lower the value the better it is [71].

However, regardless of the above calculation, interleaving still improves the FOM. Since the interleaving is employed when the conversion speed of a single channel approaches the limits of the technology, the power and speed trade-off becomes nonlinear. Therefore, even if the desired speed increase is achievable, it will demand a disproportionately higher power. Moreover, it is not easy to scale the increased timing constraints with power [72].

The electronic time-interleaved ADCs operating at high speeds are mainly limited by the timing jitter of the electronic clocks. Therefore, photonic time and wavelength interleaving

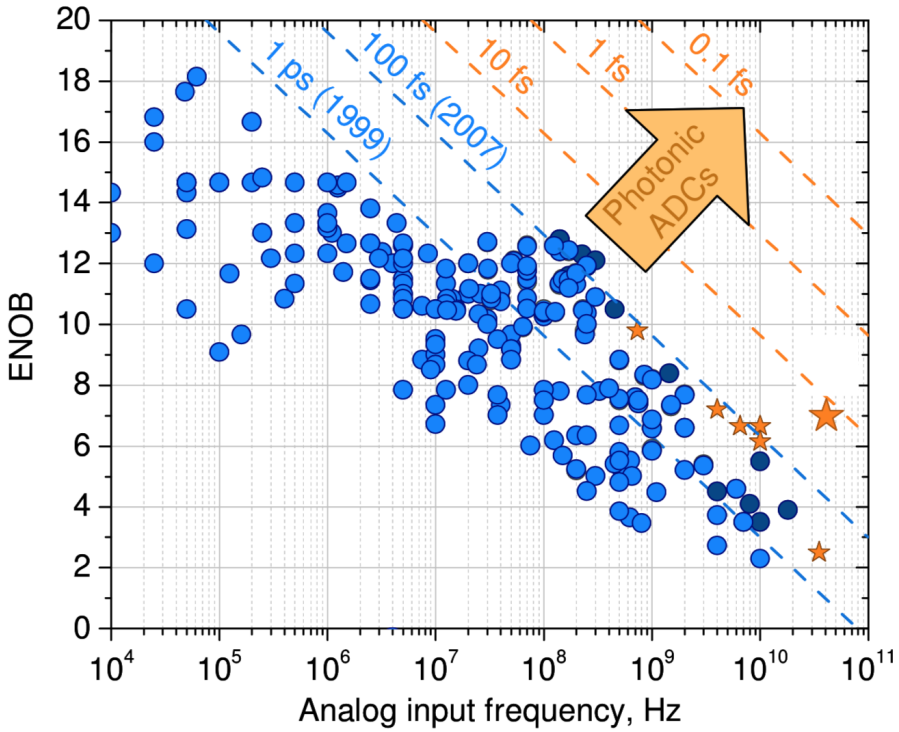

Figure 4.2: Walden plot showing ENOB of existing ADCs as a function of the analog input frequency. Each point represents an ADC: electronic (circles) and photonic (stars). Dashed lines show the maximum jitter to achieve such performance. As indicated by the arrow, photonic ADCs, operating with very low timing jitter, are envisioned to bring ADC performance to new levels [73].

techniques are introduced to exploit several orders of magnitude lower timing jitter of mode-locked lasers. Figure 4.2 demonstrates ENOB of the existing ADCs with circles (electronic ADCs) and stars (photonic ADCs). Also, the performance improvement related to low timing jitter of photonic ADCs is indicated with an arrow [73]. Additionally, it is important to note that as low as 13 attosecond jitter is previously achieved in optical domain [12].

In the recent years, several research groups are designing ADC-less detection systems, such as demodulators and sequence detectors [74, 75, 76]. Such approaches achieve low power consumption and eliminate the design challenges of interleaved ADCs [77]. However, they are focused mainly on communications where the signal characteristics (e.g. bit-rate, modulation format) are pre-defined. ADC-less detection is valuable to remove the ADC speed bottleneck and reveal the full potential of integrated circuit technology advancement stated in Moore's

Law. On the other hand, high-speed ADCs are still in demand for a wide range of applications from medicine to defense industry to capture random fast events [78, 79, 80].

4.1.1 Photonic ADCs

Analog to digital conversion has two main stages: sampling and quantization. Photonic ADCs employ optical components or methods to replace at least one of these stages. In the sampling stage, an analog input signal is sampled at precise points to generate a set of analog values that will be converted to digital values in the quantization stage. In his review paper, Valley classified photonic ADCs according to which stage is implemented optically as shown in Fig. 4.3 [11].

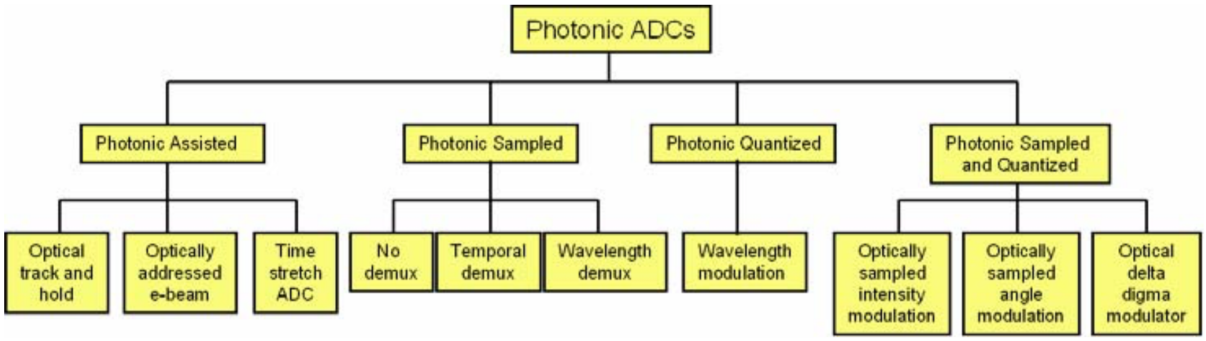

Figure 4.3: Four major classes of photonic ADCs [11].

In this work, we propose a photonic sampled ADC system that employs time and wavelength interleaving of CW lasers to increase the effective sampling rate of electronic ADCs and wavelength demultiplexing to down-convert signals to detect each color with single low-speed ADC. In the proposed approach, several (N) continuous-wave lasers that have equally spaced wavelengths are combined with a dense wavelength division multiplexer (DWDM) and pulsated with a single MZM that is driven with a short pulse to form N-color synchronized sampler. Synchronized N-color sampler pulses are uniformly distributed in the time domain with employing wavelength-to-time mapping property of the linear dispersive medium to

generate multi-color time-interleaved high-speed sampler. In another modulator, the analog input signal is optically sampled by this high repetition rate ($N \times f_s$) pulse train. After the photonic sampling of the RF signal, different colors are separated with a DWDM demultiplexer to be quantized with a slow speed (f_s) electronic ADC (Fig. 4.4). Consequently, the proposed system is an optical front-end for electronic ADCs to increase their speed by employing time and wavelength interleaving, sampling and wavelength demultiplexing in optical domain and quantization in the electronic domain.

In this chapter, the proposed photonic sampler system is investigated theoretically and verified with numerical simulations. Also, proof of principle experiments have been performed to show the system performance. Additionally, experimental limitations are explained and potential performance improvements with using state-of-the-art components are discussed.

4.2 Principle of the System

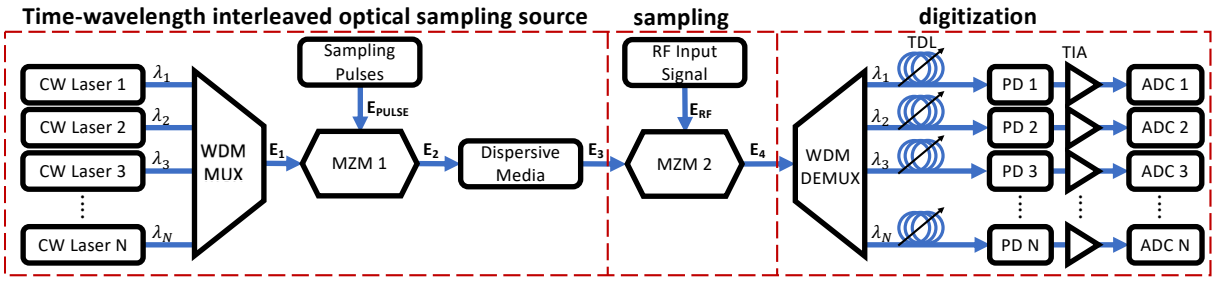

Figure 4.4: Simplified block diagram of the proposed photonic sampled interleaved ADC.

As seen in Fig. 4.4, the proposed system fundamentally consists of high repetition rate optical pulse source, optical sampling of the analog input signal, wavelength demultiplexing, and electronic quantization of each channel. Here, the repetition rate of the optical sampling source is increased with pulse modulating several CW lasers simultaneously and then temporally separating each wavelength by employing dispersion property of optical media such as optical fiber or employing accurate delays to each channel separately. To facilitate

the low timing jitter of the optical sources, the analog input signal is sampled in the optical domain with the help of an intensity modulator. Later, the sampled signal is split into sub-channels via wavelength demultiplexing. The optical field in each channel is detected with a photodiode and then quantized with electronic ADCs after amplification. Wavelength demultiplexing works as downconverter and eliminates the need for high-speed electronics.

More detailed schematic of the proposed photonic sampled electronically quantized ADC system is illustrated in Fig. 4.5. In the proposed system, only MZMs have a polarization-dependent response. Therefore, the polarization state of the light at the modulator input should match the internal polarizer of the modulator. Therefore, each CW laser is followed by a polarization controller that matches the polarization of the individual lasers to the modulator along with correcting any polarization rotation occurred due to the single-mode fibers connecting the components. Fixing the output polarization of the lasers and replacing all fibers with polarization maintaining counterparts can eliminate the need for polarization controllers and simplify the system. Later, all the wavelengths are combined with a wide-band combiner or a WDM multiplexer which works better with further suppressing the side modes of the laser and eliminating the possible problems due to the overlap of sideband with the other channels.

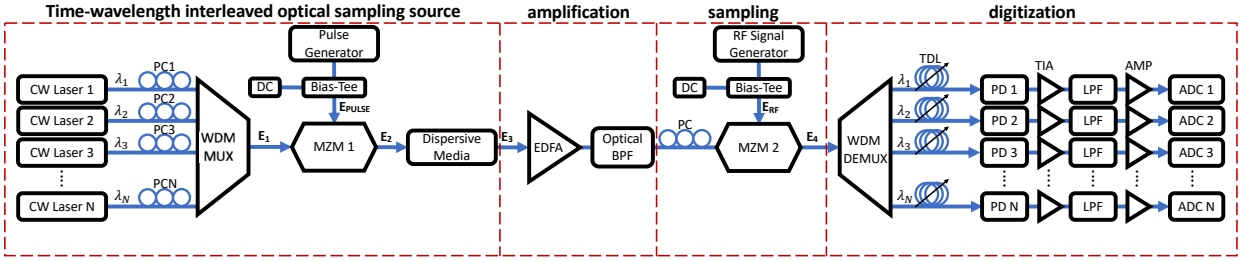

Figure 4.5: Detailed block diagram of the proposed photonic sampled interleaved ADC.

The combined wavelengths are pulsated with an MZM that is biased at the minimum transmission point and driven with an amplified pulse train to achieve a full swing of transmission. The pulse generator can be an RF component or optoelectronic device based on a mode-locked laser (MLL). MLL based pulse generator is demonstrated in Fig. 4.6 together with

simple pulse interleaving method to increase the repetition rate. Even though MLL creates narrow pulses (e.g. 100fs), the pulse width of the optical sampler is limited by the bandwidth of the optoelectronic and electronic components including photodetector, modulator, and RF amplifiers.

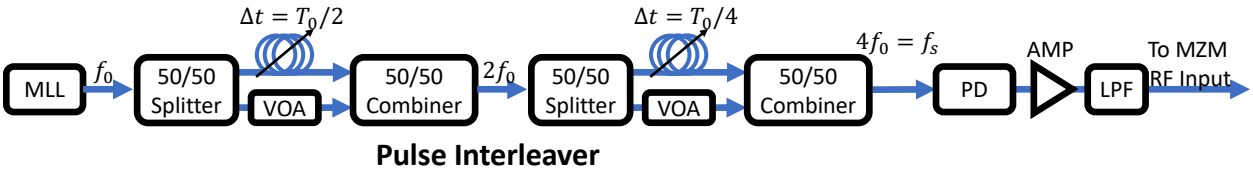

Figure 4.6: MLL based time interleaved pulse generator.

After the first modulator, all wavelengths are pulsated to be employed as an optical sampler, but they overlap in the time domain. Then, dispersive medium introduces delay where each wavelength is separated $\Delta t = \frac{1}{N \times f_s}$ with respect to the closest wavelength to achieve high repetition rate sampler ($N \times f_s$). Such delays can be applied to each wavelength individually via true delay lines that can provide the most accurate and flexible delays. However, extra multiplexer and demultiplexer pair is required as seen in Fig. 4.7. The other technique is to facilitate the dispersion property of optical components such as fibers, chirped fiber Bragg gratings (CFBG), and prisms. Since our system is based on fibers, the best options are fibers or CFBGs. In this project, we employed SMF based dispersion compensation modules (DCM) that have a limited range of linear dispersion due to non-zero β_3 term. In the proof of concept stage of this project, we employed tunable CW lasers, therefore the wavelength of each channel (λ_i) can be slightly tuned to correct nonlinear dispersion and achieve accurate temporal delays. Temperature controlled wavelength tuning is also possible for fixed wavelength DFB lasers in a short tuning range with lower quality. After the linear dispersive medium, high repetition rate optical sampling pulses are generated.

Such pulses are amplified with an EDFA to increase the peak power that is followed by an optical bandpass filter to eliminate ASE noise due to the wide-band (∼80nm) gain spectrum of EDFA. Bandwidth ($\Delta\lambda_{BPF}$) of the optical bandpass filter to suppress ASE noise depends

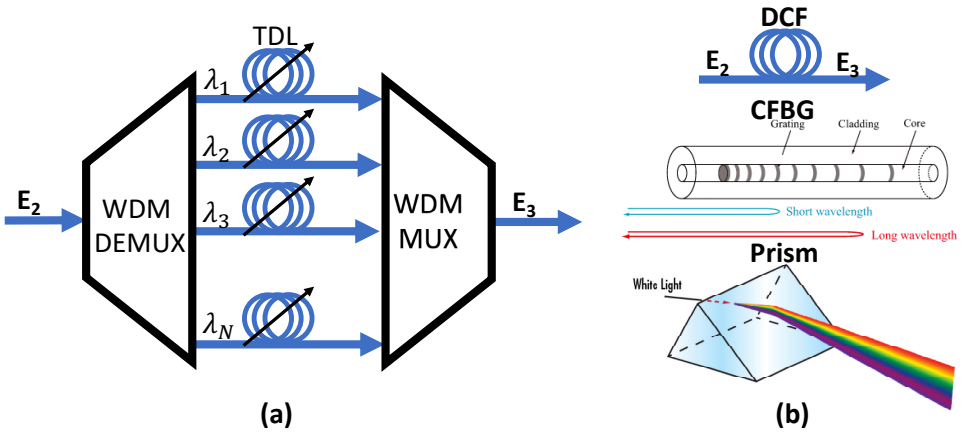

Figure 4.7: Techniques to create high repetition rate sampler. (a) TDL based time interleaver (b) various dispersive media: fiber, CFBG [81], prism [82].

on the amount of parallelization (N) and channel separation ($\Delta\lambda_{ch}$) where $\Delta\lambda_{BPF} \geq (N-1)\Delta\lambda_{ch}$.

After the amplification, an RF signal is encoded on the sampling pulses via MZM that is biased at quadrature point. Since each wavelength is temporally separated, they sample the RF signal at different positions. Quadrature biasing inherently cancels even-order harmonic distortion tones [83]. However, modulator linearization is still required to suppress odd-order harmonics. This photonic sampling step is crucial to assess the performance of the proposed ADC. Since the ENOB of the proposed ADC is calculated based on a single RF tone, the purity of the RF signal is crucial. Therefore, the RF tone generated by a synthesizer is first amplified and then filtered with a narrow BPF to minimize noise generated by the amplifier and to suppress the harmonics. On the other hand, quadrature biasing is also important to cancel even harmonics, therefore automated bias controller as shown in Fig. 4.8 [84] is suggested to ensure accurate biasing. Moreover, the bandwidth of this modulator determines the analog input bandwidth of the proposed ADC [85].

After the optical sampling of the RF signal, each wavelength is separated via a WDM demultiplexer that may add unequal delays to the wavelengths. Since the wavelengths are already separated in time for sampling, the total net delay should be calculated for each wavelength.

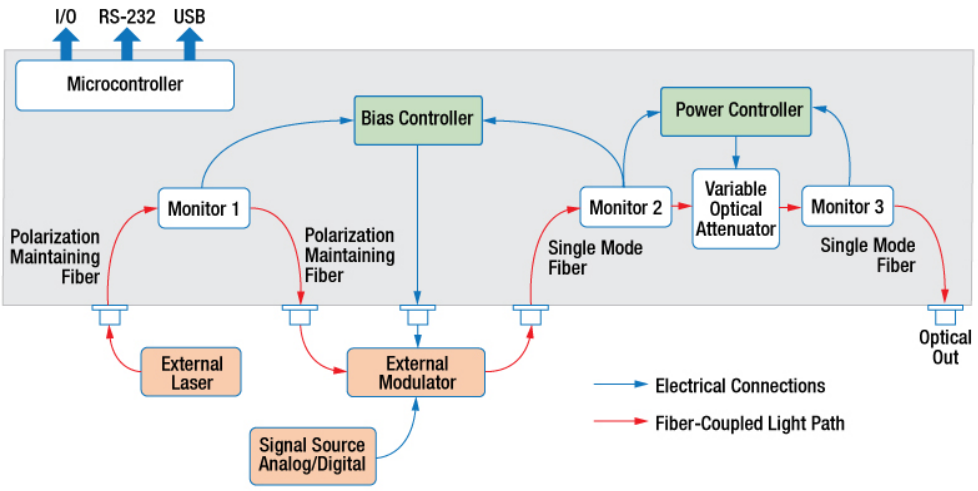

Figure 4.8: Block diagram of the automated modulator bias controller [84].

By employing tunable delay lines, optical sampling pulses from different channels can be synchronized in the time domain with <10fs accuracy and repeatability. In this way, all slow ADCs will be triggered at the same time with the same clock input, hence no need for delaying each clock.

After temporal alignment of channels, each optical wavelength is converted to the electrical domain with a photodiode. Generated photodiode current is pre-amplified with a trans-impedance amplifier (TIA) and then low pass filtered with a bandwidth of $B_{LPF} \geq f_s/2$ to limit input noise bandwidth and amplified again to utilize the full dynamic range of the electronic ADCs. ADCs quantized the optically sampled signal and generated digital signals are transferred to a computer for post-processing. The post-processing includes (i) modulator linearization, (ii) interleaving the data from N channels, (iii) Fourier transformation, (iv) spectral analysis to identify distortion tones and interleaving spurs, and (v) performance parameter calculation including SNR, SFDR, THD, SINAD, and ENOB.

4.2.1 Analytical Modeling

The complex optical field at the output of the WDM multiplexer can be modeled as

$$E_1 = \sum_{n=1}^{N} A_n exp(j2\pi f_n t + j\phi_n) \tag{4.2}$$

where A_n, f_n, and ϕ_n are amplitude, frequency, and phase of the n^{th} CW laser output respectively. Later, this optical carrier combination is intensity modulated by a Gaussian pulse train that can be represented as

$$E_{PULSE} = A_{PULSE} \sum_{m=-\infty}^{\infty} exp\Big[-\frac{1}{2}\Big(\frac{t - mT_s}{T_0}\Big)^2 \Big] \tag{4.3}$$

where A_{PULSE} is the amplitude of the pulse, T_s is the fundamental sampling period, and T_0 is the half width at 1/e intensity point and related to full width at half maximum of the pulse as $T_{FWHM} = 1.665T_0$.

The field transfer function of the balanced driven Mach Zehnder modulator (MZM) under push-pull configuration is $cos(0.5\pi\frac{v_m}{V_\pi})$ where $v_m = \pm V_\pi + E_{PULSE}$ when biasing at minimum transmission point. Therefore, after trigonometric conversions, the transfer function of MZM can be rewritten as

$$cos\Big(\pm \frac{\pi}{2} + \frac{\pi}{2V_\pi} E_{PULSE}\Big) = \mp sin\Big(\frac{\pi}{2V_\pi} E_{PULSE}\Big) \tag{4.4}$$

Since this is pulse modulation, it will cover all the points from minimum to maximum transmission, therefore $A_{PULSE} = V_\pi$ and the field at the output of the first modulator will be

$$E_2 = E_1 sin\Big(\frac{\pi}{2V_\pi} E_{PULSE}\Big) \tag{4.5}$$

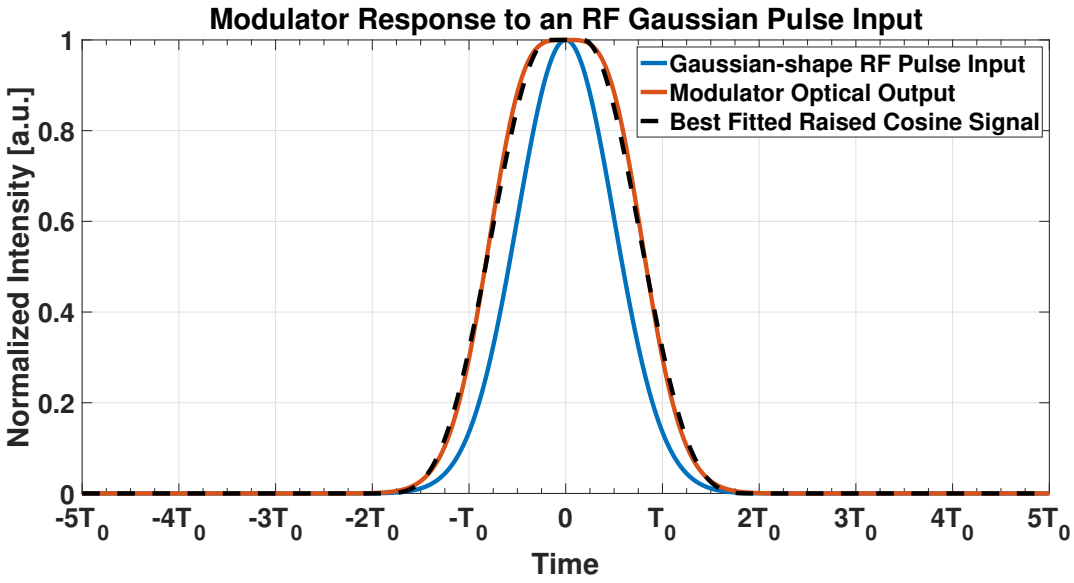

Figure 4.9: Effect of 100% modulation depth on Gaussian Signal. CW optical input is pulsated with Gaussian Pulse from Pulse Generator that is amplified to achieve 100% modulation depth. Modulator output becomes raised-cosine like pulse with β=0.834 and T=0.1165T_0 due to nonlinear transfer function of the MZM.

and when Eq. 4.2 and Eq. 4.3 are inserted in Eq. 4.5, E_2 will be

$$E_2 = \sum_{n=1}^{N} \left\{ A_n exp(j2\pi f_n t + j\phi_n) sin\left(\frac{\pi}{2} \sum_{m=-\infty}^{\infty} exp\left[-\frac{1}{2}\left(\frac{t - mT_s}{T_0} \right)^2 \right] \right) \right\} \tag{4.6}$$

As shown in Fig. 4.9, modulator non-linearity converts Gaussian pulses to raised cosine like pulses. However, we can represent these pulses with Dirac delta or another envelope function for mathematical simplicity, since all of them are short pulses and will be used to sample an RF signal. The investigation of broader pulses is left for numerical analysis. Therefore, E_2 will convert to

$$E_2 = \sum_{n=1}^{N} \sum_{m=-\infty}^{\infty} A_n exp\Big(j2\pi f_n t + j\phi_n\Big) \delta\Big(t - mT_s\Big) = \sum_{n=1}^{N} \sum_{m=-\infty}^{\infty} A_n \delta\Big(t - mT_s\Big) \tag{4.7}$$

During propagation in dispersive media, each wavelength will be delayed $\Delta t_n = (n-1)T_s/N$ with respect to the first channel. Therefore, the output of the high repetition rate sampling

source will be

$$E_3 = \sum_{n=1}^{N} \sum_{m=-\infty}^{\infty} A_n \delta\Big(t - mT_s - \frac{n-1}{N} T_s\Big) \tag{4.8}$$

After amplification, these sampling pulses are used to sample an RF signal with the help of another intensity modulator that is biased at the quadrature point. Since we are not interested in the phase information of the optical field, it is better to use intensity and power transfer function of MZM. Therefore, I_3 will be

$$I_3 = \sum_{n=1}^{N} \sum_{m=-\infty}^{\infty} P_n \delta\Big(t - mT_s - \frac{n-1}{N} T_s\Big) \tag{4.9}$$

and power transfer function of the modulator biased at the quadrature point ($V_b = -\frac{V_\pi}{2}$) will be

$$T_{MZM2}(t) = cos^2\Big(\frac{\pi}{4} + \frac{\pi}{2V_\pi}(V_b + E_{RF})\Big) = \frac{1}{2}\Bigg[1 + cos\Big(-\frac{\pi}{2} + \frac{\pi}{V_\pi} E_{RF}\Big)\Bigg] = \frac{1}{2}\Bigg[1 + sin\Big(\frac{\pi}{V_\pi} E_{RF}\Big)\Bigg] \tag{4.10}$$

where E_{RF} can be any analog input signal, but it is set to single tone RF signal for performance analysis of photonic ADC. Therefore, E_{RF} will be

$$E_{RF} = A_{in} cos(2\pi f_{in} t + \phi_{in}) \tag{4.11}$$

where A_{in}, f_{in}, and ϕ_{in} are the amplitude, frequency, and phase of input RF tone, respectively. The modulator transfer function will be linear, if low modulation depth ($m = \pi \frac{A_{in}}{V_\pi} \ll 1$) is assumed. Using small angle approximations, the output intensity can be expressed as

$$I_4 = T_{MZM2}(t) G_{opt} I_3 \approx \frac{G_{opt} I_3}{2} + \frac{G_{opt} I_3}{2} \frac{\pi}{2V_\pi} E_{RF} \tag{4.12}$$

where G_{opt} is small signal power gain of the EDFA. After inserting I_3, the most general representation of I_4 and its small signal approximation will be

$$\begin{aligned} I_4 &= G_{opt}\sum_{n=1}^{N}\sum_{m=-\infty}^{\infty} P_n T_{MZM2}\Big(t - mT_s - \frac{n-1}{N}T_s\Big) \\ &\approx G_{opt}\sum_{n=1}^{N}\sum_{m=-\infty}^{\infty} \frac{P_n}{2} + \frac{P_n A_{in}\pi}{4V_\pi} cos\Big[2\pi f_{in}\Big(t - mT_s - \frac{n-1}{N}T_s\Big) + \phi_{in}\Big] \end{aligned} \tag{4.13}$$

that will be converted to electronic domain after wavelength demultiplexing and time delaying to overlap the channels and simplify clock distribution. Therefore, the photodiode current of each channel can be represented as

$$\begin{aligned} i_n(t) &= R_n G_{opt} P_n \sum_{m=-\infty}^{\infty} T_{MZM2}\Big(t - mT_s - \frac{n-1}{N}T_s\Big) \\ &\approx \frac{1}{2}R_n G_{opt} P_n \left\{1 + \frac{\pi}{2V_\pi}A_{in}\sum_{m=-\infty}^{\infty} cos\Big[2\pi f_{in}\Big(t - mT_s - \frac{n-1}{N}T_s\Big) + \phi_{in}\Big]\right\} \end{aligned} \tag{4.14}$$

where R_n is the responsivity of the photodiode in channel n. After considering the effect of electronic components such as amplifiers and filters, the voltages at the input of the electronic ADCs to be quantized will be

$$\begin{aligned} v_n(t) &= R_n G_{opt} P_n \sum_{m=-\infty}^{\infty} T_{MZM2}\Big(t - mT_s - \frac{n-1}{N}T_s\Big) * g_n h(t) * \delta(t - \delta t_n) \\ &\approx \frac{\pi}{4V_\pi} g_n R_n G_{opt} P_n A_{in} \sum_{m=-\infty}^{\infty} cos\Big[2\pi f_{in}\Big(t - mT_s - \frac{n-1}{N}T_s\Big) + \phi_{in}\Big] * h(t) * \delta(t - \delta t_n) \end{aligned} \tag{4.15}$$

where g_n represents the link gain of analog components in channel n, h(t) represents the normalized impulse response of analog components, and δt_n represents the timing mismatches. Here, DC component of $v_n(t)$ can be discarded due to balanced detection or DC block of the RF amplifiers. In the ideal case where $\delta t_n \approx 0$, $h(t) \approx 1$ for the Nyquist bandwidth of the

ADC, and gains and powers ($G_{opt}g_nR_nP_n = V_{eq}$) are equal, the interleaved result will be

$$\begin{aligned} v(t) &= V_{eq}\sum_{n=1}^{N}\sum_{m=-\infty}^{\infty} T_{MZM2}\Big(t - mT_s - \frac{n-1}{N}T_s\Big) * \delta(t) \\ &\approx V_{eq}\frac{\pi}{4V_\pi}A_{in}\sum_{n=1}^{N}\sum_{m=-\infty}^{\infty} cos\Big[2\pi f_{in}\Big(t - mT_s - \frac{n-1}{N}T_s\Big) + \phi_{in}\Big] * \delta(t) \end{aligned} \tag{4.16}$$

after Nyquist sampling in electronic ADCs. As it is clearly seen in the linear case, the result is the single tone RF signal sampled at a high repetition rate ($N \times f_s$). For the general case, modulator can be linearized by applying the inverse of T_{MZM2} to ADC sampled data before interleaving.

4.2.2 Numerical Verification

Since it is not easy to represent all of the system anomalies including noises, nonlinearities, and timing mismatches mathematically, we modeled the full system of the proposed photonic ADC in the computer environment using OptSim for optoelectronic parts and MATLAB for post-processing.

In Fig. 4.10, the evolution of the optical signal that creates high repetition rate sampler is demonstrated. Initially, a combination of all 4 laser channels (from 193.2THz to 193.8THz with 200GHz channel spacing) is shown in Fig. 4.10(a). Since the lasers are CW, their output powers are represented as equal DC values. Later, pulse-modulated output with 1GHz repetition rate is demonstrated in Fig. 4.10(b). Due to wavelength-dependent refractive index change of $LiNbO_3$, each wavelength is observing slightly different delay (∼3.86fs/nm at room temperature) while propagating through the modulator with 4cm-long crystal. Since the delay is so small, we see all pulses in sync after the modulator. Also, inset shows the effect of the WDM demultiplexer that will be used to separate channels after the sampling. The band-pass filter behavior of the demultiplexer creates slight variations in peak position that

will cause peak power fluctuation. This is a deterministic error and such delays will occur for every filter in the system. Their cumulative effect can be corrected before quantization with electronic ADCs. Later, high repetition rate sampler with 4GHz repetition rate is demonstrated in Fig. 4.10(c) where a linear dispersive medium is employed to achieve desired delays for each wavelength. The zoomed version is given as an inset to demonstrate the pulse shape. Due to the dispersion effect of the fiber, individual pulses are squeezed from ∼50ps to ∼22ps while different wavelengths are separating from each other. This process also increased pulse peak power from 7.6mW to 13.5mW, since energy is squeezed to a narrower region. To properly represent individual wavelengths, the results are recorded after demultiplexing the wavelengths at each step and combined later in MATLAB.

In the proposed system, we are executing the sampling part of the analog to digital conversion in the optical domain due to achievable ultra-low timing jitters. Therefore, the quality of the photonic sampler is important. The sampler should have low jitter and narrow pulses, therefore, the best sampler is provided by mode-locked lasers. They can create a high repetition rate (>100GHz) ultra-short (< 100fs) pulses with ultra-low timing jitter (<10fs). Another approach is the pulse modulated CW lasers. In this method, CW lasers are either modulated with a single tone RF frequency (e.g. 10GHz) and later squeezed in a dispersive medium to create pulses, or directly modulated with a pulse source. These methods can provide ps-level pulse width with <250fs jitter [86, 87]. The pulse width is limited by the modulator bandwidth. In pulse-modulated systems, initial lasers are jitter-free due to continuous-wave operation. However, pulse modulation can add some timing jitter to the system due to wavelength and temperature-dependent refractive index change of the $LiNbO_3$ crystal. Modulator effect on the jitter is <8.7fs/nm/°C. Since thermo-electric coolers can achieve high precision temperature control (stability <0.01°C), wavelength stability of CW lasers will be < ±0.01nm. Therefore, modulator induced jitter will be in attosecond level. It shows that the system is mainly limited by the jitter of the pulse generator that can be based on optical or RF systems depending on the application and design metrics.

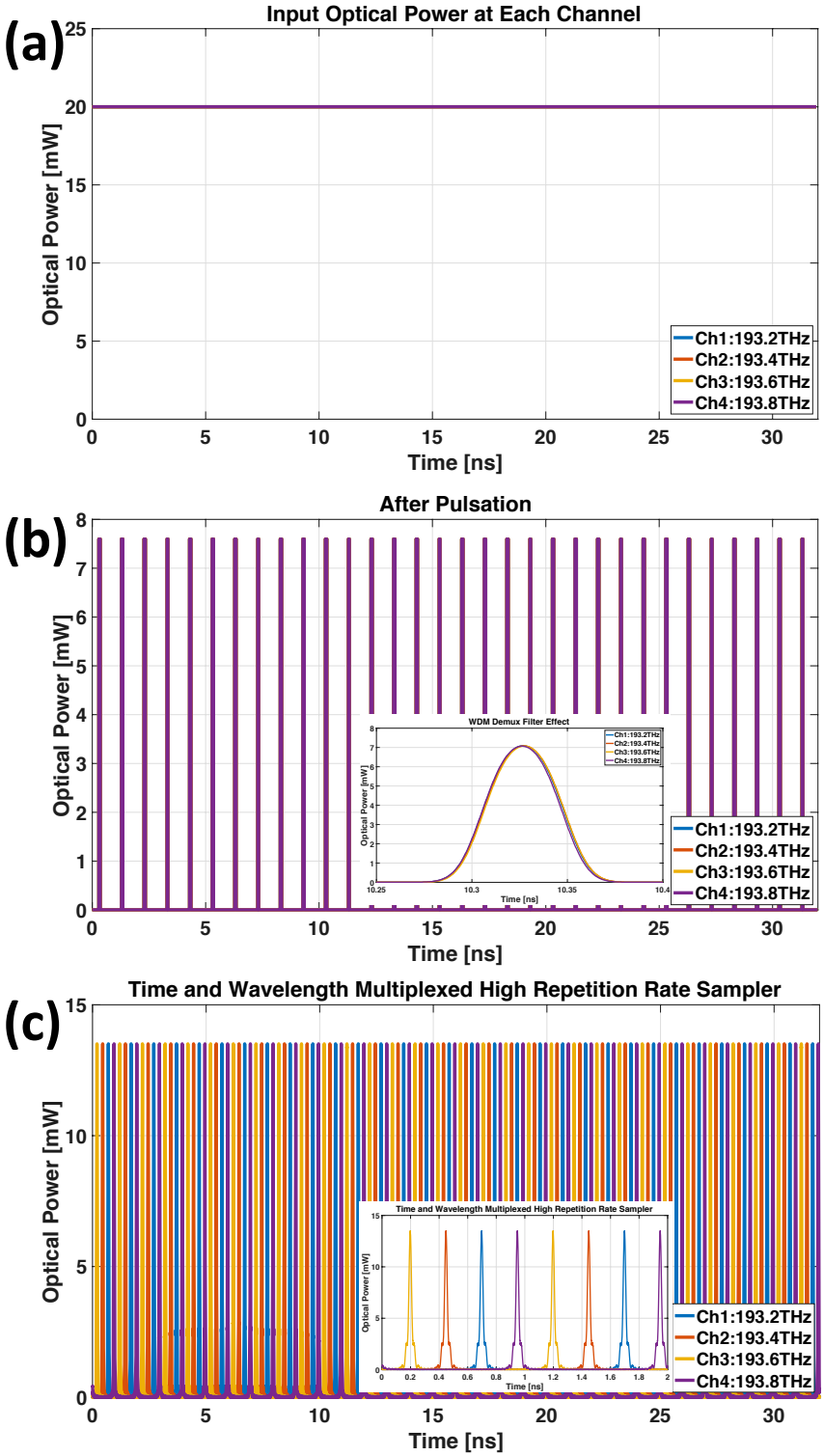

Figure 4.10: Evolution of the optical signal to create high repetition rate sampler via time and wavelength interleaving. (a) Initial CW lasers after multiplexing (b) Pulse modulated sampler (f_s) that includes all 4 temporally overlapped wavelengths (c) after linear dispersion: 4 wavelengths are delayed and create high repetition rate sampler ($4f_s$) signal.

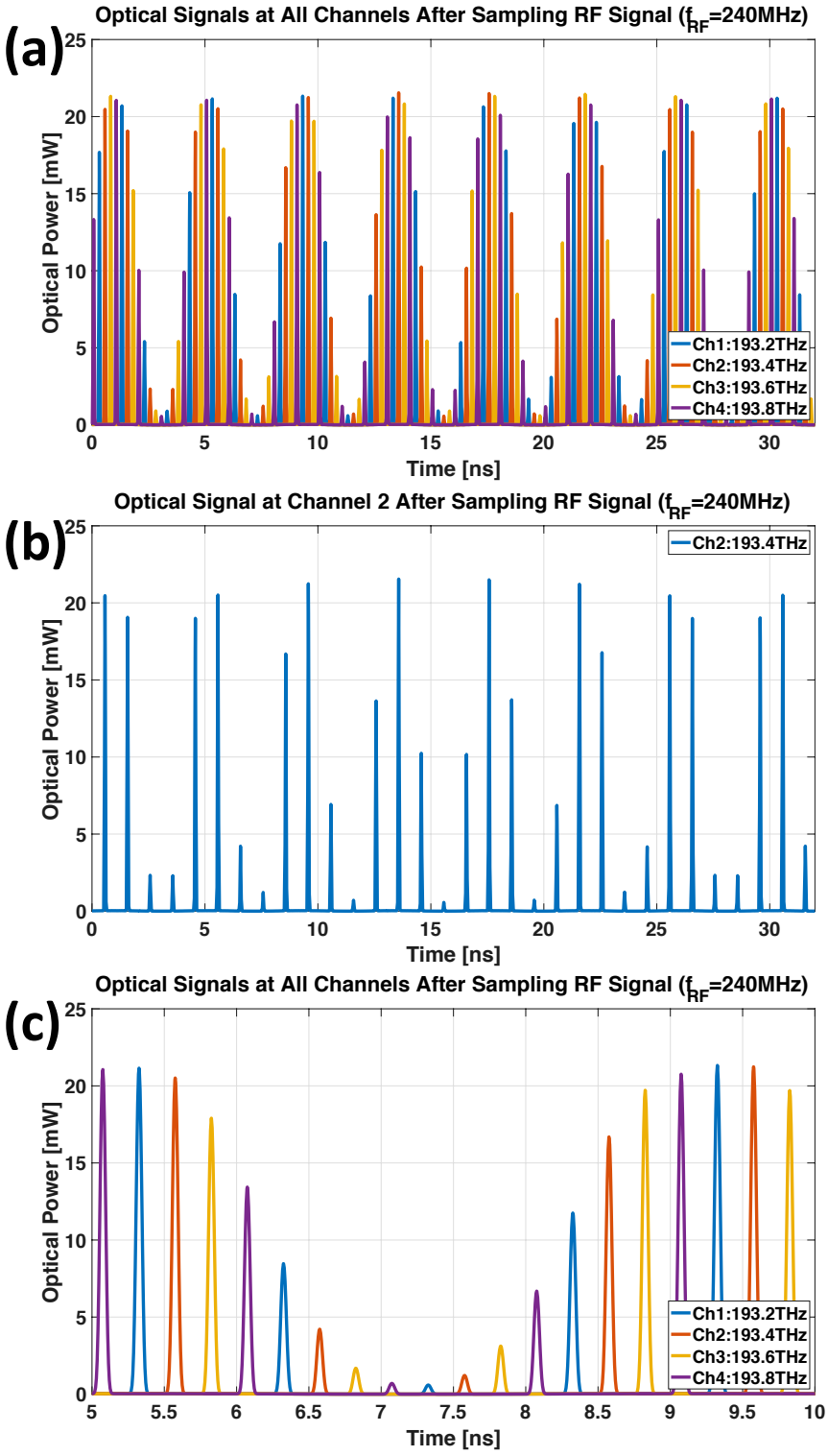

Figure 4.11: Optical signal after sampling 240MHz RF signal. (a) All four channels are shown together. RF signal is clearly visible from the peaks. (b) Single channel (Channel 2: 193.4THz) is shown separately. (c) Zoomed in version of (a) to demonstrate individual ∼45ps wide sampling pulses.

The generated sampler pulses travel through another MZM where the analog input signal is sampled. In this numerical study, to demonstrate the sampling at each channel and after combining all channels, a tone that is below the Nyquist bandwidth of single ADC is selected. Since electronic ADCs are sampling at 1GSa/s, Nyquist bandwidth is 500MHz. Therefore, 240MHz is selected for demonstration purposes. Individual channels are separated with a DWDM demultiplexer and results are combined in MATLAB. Fig. 4.11(b) shows the optically sampled signal at Channel 2 just before photodetection. Also, the combination of all channels is demonstrated in Fig. 4.11(a). While the RF tone is not clearly visible in single-channel due to a low number of samples ($\sim$4.17 points per period), the combined result with 4$\times$ more samples ($\sim$16.67 pts/period) can represent the signal much better. The interleaved system increases the sampling rate to 4GSa/s, hence Nyquist bandwidth to 2GHz. Therefore, the frequencies from 500MHz to 2GHz can be sampled with the optically interleaved system with satisfying the Nyquist criteria. Figure 4.11(c) is showing the zoomed-in version of Fig. 4.11(a) to demonstrate the pulse width and pulse separation of each channel. Previously shown raised cosine like pulse shape is converted to the Gaussian due to the Gaussian filtering with 20GHz bandwidth while separating different wavelengths via demultiplexer. Due to 20GHz bandwidth of the Gaussian filter, the pulses are $\sim$45ps wide (full-width at half maximum) and $\sim$108ps wide if we consider full width at 1% of the maximum. Since pulses are 250ps apart due to 4 times interleaving, it seems that it is possible to achieve 8 times interleaving. Even further interleaving can be possible with increasing the bandwidth of the initial modulator and demux filter to achieve narrower pulses.

In electronic ADCs, the analog input bandwidth is generally limited by the sample and hold circuit. Here, the analog input bandwidth of the proposed system is determined by the bandwidth of the second modulator that is used to encode the RF signal on optical sampling pulses. Therefore, it is possible to achieve up to 110GHz analog bandwidth with the custom design of the modulator and other components such as DWDM Mux/Demux. On the other hand, it is more suitable to facilitate 40GHz analog input bandwidth due to widely available

commercial off-the-shelf (COTS) components. Both of the MZMs used in this numerical study have 8GHz bandwidth due to the components used in the experimental study.

After sampling the given RF signal and demultiplexing to individual channels, optical signal at each channel is detected by an InGaAs PIN photodiode with 1.2GHz bandwidth and amplified with TIA and RF amplifiers to achieve full input voltage swing (1V amplitude) of the electronic ADC. Due to $\sim$16$\times$ bandwidth decrease, the individual pulses are broadened. Their tails are slightly overlapped, however, the tail is not continued all the way to the peak point as shown in Fig. 4.12(b), therefore it does not create any problem.

Here, the sampling rate of electronic ADC should be the same as the repetition rate of the optical sampler that is 1GHz. Therefore, 1GSa/s electronic ADC with 8-bit resolution, 165fs RMS timing jitter, 2Vpp input voltage swing, and 750MHz analog input bandwidth is employed for the numerical study. Since we didn't employ balanced detection in the experimental work, it is not used in the numerical study too. Therefore, negative voltages cannot be used that causes a 1-bit drop in resolution.

Figure 4.12(a) demonstrates the combination of all channels before quantization with several ADCs. Also, channel 2 is shown separately in Fig. 4.12(b). Also, zoomed in version is shown in Fig. 4.12(c) to indicate 1.2GHz detector response.

The signals are shown in Fig. 4.12 are sampled with 4 ADCs with 1GSa/s at the peak points. The sampled data is combined in MATLAB with applying necessary delays and plotted together in the time domain. While plotting, bits are converted back to voltages with using ideal digital to analog converter (DAC) logic. Individual channel (Ch2) and combined results are shown in Fig. 4.13 for 32ns similar to previous figures. However, total collected data is 8192ns to properly calculate the performance parameters from the frequency domain analysis.

Spectral-domain representation of the collected data is given in Fig. 4.15 after applying

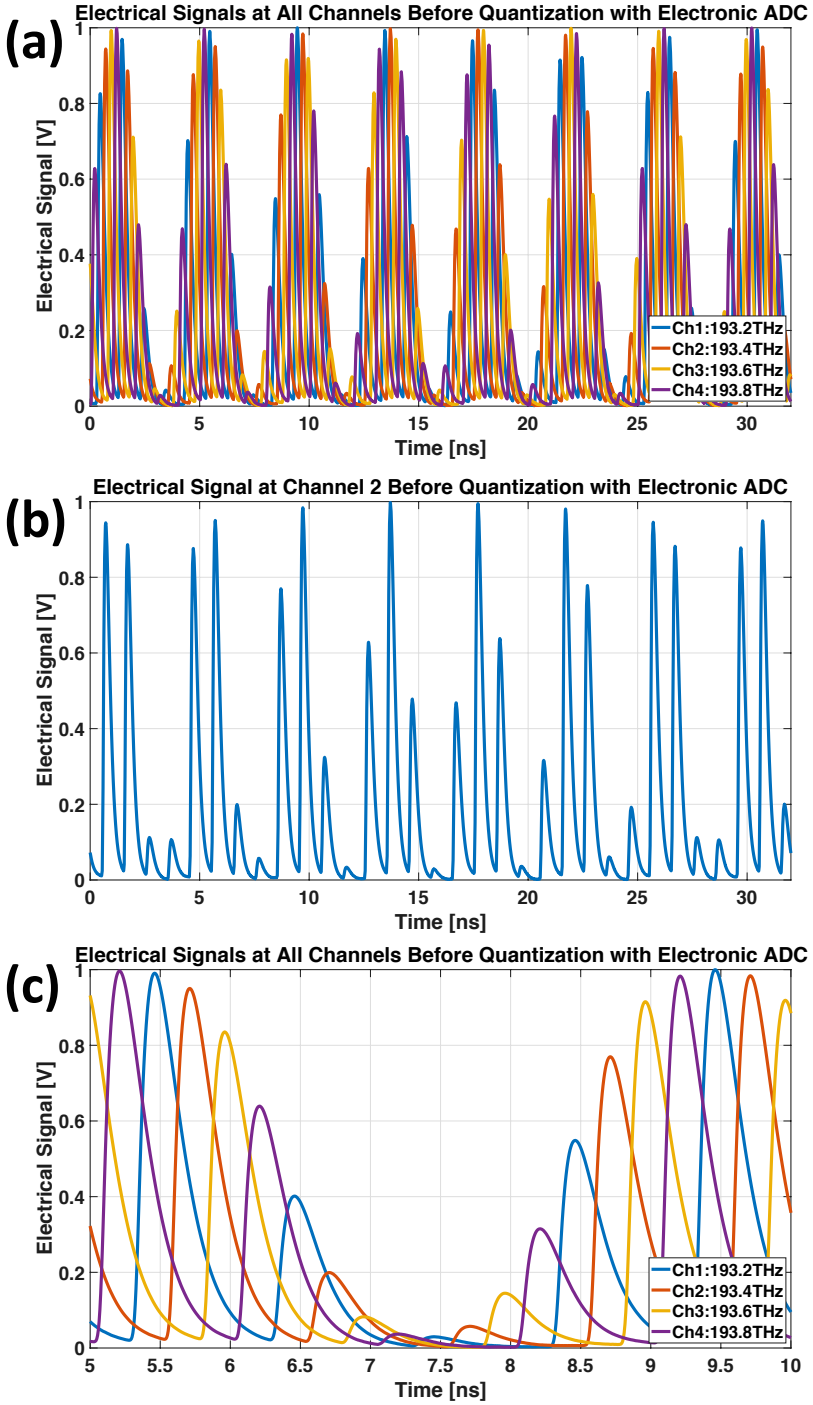

Figure 4.12: Electrical signals before quantization with electronic ADCs. The optical signals at each channel are detected with 1.2GHz photodetectors, amplified with TIA and/or RF amplifiers to achieve full input voltage swing of the electronic ADCs, and filtered to suppress amplifier noise generated outside the desired bandwidth. (a) All four channels are shown together. (b) Single channel (Channel 2: 193.4THz) is shown separately. (c) Zoomed in version of (a) to demonstrate individual pulses after bandwidth limitation of photodetector and RF amplifiers.

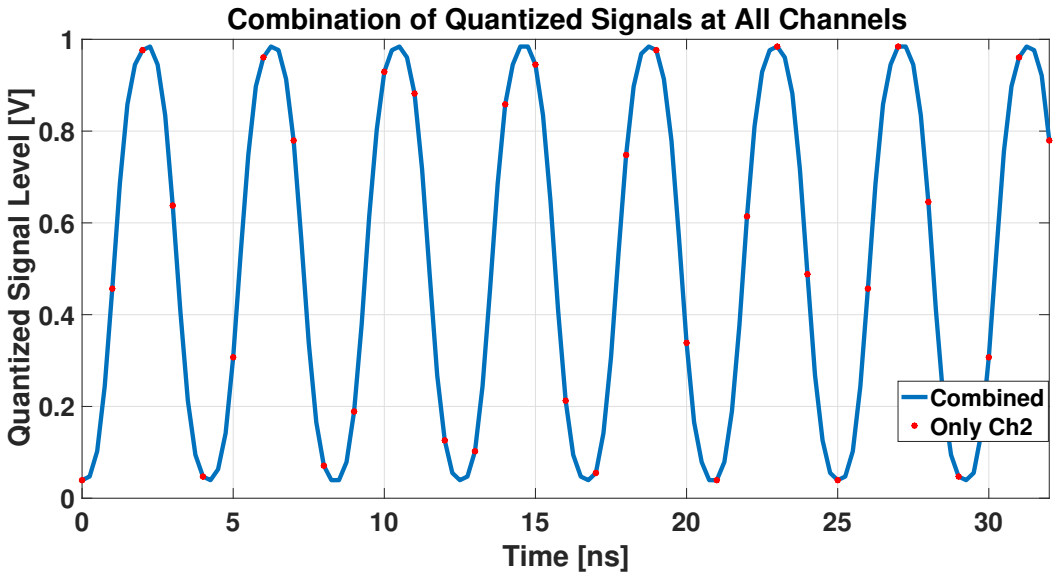

Figure 4.13: Combination of quantized signals at all channels. Also channel 2 data points are shown as red dots on the plot for reference. Data is taken as bits and converted to voltages via ideal DAC.

only Blackman windowing to the raw data. Here, the frequency resolution is ∼122kHz due to 8192ns long time window. Single-channel is represented up to 500MHz due to Nyquist bandwidth limit that is extended four times for the interleaved system. Due to quadrature biasing of the modulator, even-order harmonics are suppressed, however, odd orders are still present and HD3 at 720MHz is the strongest. In single-channel, HD3 is aliased to 280MHz as seen in 4.15(a). Also, interleaving spurs are observed in the combined signal due to gain and offset mismatches between individual ADC channels. The performance metrics calculated from the Fourier spectra of the individual ADC channels and their interleaved result are tabulated in Table 4.1.

The modulator is a nonlinear device with a sinusoidal transfer function as mentioned in the analytical modeling (Ch. 4.2.1). It can be used in linear mode with keeping modulation depth low and biasing at quadrature point. However, low modulation limits facilitating the full energy of the sampling pulses and require extra amplification later on. Therefore, in this numerical study, the modulation depth is kept at 80%. In practical applications <10% modulation depth is assumed linear and 40-60% modulation depth can be enough in terms

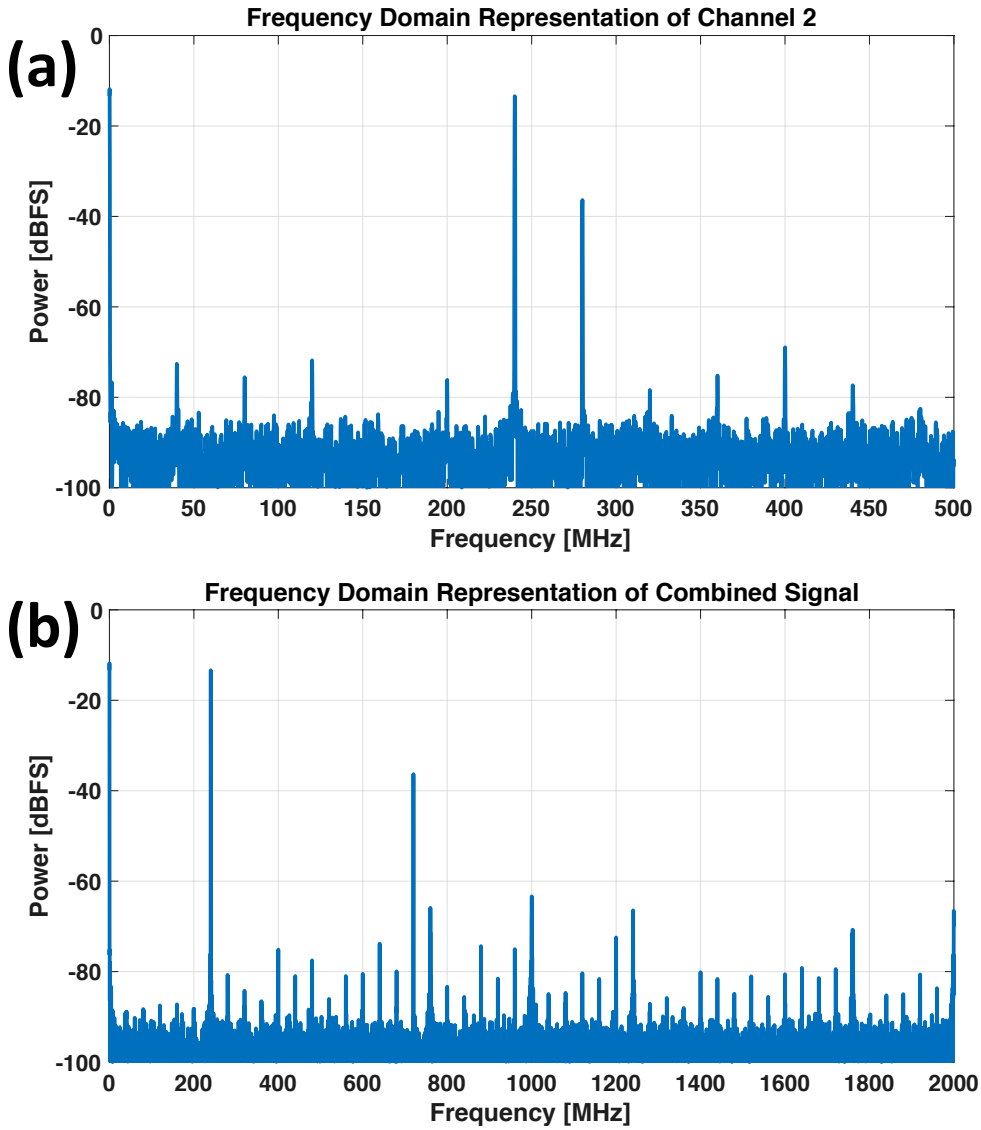

Figure 4.14: Frequency domain representation of single channel and interleaved system. Only blackman windowing function is applied to the raw data. Frequency resolution for both cases is ∼122kHz due to 8192ns time window. Spectral representation of (a) Channel 2, (b) interleaved data.

of power requirements. However, 80% modulation depth is employed to test the ability of a basic modulator linearization technique. This technique is applied to final sampled and quantized data and simply inverse the transfer function of the modulator assuming all other devices are linear in the system. The power transfer function of the modulator is

$$T_{MZM}(t) = \frac{1}{2}\left[1 + sin\Big(\frac{\pi}{V_\pi}V_{in}(t)\Big)\right] \tag{4.17}$$

Since optical power is converted to electrical current at the photodiode that is later converted to voltage, optical power at the modulator output is linearly proportional to ADC voltage $V_{ADC}(t) \approx C_G \times sin\Big(V_{in}(t)\Big) + C_O$ where C_G and C_O are representing gain and offset changes during propagation from modulator output to electronic ADC. In order to linearize modulator, we need to use this proportionality to extract $V_{in}(t)$, therefore

$$V_{in}(t) = sin^{-1}\left(\frac{V_{ADC}(t) - C_O}{C_G}\right) = sin^{-1}\left(\frac{V_{ADC}(t)}{C_1} + C_2\right) \tag{4.18}$$

where C_1=C_G and C_2=-C_O/C_G [85]. The parameters are optimized to achieve best possible ENOB for the linearized signal. The formulas for the performance metrics are [88]

$$SNR[dB] = 10 \times log_{10}\Big(\frac{P_{signal}}{P_{noise}}\Big) \tag{4.19a}$$

$$SFDR[dB] = 10 \times log_{10}\Big(\frac{P_{signal}}{max(P_{spur})}\Big) \tag{4.19b}$$

$$SINAD[dB] = 10 \times log_{10}\Big(\frac{P_{signal}}{P_{noise} + P_{harmonics}}\Big) = 10 \times log_{10}\Big(\frac{P_{signal}}{P_{total} - P_{DC} - P_{signal}}\Big) \tag{4.19c}$$

$$ENOB = \frac{SINAD[dB] - 1.76}{6.02} \tag{4.19d}$$

As shown in Table 4.1, after post-processing, the achieved ENOB is 5.2bits and which can go all the way up to 5.76bits if all the distortion tones can be eliminated with further processing.

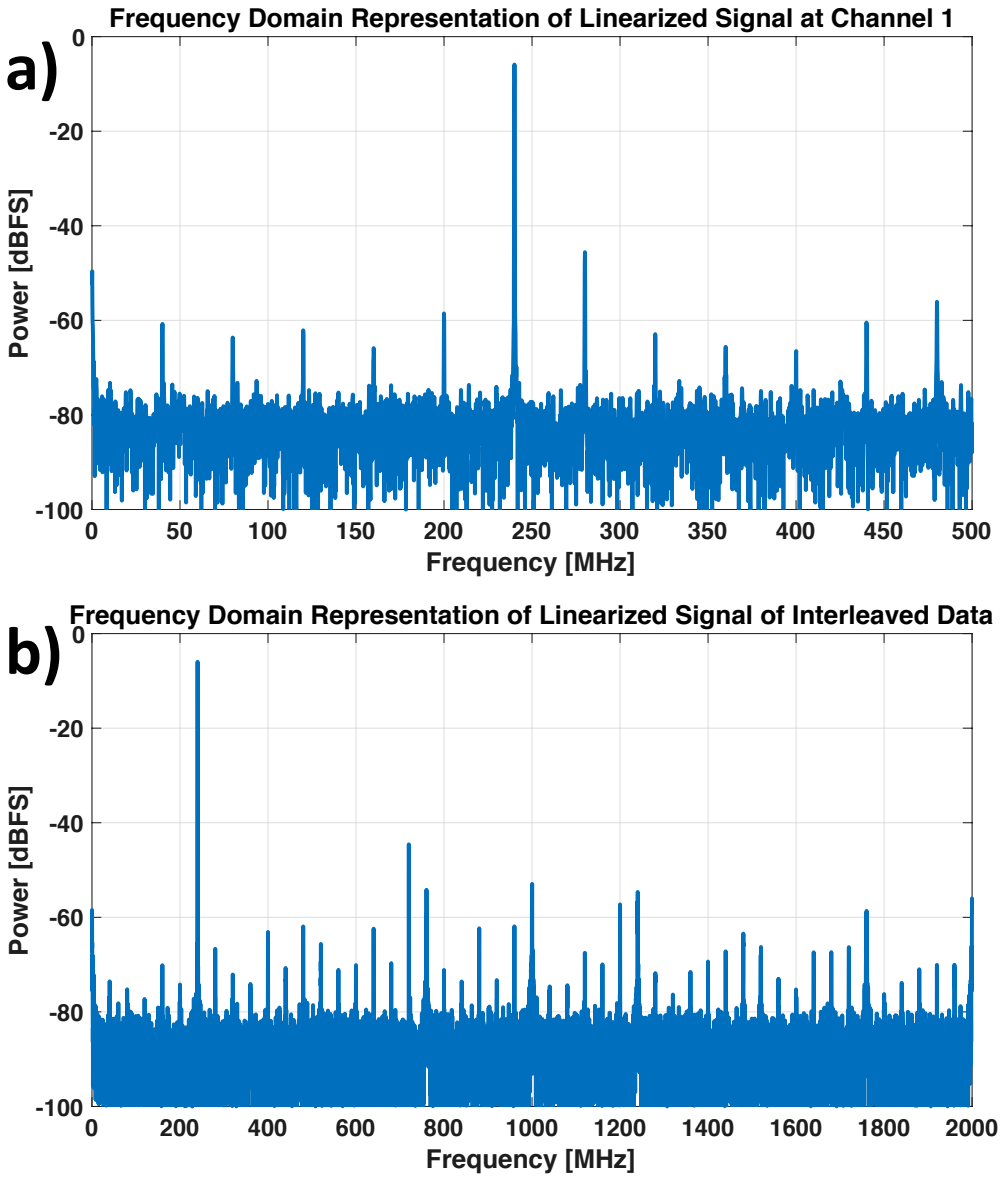

Figure 4.15: Frequency domain representation of single channel and interleaved system after modulator linearization. Frequency resolution for both cases is ∼122kHz due to 8192ns time window. Spectral representation of (a) Channel 1, (b) interleaved data.

Table 4.1: Performance metrics calculated from the Fourier Spectra of the raw and linearized data.

	SNR	SFDR	SINAD
Ch1-Raw	42.01dB (6.69b)	22.95dB (3.52b)	20.29dB (3.08b)
Ch1-Linearized	38.79dB (6.15b)	39.67dB (6.30b)	34.27dB (5.40b)
Ch2-Raw	41.21dB (6.55b)	22.97dB (3.52b)	20.28dB (3.08b)
Ch2-Linearized	38.19dB (6.05b)	38.52dB (6.11b)	33.22dB (5.23b)
Ch3-Raw	39.84dB (6.33b)	23.04dB (3.53b)	20.37dB (3.09b)
Ch3-Linearized	36.5dB (5.77b)	38.17dB (6.05b)	32.14dB (5.05b)
Ch4-Raw	41.81dB (6.65b)	22.95dB (3.52b)	20.29dB (3.08b)
Ch4-Linearized	38.29dB (6.07b)	39.04dB (6.2b)	33.58dB (5.29b)
Interleaved-Raw	38.47dB (6.10b)	22.98dB (3.52b)	20.27dB (3.07b)
Interleaved-Linearized	36.43dB (5.76b)	38.62dB (6.12b)	31.57dB (4.95b)
Interleaved-Gain and Offset Matched	36.43dB (5.76b)	38.62dB (6.12b)	33.04dB (5.2b)

However, still, $\sim$2.3bits are lost. Due to the lack of balanced detection, all received signals are positive that limits us to use the negative quantization levels of the ADC. It costs us 1bit directly. Remaining bits can be connected to the optical and electronic noises, modulator bandwidth limitations, optical sampling jitter, electronic ADC jitter (160fs RMS), etc. In this numerical study, optical device parameters are selected similar to the components used in the experimental study. However, extra electronic components are added to amplify and filter the signal. Also, the repetition rate of the pulse generator is selected 1GHz to employ a state of the art ADC (HMCAD1511) [89]. Consequently, to observe optical problems in the experimental setup, the state of the art electronic components are selected in the numerical study.

4.3 Experimental Results

To demonstrate the system performance, the proposed ADC system is established in the lab environment. In the experiments, we used two CW lasers with >1mW average power. Here, we used tunable lasers (C band or C+L band) for flexibility that can be replaced with ITU grid lasers later on. After polarization controllers, the lasers are combined with

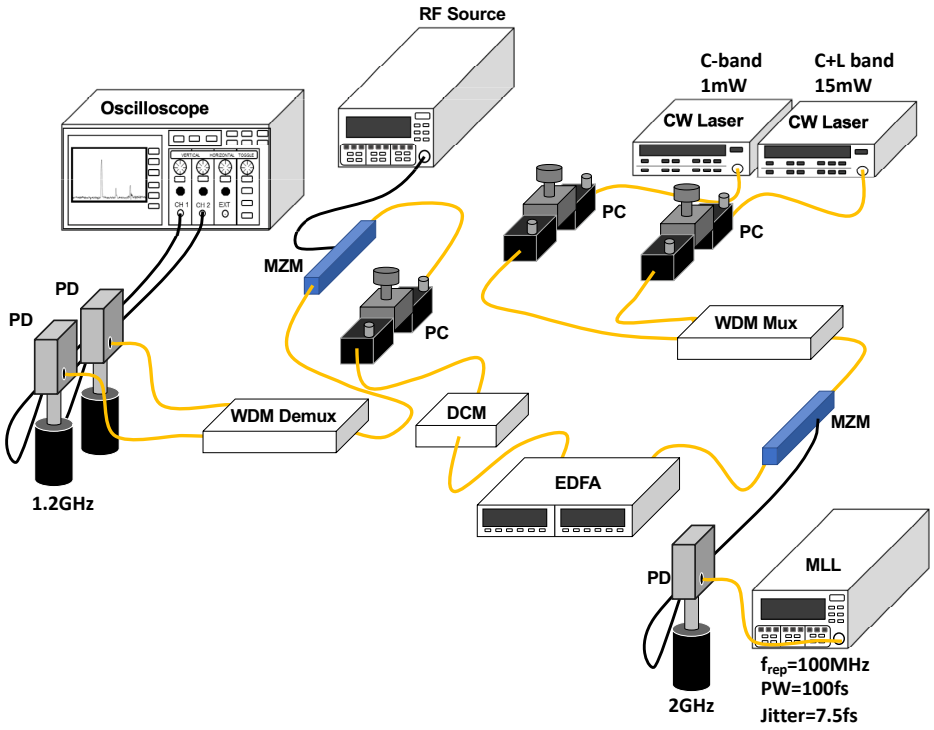

Figure 4.16: Experimental setup for two channel optically interleaved system. RF amplifiers after the photodiodes and DC sources to bias modulators are not shown.

a WDM multiplexer. Wavelength interleaved signal is sent to an 8GHz $LiNbO_3$ MZM to achieve pulsation. The RF input of the modulator is driven by a pulse generator. Due to lack of high-speed RF pulse generator in the lab, we designed a pulse generator based on a mode locked-laser (MLL) that produces short pulses ($\sim$100fs) with 100MHz repetition rate and 7.5fs timing jitter. Such pulses are detected with a 2GHz PIN detector. The modulator is biased at its minimum transmission point and RF pulses are amplified to achieve full swing or at least better than >70% modulation depth. At this step, 2GHz photodiode is the bottleneck to determine the pulse width of the samplers. After pulsation, a dispersion compensation module with 1350ps/nm is used to temporally distribute wavelengths and achieve 200MHz sampling rate. All of the pulses are amplified with a C-band EDFA to increase peak power. After a polarization controller, 2GHz pulse train is modulated with an analog input signal up to 100MHz in second MZM that is biased at quadrature point. To increase modulation depth, the analog input signal is amplified before connected to the

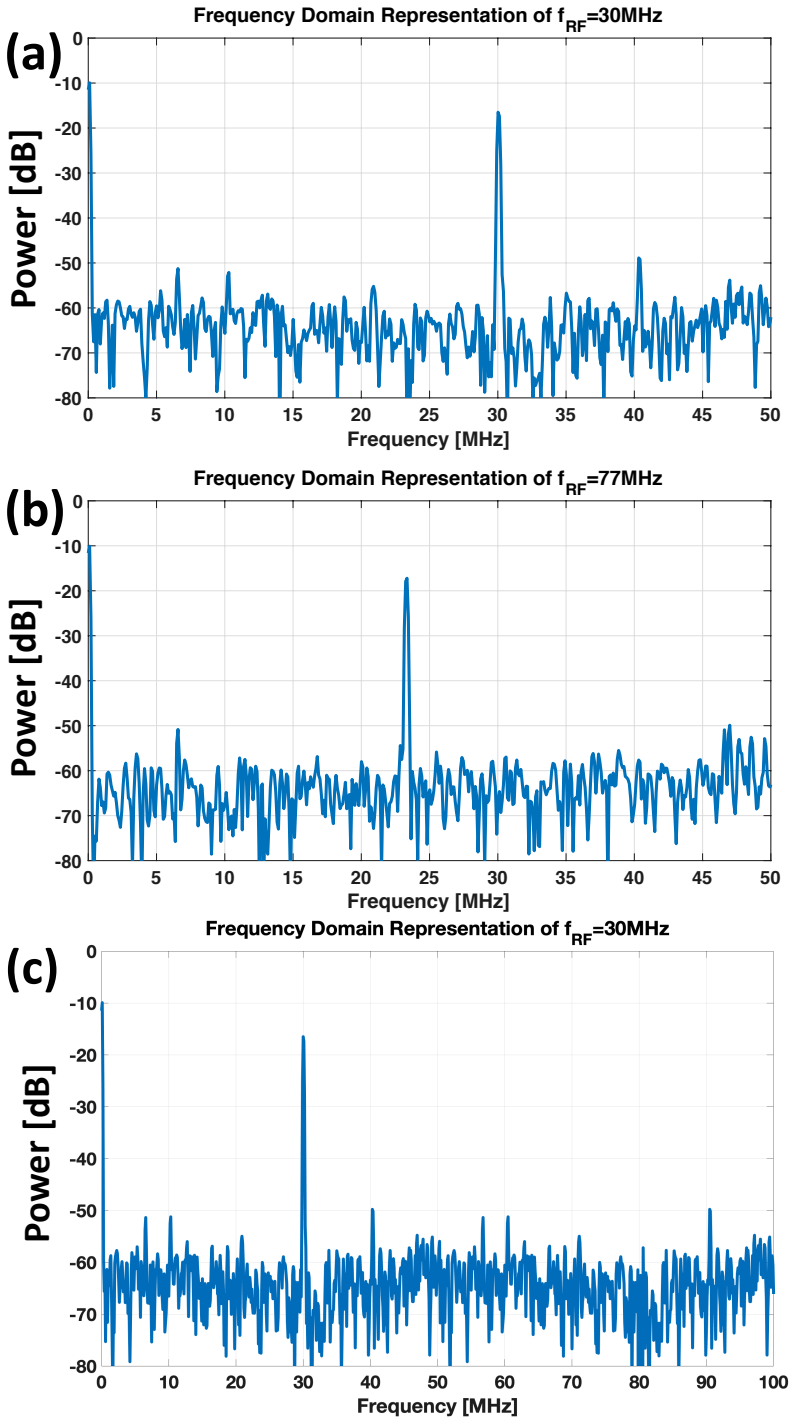

Figure 4.17: Experimental results for single channel where given analog input signals are (a) 30MHz and (b) 77MHz. Since the MLL repetition rate is 100MHz, Nyquist bandwidth is 50MHz, therefore 77MHz is aliased to 23MHz as seen in (b). Also, interleaving of both channels for 30MHz analog input is shown in (c).

MZM. Later, the modulated pulse train is down-converted to the fundamental repetition rate with a WDM demultiplexer that separates the wavelengths. Each wavelength is detected with a 1.2GHz InGaAs PIN photodiode and generated electrical signal is amplified before going to oscilloscope channels for quantization. The acquired digital data from two ADCs are recorded and further post-processed in MATLAB to extract the analog input signal. The post-processing includes: (i) modulator linearization, (ii) interleaving the data from N channels, (iii) Fourier transform, (iv) spectral analysis to identify distortion tones and interleaving spurs, and (v) performance parameter calculation including SNR, SFDR, THD, SINAD, and ENOB.

Initially, a single-channel experiment is conducted to see the performance of the system. Here, the fundamental repetition rate of the MLL (∼100MHz) is employed and optical signal sampled 30MHz and 77MHz RF input signals. The spectrums of both cases are shown in Fig. 4.17(a)-(b). The system shows 18.34dB SINAD (2.75b ENOB) for 30MHz and 17.4dB SINAD (2.6b ENOB) for 77MHz. Additionally, interleaving of both channels for 30MHz analog input is shown in 4.17.

The experimental results are limited due to component availability. The main limiting factor is optical power. Since we are employing 1mW CW lasers, the signal level is decreasing a lot after pulse modulation. Even though we amplify the signal with an EDFA that can reach 100mW output power, the signal quality degrades due to wideband amplified spontaneous emission (ASE) noise. If CW lasers can be increased to 20mW level, system SNR will improve 13dB. Since one of the CW lasers can reach 15mW output power, a single-channel experiment is conducted to show the ENOB improvement with respect to the increase in optical input power. Figure 4.18 shows the spectrum of 30MHz and 70MHz analog input signals that are sampled with one channel (100MSa/s) of the photonic assisted ADC. It is clearly seen that SINAD of the system is improved more than 10dB. The results show 10.82dB and 10.6dB improvements for 30MHz and 70MHz signals respectively. SINAD for 30MHz signal reaches

to 29.16dB (4.55bits) while SINAD for 70MHz reaches 28dB (4.36bits). This result indicates that the current system is limited by the optical power.

On the other hand, 8GHz modulator bandwidth is limiting the pulse width to 125ps that increases the jitter that is linearly proportional to the pulse width of the sampler. Additionally, the system is mainly limited by the jitter of the pulse generator. Here, MLL that generates 100fs pulses with 7.5fs RMS jitter is employed to minimize the source jitter. However, to achieve >80% modulation depth in the modulator, optical pulses are detected with low speed (∼2GHz) photodiodes and photodiode current is amplified with RF amplifiers. Due to noise addition and pulse broadening during this process, the source jitter increases.

Moreover, the cross-talk between the pulses while propagating along the dispersion compensation module causes pulse amplitude variations. This problem can be resolved with using dual-output MZM that creates complementary outputs. In balanced detection, if you sum these outputs, you will get the mean value and their difference gives twice the modulation that improves the SNR of the system 6dB. In this way, all ADC bits can be utilized and peak power variation of the sampler can be corrected [90, 91].

In the electronic part, we used oscilloscope channels as electronic ADC that has an 8-bit resolution, but 1.5ps RMS timing jitter. Today, it is possible to have electronic ADCs with <100fs RMS jitter.

To sum up, the performance of the system can be improved with increasing received power, employing linear dispersive medium, using large bandwidth (e.g. 40GHz) modulators and detectors, employing dual output modulator and balanced detection, and state of the art ADC.

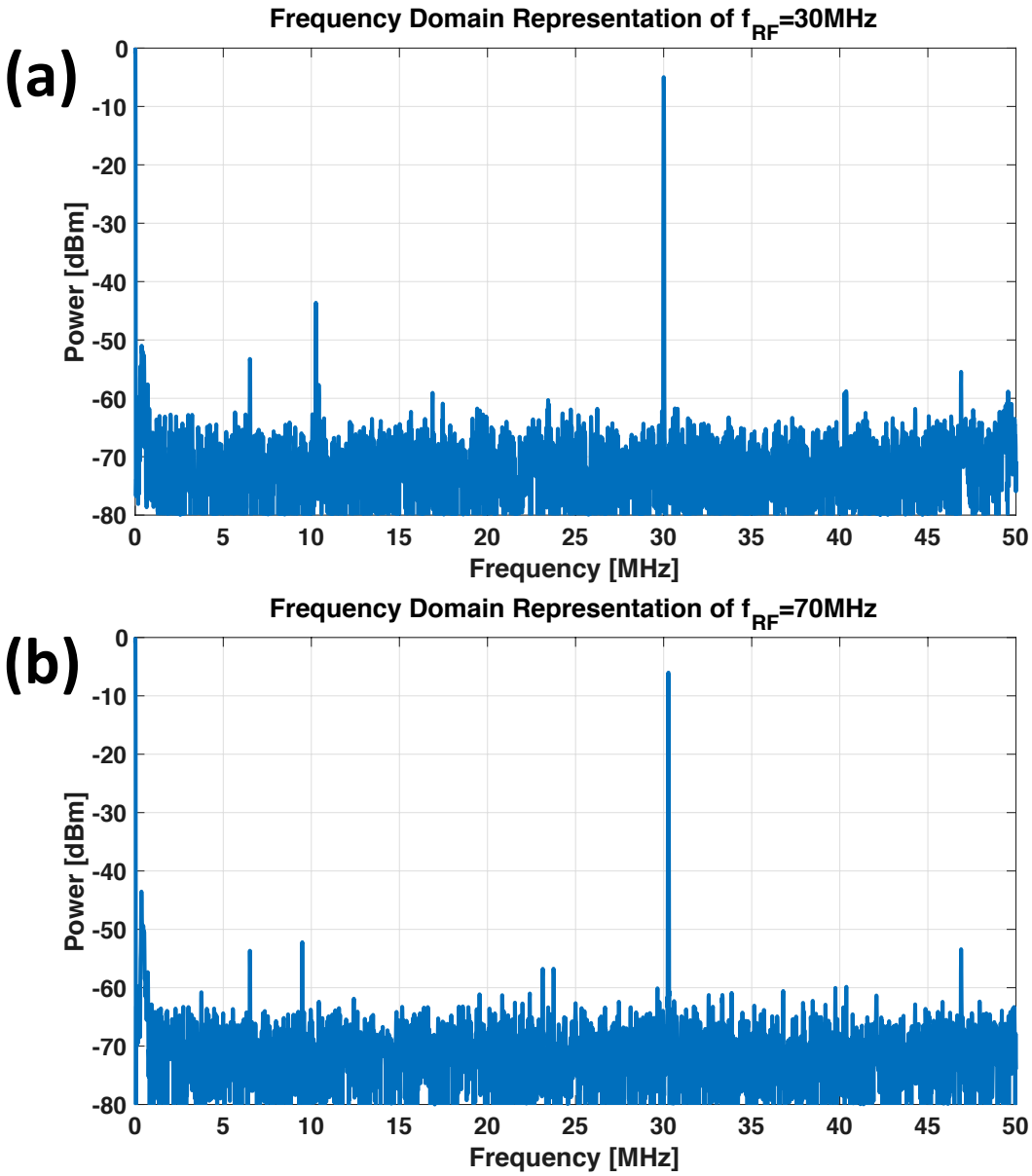

Figure 4.18: Experimental results for single channel when 15mW CW laser is used. Given analog input signals are (a) 30MHz and (b) 70MHz. Since the MLL repetition rate is 100MHz, Nyquist bandwidth is 50MHz, therefore 70MHz is aliased to 30MHz as seen in (b).

4.4 Conclusion

In this chapter, we demonstrated the photonic assisted continuous-time ADC system. The proposed system is an optical front end for electronic ADCs to increase their sampling rate. In addition, we performed proof of concept experiments along with the theoretical and numerical analysis to assess the performance of the proposed system. The performance of the system can be improved with further optimization of the power levels, amplifications, delays, and bandwidth.

Chapter 5

Performance Evaluation of Proposed PACT-ADC System

5.1 Introduction

The proposed ADC system is theoretically and numerically investigated in Chapter 4. Also, proof of concept experiment is completed to demonstrate the feasibility of the proposed system. However, the experimental results do not reflect the full potential of the proposed system due to resource limitations in the lab. The current experimental setup is limited due to received power and optical sampler jitter. In this chapter, I will discuss these limitations and demonstrate the methods for improvement.

5.2 Power Analysis

In order to understand the power requirements of the system, we need to check the detector and post electronics noise currents and the received optical peak power. Photodetector noises

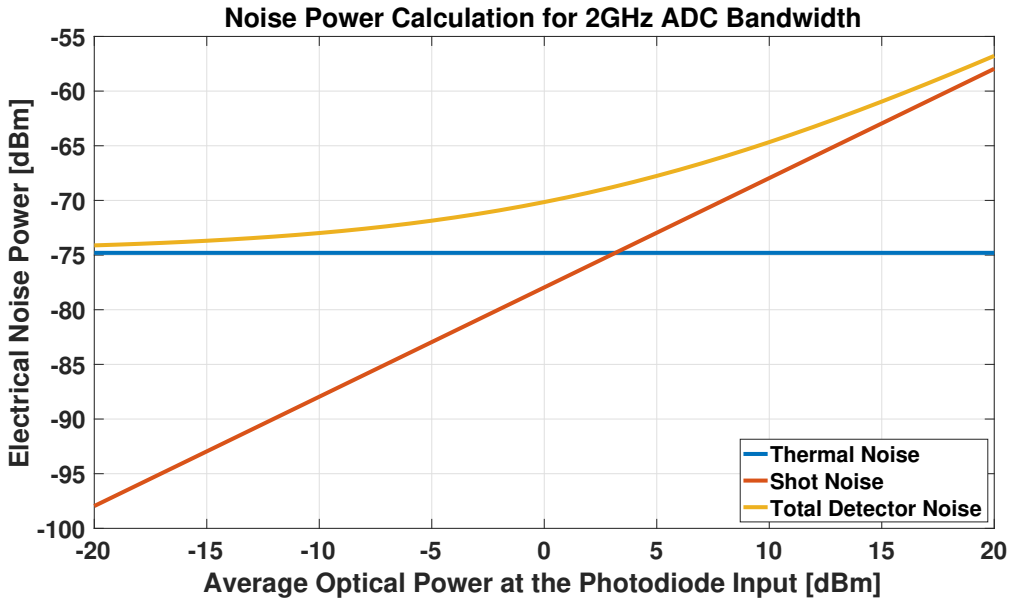

Figure 5.1: Components of detector noise for 2GHz bandwidth including thermal noise, shot noise, and dark current.

are thermal noise, shot (quantum) noise and dark current due to operation under reverse biasing.

$$i_{n,thermal} = \sqrt{\frac{4k_B T BW_{ADC}}{R_L}} \tag{5.1a}$$

$$i_{n,shot} = \sqrt{2qI_{avg}BW_{ADC}} = \sqrt{2qRP_{avg}BW_{ADC}} \tag{5.1b}$$

where k_B is the Boltzmann constant, T is temperature in Kelvin, R_L is the load resistance, BW_{ADC} is ADC bandwidth assumed 2GHz, q is the electron charge, I_{avg} is the average photocurrent, P_{avg} is the average optical power at each channel, and R is the responsivity of the photodiode in A/W.

Figure 5.1 shows the amount of noise power generated from the photodiode (Thorlabs DET01CFC) [92] with 50Ω load resistance and 0.5 A/W responsivity for 2GHz ADC bandwidth. Shot noise becomes dominant above 3dBm average optical power at the photodiode.

As it is seen in Eq. 5.1b, shot noise is related to the average photocurrent. For nonstationary

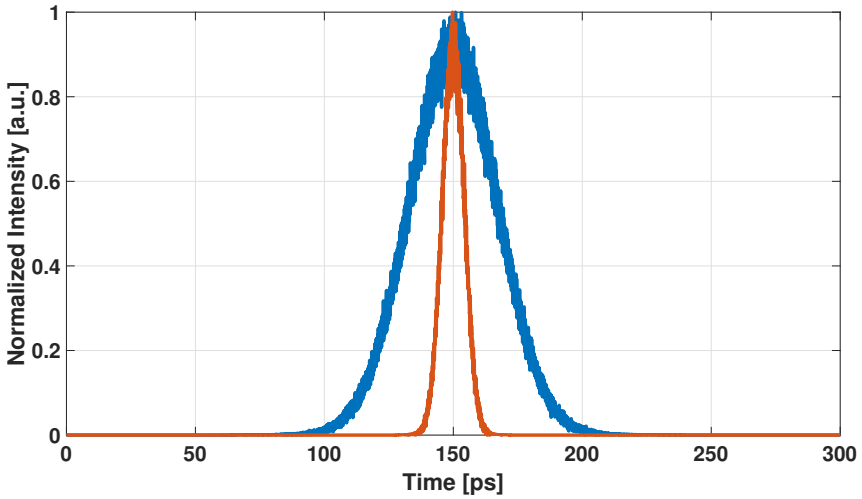

Figure 5.2: Shot noise effect on nonstationary photocurrent for narrow and broad pulses with same average power.

photocurrent, the shot noise current variance can be linked to the average photocurrent only through time averaging. Therefore, there will be more noise component at the peak of the pulse and less at the tails as seen in Fig. 5.2. In addition, short pulses will experience less penalty in terms of jitter from amplitude variations even though average photocurrents, hence noise variances are the same for both cases [93, 94].

In order to determine the noise performance of the system, we need to find the signal power for average optical power at the photodiode input. Since ADC bandwidth is set to 2GHz for noise calculations for 1GSa/s sampling system, all short pulses will broaden due to low bandwidth which will limit the peak power, hence SNR. Signal power is computed using the RMS value at 2GHz bandwidth such as

$$I_{rms} = \left(\frac{I_{pp}/2}{\sqrt{2}} \right) \tag{5.2}$$

where I_{pp} is the difference between peak amplitude of the pulses at maximum and minimum transmission that is equal to maximum peak amplitude at each channel (I_p) when 100% modulation depth is achieved. Peak current at the channel is related to the average channel

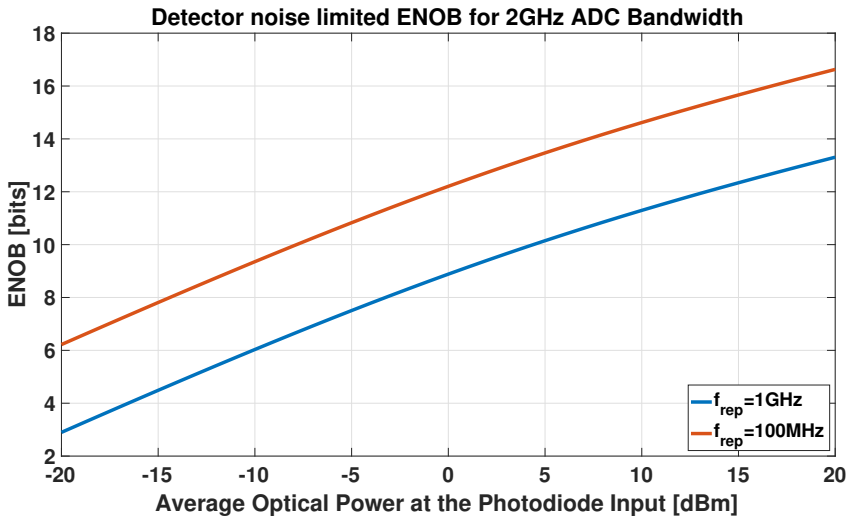

Figure 5.3: Achieavable ENOB for average optical channel power available.

power as in

$$I_p = R \times \left[P_{avg} \left(\frac{T_{rep}}{\tau} \right) \right] \left(\frac{BW_{ADC}}{BW_{filter}} \right) \tag{5.3}$$

where τ is the pulsewidth of the optical sampler, $\mathrm{T}_{rep} = \frac{1}{f_s}$ is the fundamental repetition rate of the sampler. Here, T_{rep} is assumed 1ns due to 1GSa/s sampling rate of electronic ADCs. It is important to fully utilize channel filter bandwidth to achieve short pulsewidth and limit the conversion losses. For Gaussian pulses, time bandwidth product (TBP=$\tau \times \mathrm{BW}_{filter}$) is equal to ≈0.44. After inseting Eq. 5.3 into Eq. 5.2, the RMS signal current will be

$$I_{rms} = \frac{1}{2\sqrt{2}} R P_{avg} \frac{T_{rep} BW_{ADC}}{0.44} \tag{5.4}$$

The SNR of the system can be calculated from here.

$$SNR = 20log_{10} \left(\frac{I_{rms}}{i_{n,tot}} \right) = 6.02 \times ENOB + 1.76 \tag{5.5}$$

Figure 5.3 demonstrates the achievable ENOB for the average channel power considering only detector noise and assuming optical pulses have an infinite extinction ratio, therefore

the optical system is limited by detector noise. On the other hand, the achievable average power at the photodiode input is <7dBm for 4 channel system, since EDFA output can be as high as 23dBm, therefore each channel can reach up to 17dBm. Also, the total loss after EDFA due to insertion loss of the modulator and WDM multiplexer, and connectors will be ∼10dB. However, the modulator extinction ratio and noise from laser and pulse generator will limit the signal power percentage of this average power. For example, 13dB extinction ratio of the modulator will leave 5% of the peak power in zero region. In no saturation case, such photons will be amplified similar to the signal photons, therefore a high amount of power will go to zero region. As an example, 40GHz modulator will provide 10ps pulses that have high peak power, but the remaining region of 990ps will have 5% of that peak power, therefore total energy of the pulse is 5.21× lower than the total energy in the zero region. This will keep the detector noise same, but SNR will decrease 15.86dB causing 2.34bit loss due to signal power loss. State of the art higher extinction ratio (>30dB) modulators that are commercially available in the market can eliminate this problem.

5.3 Optical Sampler Jitter Analysis

The proposed system employs RF pulses to generate optical sampler pulses. Therefore, it is suitable to be used with RF systems. Due to the limited RF pulse generator availability in the lab, we built a homemade RF pulse generator using MLL. MLL generates 100MHz pulses with ∼100fs pulse width and <10fs jitter. Such pulses are detected with a photodiode and amplified to achieve ∼5Vpp amplitude to fully utilize the CW laser power by satisfying 100% modulation depth (Fig. 4.6). The jitter at the output of the amplifier is the combination of MLL jitter (<10fs) and the contributions from detector and amplifier noises. If an RF pulse generator is employed, its jitter performance should be inserted here. However, this is not the position where optical sampling occurred. Optical sampling occurs after modulating the

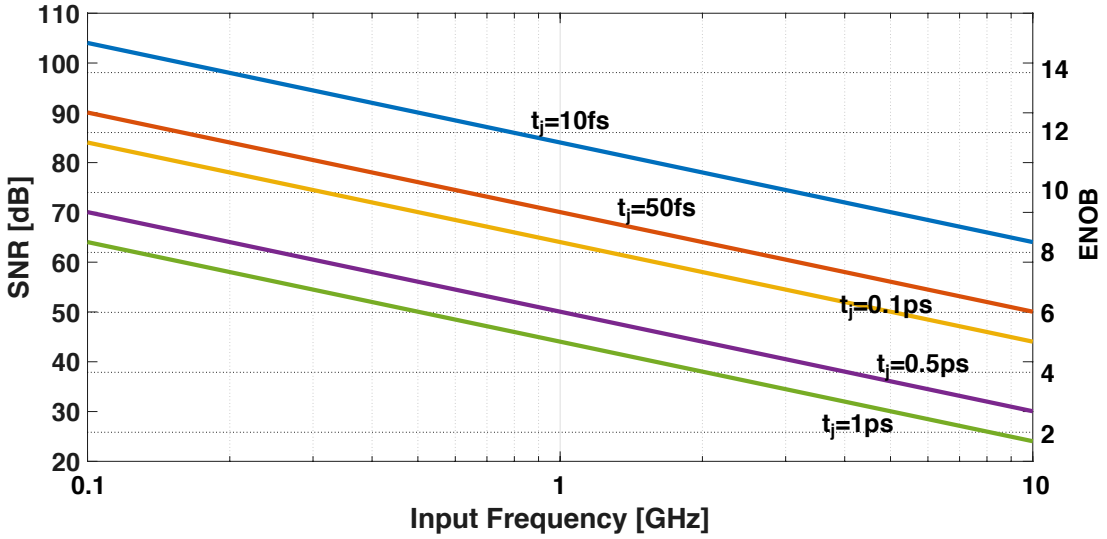

Figure 5.4: SNR degradation due to jitter for GHz analog input frequencies.

CW laser with such pulses, delaying the pulses to achieve high repetition rate sampler and amplifying them. Therefore, the noise performance of these components also affects jitter. In the optical part, the main noise contributor is EDFA due to 3-5dB noise figure.

Figure 5.4 demonstrates the 20dB/decade decay of the SNR with respect to timing jitter and frequency of the analog input signal according to Eq. 5.6 [95].

$$SNR = 20log_{10}\left[\frac{1}{2\pi f t_j}\right] \tag{5.6}$$

When we consider the theoretical timing jitter formula $\left(\Delta t_{ml} \approx \tau\sqrt{\frac{1}{E_{pulse}}\frac{h\nu}{\tau_c}T_M}\right)$ of mode-locked lasers [96, 97], it is clearly seen that low detector bandwidth will increase the jitter. When there is no saturation, while the pulse width (τ) is increasing, pulse energy will decrease at the same amount causing $\sqrt{\frac{BW_{MLL}}{BW_{det}}}$ times jitter increase. If the detector saturates, both of the parameters will increase and further increase the jitter. Employing wide bandwidth photodiode and modulator can solve this issue with a penalty of increasing noise bandwidth.

On the other hand, noise-related fluctuations will have the same effect as jitter. The noise of

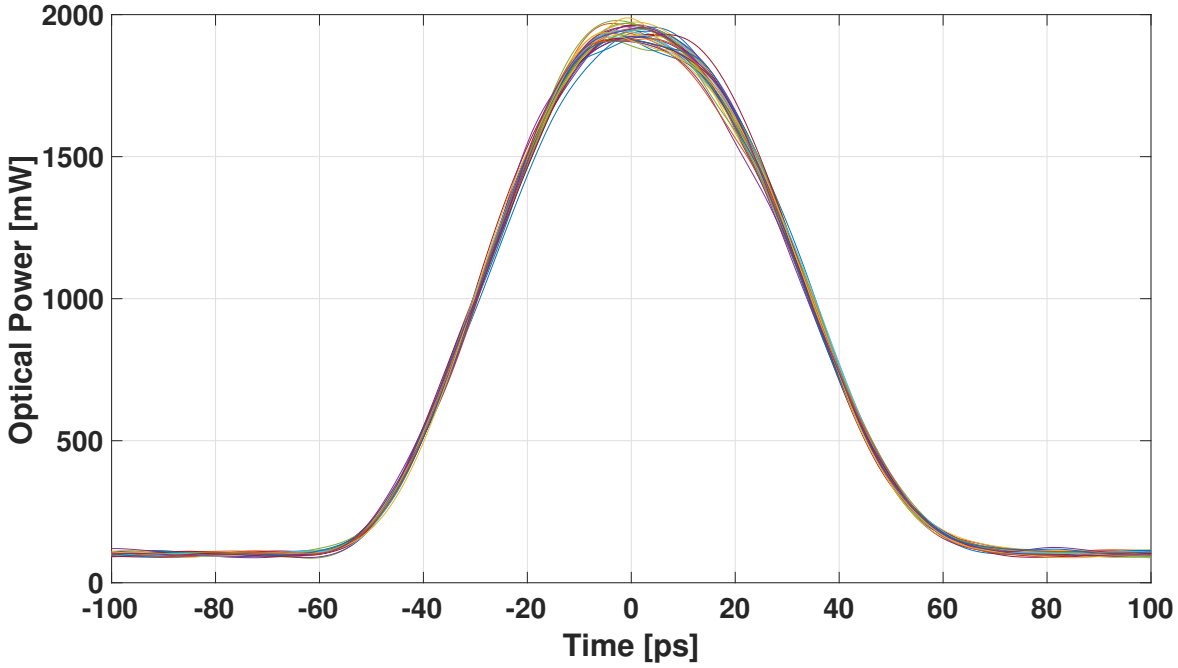

Figure 5.5: Jitter of the high repetition rate sampler. MLL jitter of 7.5fs is elevated by detector noise and RF amplifier noise. Additionally, ASE noise in the EDFA increases the jitter further. Numerically calculated jitter is ∼0.4ps.

the pulse generator is mainly limited by the amplifier noise. By employing highly linear high power detectors, the need for amplifier can be eliminated and the system will be limited to detector noise. Figure 5.5 demonstrates the total jitter of the sampler (∼0.4ps) that includes the MLL jitter of 7.5fs and jitter caused by the noise generated in the detector, RF amplifier, and EDFA. The limited extinction ratio of the modulator is also seen in the figure.

5.4 Demultiplexer Channel Isolation

Another limiting factor for the performance is channel isolation of the demultiplexer. The leaked power from adjacent channels acts as a noise source, therefore it should be minimized below the least significant bit (LSB) of the ADC when the optical power is amplified to the full-scale range of the electronic ADCs after detection. As an example, 10-bit ADC

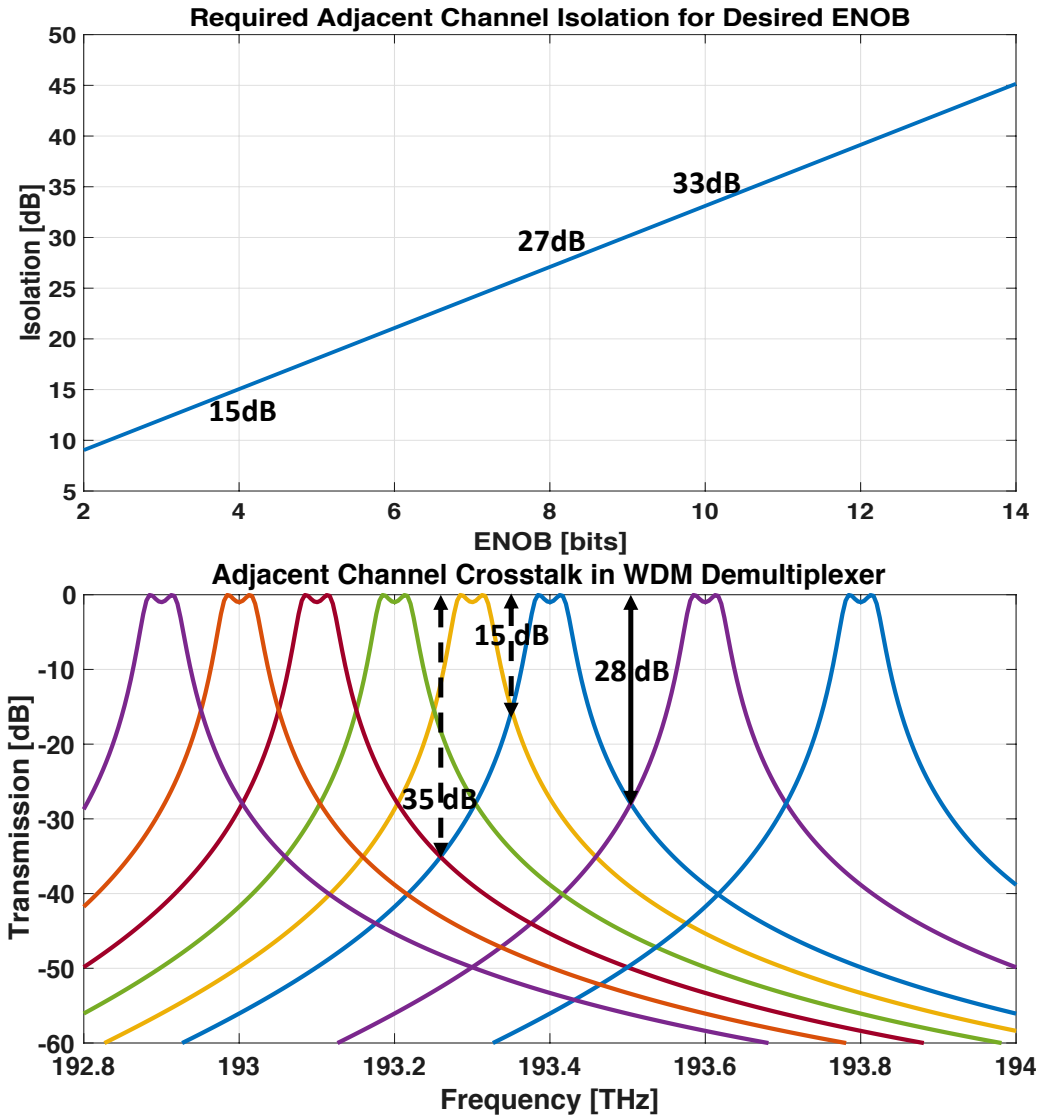

Figure 5.6: WDM Demultiplexer Channel Selection for Desired ENOB. (a) Adjacent channel isolation requirements for desired ENOB. (b) Transmission of channels in a DWDM demultiplexer that is modeled as 2^{nd} order Chebyshev Filter with 40GHz passband and 100GHz channel spacing. All channels are shown on the left, but only even channels are shown on the right. It shows that adjacent channel isolation of 15dB allows only 4 ENOB. Using only odd or even channels can allow 8 ENOB. For higher ENOB values more channels should be omitted.

requires ∼33.1dB isolation as shown in Fig. 5.6(a) where 30.1dB is due to 10-bit resolution ($10 \times log_{10}(2^{10}) = 30.1dB$) and 3dB is due to two symmetric adjacent channels. Effect of non-adjacent channels is ignored due to a much lower contribution to the noise.

Figure 5.6(b) demonstrates transmission spectra of DWDM demultiplexer channels that are modeled as 2^{nd} order Chebyshev Filter with 40GHz passband and 100GHz channel spacing. All channels are shown on the left, but only even channels are shown on the right. It shows that adjacent channel isolation of 15dB allows only 4 ENOB. Using only odd or even channels (200GHz spacing) can achieve 28dB isolation and allow 8 ENOB. For higher ENOB values more channels should be omitted to make the system 40GHz passband but >300GHz channel spacing.

This isolation requirement will limit the number of interleaving channels for high repetition rate sampling. For example, in C-band operation (1530-1565nm), the amount of interleaving is limited to <16 for 10-bit resolution.

5.5 Conclusion

In this chapter, the performance limitations of the proposed system are investigated. The system is mainly limited by the jitter and the received power. The ideas to improve jitter performance and increase received power are introduced.

Chapter 6

Conclusion

In summary, this thesis has investigated how multi-wavelength and multi-tone laser sources can be used for light detection and ranging, photonic Doppler velocimetry, and photonic assisted analog to digital conversion applications. Depending on the application one or selected number of properties of multiwavelength or broadband laser sources such as dispersion, nonlinearity, coherence, etc can be used to enable creative engineering solutions. In ranging, single-shot measurement capability is enabled along with improvement in measurement accuracy. In velocimetry, direction information can be acquired besides the speed information with the help of extra wavelengths or single-sideband modulation. Additionally, the sampling rate multiplication in the photonic assisted ADC is directly proportional to the number of wavelengths used. The thesis covers the analysis of all three multi-wavelength based applications; Lidar, photonic Doppler velocimetry, and photonic assisted ADC.

The early part of the thesis focuses on Lidar and velocimetry. The theoretical and numerical analysis of the proposed multi-tone Lidar method is presented. Additionally, the feasibility of the system is demonstrated with proof of concept experiments. Initially, the range of a target mirror is measured with <1cm range resolution by employing 1550nm light source and

multiple RF tone modulations from 50MHz to 6GHz. Additionally, the velocity measurement capability of the system has been demonstrated by using a target attached to a speaker membrane or a stepper motor. Up to 10cm/s speeds are measured with a stepper motor. Finally, the effect of motion on the range measurements are theoretically investigated. Consequently, high precision range and velocity measurement capability of the MTCW Lidar is demonstrated with reflective targets. Further applications of the proposed method for scattering targets can be implemented by engineering the source power and receiver sensitivity.

The second part of the thesis presents a pulse-modulated CW laser-based system and investigates its performance in time-interleaved photonic assisted ADCs. The study consists of theoretical analysis, numerical investigation with an experimental demonstration. The proposed system is an optical front end for electronic ADCs to increase their effective sampling rate through time and wavelength interleaving in the optical domain. Sources that limit the performance of the ADC are investigated. In summary, system performance is limited by low optical power and source jitter from the pulse generator. The methods to overcome such limitations are presented.

To sum up, optical methods are employed in various applications to improve system performance and open new fields. The MTCW Lidar method applies to several fields from autonomous vehicles to earth observation from satellites. On the other hand, photonic assisted ADC is capable of providing high sampling rates by employing low jitter (<10 fs) time and wavelength interleaved optical sources to sample the analog input signal and electronic ADCs for quantization.

Bibliography

[1] Barry L. Stann, William C. Ruff, and Zoltan G. Sztankay. Intensity-modulated diode laser radar using frequency-modulation/continuous-wave ranging techniques. *Optical Engineering*, 35(11):3270–3279, 1996.

[2] Albert Ansmann, Ulla Wandinger, Maren Riebesell, Claus Weitkamp, and Walfried Michaelis. Independent measurement of extinction and backscatter profiles in cirrus clouds by using a combined raman elastic-backscatter lidar. *Applied Optics*, 31(33):7113–7131, 1992.

[3] Arthur R. Braun, C. Y. Chien, Scott Coe, and Gerard A. Mourou. Long range, high resolution laser radar. *Optics Communications*, 105(1):63–66, 1994.

[4] Jack L. Bufton, James B. Garvin, John F. Cavanaugh, Luis A. Ramos-Izquierdo, Thomas D. Clem, and William B. Krabill. Airborne lidar for profiling of surface topography. *Optical Engineering*, 30(1):72–79, 1991.

[5] Rodanthi-Elisavet Mamouri and Albert Ansmann. Potential of polarization/raman lidar to separate fine dust, coarse dust, maritime, and anthropogenic aerosol profiles. *Atmospheric Measurement Techniques*, 10(9):3403–3427, 2017.

[6] Peter P. Sullivan, Chin-Hoh Moeng, Bjorn Stevens, Donald H. Lenschow, and Shane D. Mayor. Structure of the entrainment zone capping the convective atmospheric boundary layer. *Journal of the Atmospheric Sciences*, 55(19):3042–3064, 1998.

[7] Jiannong Quan, Yang Gao, Qiang Zhang, Xuexi Tie, Junji Cao, Suqin Han, Junwang Meng, Pengfei Chen, and Delong Zhao. Evolution of planetary boundary layer under different weather conditions, and its impact on aerosol concentrations. *Particuology*, 11(1):34–40, 2013.

[8] Subramanian Ramasamy, Roberto Sabatini, Alessandro Gardi, and Jing Liu. LIDAR obstacle warning and avoidance system for unmanned aerial vehicle sense-and-avoid. *Aerospace Science and Technology*, 55:344–358, 2016.

[9] John P. Godbaz, Michael J. Cree, and Adrian A. Dorrington. Closed-form inverses for the mixed pixel/multipath interference problem in amcw lidar. In *Computational Imaging X*, volume 8296, page 829618. International Society for Optics and Photonics, 2012.

[10] Daniel J. Lum, Samuel H. Knarr, and John C. Howell. Frequency-modulated continuous-wave LiDAR compressive depth-mapping. *Optics Express*, 26(12):15420–15435, 2018.

[11] George C. Valley. Photonic analog-to-digital converters. *Optics Express*, 15(5):1955–1982, 2007.

[12] Andrew J. Benedick, James G. Fujimoto, and Franz X. Kärtner. Optical flywheels with attosecond jitter. *Nature Photonics*, 6(2):97, 2012.

[13] S. P. Singh and N. Singh. Nonlinear effects in optical fibers: Origin, management and applications. *Progress in Electromagnetics Research*, 73:249–275, 2007.

[14] Govind P. Agrawal. *Nonlinear Fiber Optics*. Academic Press, 3rd edition, 2009.

[15] Ozdal Boyraz. 285A Lecture Slides 3, 2014. [Online; accessed 10-June-2014].

[16] Govind P. Agrawal. *Fiber-Optic Communication Systems*. John Wiley & Sons, 3rd edition, 2002.

[17] Mohammed N. Islam, Linn F. Mollenauer, Roger H. Stolen, Jay R. Simpson, and Hen-Tai Shang. Cross-phase modulation in optical fibers. *Optics Letters*, 12(8):625–627, 1987.

[18] Brian R. Washburn. *Dispersion and nonlinearities associated with supercontinuum generation in microstructure fibers*. PhD thesis, Georgia Institute of Technology, 2003.

[19] Salih K. Kalyoncu. *Raman based dispersive systems for short pulse generation and optical signal processing*. PhD thesis, University of California, Irvine, 2013.

[20] Corning. Corning SMF-28 optical fiber product information, 2002. [Online; accessed 10-Nov-2018].

[21] RP Photonics Encyclopedia. Erbium-doped gain media. [Online; accessed 10-June-2018].

[22] Haisheng Rong, Shengbo Xu, Oded Cohen, Omri Raday, Mindy Lee, Vanessa Sih, and Mario Paniccia. A cascaded silicon Raman laser. *Nature Photonics*, 2(3):170, 2008.

[23] Roger H. Stolen. Fundamentals of Raman amplification in fibers. In Mohammed N. Islam, editor, *Raman amplifiers for telecommunications*, volume 1, chapter 2. Springer, 2004.

[24] Chandrasekhara V. Raman. A new radiation. *Indian Journal of Physics*, 2:387–398, 1928.

[25] Hermann A. Haus and Masataka Nakazawa. Theory of the fiber Raman soliton laser. *JOSA B*, 4(5):652–660, 1987.

[26] Jake Bromage. Raman amplification for fiber communications systems. *Journal of Lightwave Technology*, 22(1):79, 2004.

[27] Jason Chou, Ozdal Boyraz, Daniel Solli, and Bahram Jalali. Femtosecond real-time single-shot digitizer. *Applied Physics Letters*, 91(16):161105, 2007.

[28] Salih K. Kalyoncu, Yuewang Huang, En-Kuang Tien, Enver Adas, Dogukan Yildirim, and Ozdal Boyraz. Noise performance of time stretch system with distributed and discrete amplifiers. In *CLEO: Science and Innovations*, page CTuA7. Optical Society of America, 2011.

[29] Albert Ansmann and Detlef Müller. Lidar and atmospheric aerosol particles. In *Lidar*, pages 105–141. Springer, 2005.

[30] Thorsten Luettel, Michael Himmelsbach, and Hans-Joachim Wünsche. Autonomous ground vehiclesconcepts and a path to the future. *Proceedings of the IEEE*, 100(Special Centennial Issue):1831–1839, 2012.

[31] Michael Himmelsbach, Andre Mueller, Thorsten Lüttel, and Hans-Joachim Wünsche. Lidar-based 3D object perception. In *Proceedings of 1st international workshop on cognition for technical systems*, volume 1, 2008.

[32] Kiyosumi Kidono, Takeo Miyasaka, Akihiro Watanabe, Takashi Naito, and Jun Miura. Pedestrian recognition using high-definition lidar. In *2011 IEEE Intelligent Vehicles Symposium (IV)*, pages 405–410. IEEE, 2011.

[33] Romuald Aufrère, Jay Gowdy, Christoph Mertz, Chuck Thorpe, Chieh-Chih Wang, and Teruko Yata. Perception for collision avoidance and autonomous driving. *Mechatronics*, 13(10):1149–1161, 2003.

[34] Patrick Y. Shinzato, Denis F. Wolf, and Christoph Stiller. Road terrain detection: Avoiding common obstacle detection assumptions using sensor fusion. In *2014 IEEE Intelligent Vehicles Symposium Proceedings*, pages 687–692. IEEE, 2014.

[35] Zhaodong Chen, Rongwei Fan, Xudong Li, Zhiwei Dong, Zhigang Zhou, Guangchao Ye, and Deying Chen. Accuracy improvement of imaging lidar based on time-correlated single-photon counting using three laser beams. *Optics Communications*, 429:175–179, 2018.

[36] John P. Godbaz, Michael J. Cree, Adrian A. Dorrington, and Andrew D. Payne. A fast maximum likelihood method for improving amcw lidar precision using waveform shape. In *2009 IEEE SENSORS*, pages 735–738. IEEE, 2009.

[37] John P. Godbaz, Michael J. Cree, and Adrian A. Dorrington. Understanding and ameliorating non-linear phase and amplitude responses in AMCW lidar. *Remote Sensing*, 4(1):21–42, 2012.

[38] Behnam Behroozpour, Phillip A. M. Sandborn, Ming C. Wu, and Bernhard E. Boser. Lidar system architectures and circuits. *IEEE Communications Magazine*, 55(10):135–142, 2017.

[39] Markus-Christian Amann, Thierry M. Bosch, Marc Lescure, Risto A. Myllylae, and Marc Rioux. Laser ranging: a critical review of unusual techniques for distance measurement. *Optical Engineering*, 40, 2001.

[40] Paul McManamon. Field guide to lidar. SPIE, 2015.

[41] Refael Whyte, Lee Streeter, Michael J. Cree, and Adrian A. Dorrington. Application of lidar techniques to time-of-flight range imaging. *Applied Optics*, 54(33):9654–9664, 2015.

[42] Andrew D. Payne, Adrian A. Dorrington, Michael J. Cree, and Dale A. Carnegie. Improved measurement linearity and precision for AMCW time-of-flight range imaging cameras. *Applied Optics*, 49(23):4392–4403, 2010.

[43] Adrian A. Dorrington, Michael J. Cree, Andrew D. Payne, Richard M. Conroy, and Dale A. Carnegie. Achieving sub-millimetre precision with a solid-state full-field heterodyning range imaging camera. *Measurement Science and Technology*, 18(9):2809, 2007.

[44] Eiichi Yoshikawa and Tomoo Ushio. Wind ranging and velocimetry with low peak power and long-duration modulated laser. *Optics Express*, 25(8):8845–8859, 2017.

[45] P. Feneyrou, L. Leviandier, J. Minet, G. Pillet, A. Martin, D. Dolfi, J.-P. Schlotterbeck, P. Rondeau, X. Lacondemine, A. Rieu, and T. Midavaine. Frequency-modulated multifunction lidar for anemometry, range finding, and velocimetry–1. theory and signal processing. *Applied Optics*, 56(35):9663–9675, 2017.

[46] Tatsuo Hariyama, Phillip A. M. Sandborn, Masahiro Watanabe, and Ming C. Wu. High-accuracy range-sensing system based on FMCW using low-cost VCSEL. *Optics Express*, 26(7):9285–9297, 2018.

[47] Phillip A. M. Sandborn, Noriaki Kaneda, Young-Kai Chen, and Ming C. Wu. Dual-sideband linear FMCW lidar with homodyne detection for application in 3D imaging. In *2016 Conference on Lasers and Electro-Optics (CLEO)*, page STu4H.8. Optical Society of America, 2016.

[48] Phillip A. M. Sandborn, Tatsuo Hariyama, and Ming C. Wu. Resolution-enhancement for wide-range non-linear FMCW lidar using quasi-synchronous resampling. In *3D Image Acquisition and Display: Technology, Perception and Applications*, pages DW3F–3. Optical Society of America, 2017.

[49] Taehwan Kim, Pavan Bhargava, and Vladimir Stojanovic. Optimal spectral estimation and system trade-off in long-distance frequency-modulated continuous-wave lidar. In *2018 IEEE International Conference on Acoustics, Speech and Signal Processing (ICASSP)*, pages 1583–1587. IEEE, 2018.

[50] Todd W. Du Bosq and Bradley L. Preece. Frequency modulated continuous wave lidar performance model for target detection. In *Infrared Imaging Systems: Design, Analysis,*

Modeling, and Testing XXVIII, volume 10178, page 101780T. International Society for Optics and Photonics, 2017.

[51] Oscar Batet, Federico Dios, Adolfo Comeron, and Ravil Agishev. Intensity-modulated linear-frequency-modulated continuous-wave lidar for distributed media: fundamentals of technique. *Applied Optics*, 49(17):3369–3379, 2010.

[52] Philipp Trocha, M. Karpov, D. Ganin, Martin H. P. Pfeiffer, Arne Kordts, S. Wolf, J. Krockenberger, Pablo Marin-Palomo, Claudius Weimann, Sebastian Randel, et al. Ultrafast optical ranging using microresonator soliton frequency combs. *Science*, 359(6378):887–891, 2018.

[53] Mohit Gupta, Andreas Velten, Shree K. Nayar, and Eric Breitbach. What are optimal coding functions for time-of-flight imaging? *ACM Transactions on Graphics (TOG)*, 37(2):13, 2018.

[54] Fengqiang Li, Joshua Yablon, Andreas Velten, Mohit Gupta, and Oliver Cossairt. High-depth-resolution range imaging with multiple-wavelength superheterodyne interferometry using 1550-nm lasers. *Applied optics*, 56(31):H51–H56, 2017.

[55] René Dändliker, R. Thalmann, and D. Prongué. Two-wavelength laser interferometry using superheterodyne detection. *Optics letters*, 13(5):339–341, 1988.

[56] Cyrus S. Bamji, Patrick O'Connor, Tamer Elkhatib, Swati Mehta, Barry Thompson, Lawrence A. Prather, Dane Snow, Onur Can Akkaya, Andy Daniel, Andrew D. Payne, et al. A 0.13 μm cmos system-on-chip for a 512$\times$ 424 time-of-flight image sensor with multi-frequency photo-demodulation up to 130 mhz and 2 gs/s adc. *IEEE Journal of Solid-State Circuits*, 50(1):303–319, 2014.

[57] Robert D. Peters, Oliver P. Lay, Serge Dubovitsky, Johan Burger, and Muthu Jeganathan. Design considerations and validation of the MSTAR absolute metrology system. In *Interferometry XII: Techniques and Analysis*, volume 5531, pages 32–43. International Society for Optics and Photonics, 2004.

[58] L Mandel. Complex representation of optical fields in coherence theory. *JOSA*, 57(5):613–617, 1967.

[59] Edward I. Ackerman and Charles H. Cox. Effect of pilot tone-based modulator bias control on external modulation link performance. In *International Topical Meeting on Microwave Photonics MWP 2000 (Cat. No. 00EX430)*, pages 121–124. IEEE, 2000.

[60] Xiaobo Xie, Jacob Khurgin, Jin Kang, and F-S Chow. Linearized mach-zehnder intensity modulator. *IEEE Photonics Technology Letters*, 15(4):531–533, 2003.

[61] Anatol Khilo, Cheryl M. Sorace, and Franz X. Kärtner. Broadband linearized silicon modulator. *Optics Express*, 19(5):4485–4500, 2011.

[62] Xiang Zhu, Tao Jin, Hao Chi, Jinhai Zhou, Guochuan Tong, Dong Li, Lulu Zuo, and Ying Fu. Linearization of two cascaded intensity-modulator-based analog photonic link. *Optical Engineering*, 57(8):080501, 2018.

[63] Mustafa M. Bayer, Rasul Torun, Imam Uz Zaman, and Ozdal Boyraz. A basic approach for speed profiling of alternating targets with Photonic Doppler Velocimetry. In *CLEO: Applications and Technology*, pages AW4K–4. Optical Society of America, 2019.

[64] James W. Bilbro. Atmospheric laser doppler velocimetry: an overview. *Optical Engineering*, 19(4):194533, 1980.

[65] B. J. Jensen, D. B. Holtkamp, P. A. Rigg, and D. H. Dolan. Accuracy limits and window corrections for photon doppler velocimetry. *Journal of applied physics*, 101(1):013523, 2007.

[66] D. H. Dolan. Accuracy and precision in photonic doppler velocimetry. *Review of Scientific Instruments*, 81(5):053905, 2010.

[67] Richard J. Doviak et al. *Doppler radar and weather observations*. Courier Corporation, 2006.

[68] Mount Washington Observatory. World record wind. [Online; accessed 1-Sep-2019].

[69] Jeffrey C. Snyder and Howard B. Bluestein. Some considerations for the use of high-resolution mobile radar data in tornado intensity determination. *Weather and Forecasting*, 29(4):799–827, 2014.

[70] Gordon E. Moore. Cramming more components onto integrated circuits. *Electronics*, 38(8):114–117, 1965.

[71] Robert H. Walden. Analog-to-digital converter survey and analysis. *IEEE Journal on Selected Areas in Communications*, 17(4):539–550, 1999.

[72] Behzad Razavi. Design considerations for interleaved adcs. *IEEE Journal of Solid-State Circuits*, 48(8):1806–1817, 2013.

[73] Anatol Khilo, Steven J. Spector, Matthew E. Grein, Amir H. Nejadmalayeri, Charles W. Holzwarth, Michelle Y. Sander, Marcus S. Dahlem, Michael Y. Peng, Michael W. Geis, Nicole A. DiLello, Jung U. Yoon, Ali Motamedi, Jason S. Orcutt, Jade P. Wang, Cheryl M. Sorace-Agaskar, Milos A. Popovic, Jie Sun, Gui-Rong Zhou, Hyunil Byun, Jian Chen, Judy L. Hoyt, Henry I. Smith, Rajeev J. Ram, Michael Perrott, Theodore M. Lyszczarz, Erich P. Ippen, and Franz X. Kärtner. Photonic ADC: overcoming the bottleneck of electronic jitter. *Optics Express*, 20(4):4454–4469, 2012.

[74] A. Delwar Hossain, Aurangozeb, Maruf Mohammad, and Masum Hossain. A 35 mW 10 Gb/s ADC-DSP less direct digital sequence detector and equalizer in 65nm CMOS. In *2016 IEEE Symposium on VLSI Circuits*, pages 1–2. IEEE, 2016.

[75] Akihide Sai, Hidenori Okuni, Tuan T. Ta, Satoshi Kondo, Takashi Tokairin, Masanori Furuta, and Tetsuro Itakura. A 5.5 mW ADPLL-based receiver with a hybrid loop interference rejection for BLE application in 65 nm CMOS. *IEEE Journal of Solid-State Circuits*, 51(12):3125–3136, 2016.

[76] Oscar Almer, Salvatore Gnecchi, and Robert Henderson. From linear to geiger mode avalanche detectors for ADC-less VLC receiver architectures. In *2017 IEEE Photonics Conference (IPC)*, pages 31–32, 2017.

[77] Hossein Mohammadnezhad, Huan Wang, Andreia Cathelin, and Payam Heydari. A 115-135-GHz 8PSK receiver using multi-phase RF-correlation-based direct-demodulation method. *IEEE Journal of Solid-State Circuits*, pages 1–14, 2019.

[78] G. F. Earl and M. J. Whitington. Hf radar adc dynamic range requirements. 1999.

[79] L. Pierno, M. Dispenza, G. Tonelli, A. Bogoni, P. Ghelfi, and L. Poti. A photonic adc for radar and ew applications based on modelocked laser. In *2008 International Topical Meeting on Microwave Photonics jointly held with the 2008 Asia-Pacific Microwave Photonics Conference*, pages 236–239. IEEE, 2008.

[80] Yirong Xu, Shangyuan Li, Xiaoxiao Xue, Xuedi Xiao, Xiaoping Zheng, and Bingkun Zhou. An interleaved broadband photonic adc immune to channel mismatches capable for high-speed radar imaging. *IEEE Photonics Journal*, 11(4):1–9, 2019.

[81] Optipedia. LPG and CFBG, 2014. [Online; accessed 1-Aug-2019].

[82] Edmund Optics. Introduction to optical prisms. [Online; accessed 1-Aug-2019].

[83] Edward I. Ackerman. Broad-band linearization of a mach-zehnder electrooptic modulator. *IEEE Transactions on Microwave Theory and Techniques*, 47(12):2271–2279, 1999.

[84] ThorLabs. Automated bias controller for lithium niobate (LiNbO3) modulators. [Online; accessed 10-Aug-2019].

[85] Michael Y. Peng. System demonstration of an optically-sampled, wavelength-demultiplexed photonic analog-to-digital converter. Master's thesis, Massachusetts Institute of Technology, 2011.

[86] Gregor J. McDonald and A. J. Seeds. A novel pulse source for low-jitter optical sampling: a rugged alternative to mode-locked lasers. In *Advanced Free-Space Optical Communication Techniques/Applications II and Photonic Components/Architectures for Microwave Systems and Displays*, volume 6399, page 63990J. International Society for Optics and Photonics, 2006.

[87] Gregor J. McDonald. *Optical sampling and metrology using a soliton-effect compression pulse source*. PhD thesis, UCL (University College London), 2010.

[88] Walt Kester. Understand SINAD, ENOB, SNR, THD, THD + N, and SFDR so you don't get lost in the noise floor. *Analog Devices*, 2008. [Online; accessed 1-Aug-2016].

[89] Analog Devices. HMCAD1511: High Speed Multi-Mode 8-Bit 30 MSPS to 1 GSPS A/D Converter. [Online; accessed 1-Aug-2019].

[90] Amir H. Nejadmalayeri, Matthew Grein, Anatol Khilo, Jade P. Wang, Michelle Y. Sander, Michael Peng, Cheryl M. Sorace, Erich P. Ippen, and Franz X. Kärtner. A 16-fs aperture-jitter photonic adc: 7.0 enob at 40 ghz. In *CLEO: Science and Innovations*, page CThI6. Optical Society of America, 2011.

[91] J. C. Twichell and R. Helkey. Phase-encoded optical sampling for analog-to-digital converters. *IEEE Photonics Technology Letters*, 12(9):1237–1239, 2000.

[92] ThorLabs. DET01CFC:Fiber Input InGaAs Biased Detector User Guide, 2017. [Online; accessed 1-Aug-2019].

[93] Franklyn Quinlan, Tara M. Fortier, Haifeng Jiang, and Scott A. Diddams. Analysis of shot noise in the detection of ultrashort optical pulse trains. *JOSA B*, 30(6):1775–1785, 2013.

[94] Franklyn Quinlan, Tara M. Fortier, H. Jiang, A. Hati, C. Nelson, Y. Fu, J. C. Campbell, and S. A. Diddams. Exploiting shot noise correlations in the photodetection of ultrashort optical pulse trains. *Nature Photonics*, 7(4):290, 2013.

[95] Walt Kester. Aperture time, aperture jitter, aperture delay time removing the confusion. *Analog Devices*, 2008. [Online; accessed 1-Aug-2016].

[96] Rudiger Paschotta. Noise of mode-locked lasers (part I): numerical model. *Applied Physics B*, 79(2):153–162, 2004.

[97] Rudiger Paschotta. Noise of mode-locked lasers (part II): timing jitter and other fluctuations. *Applied Physics B*, 79(2):163–173, 2004.